Spring 2022

Exploring the kinetics and thermodynamics of O–H bond activation by tripodal tris(nitroxide) aluminum and gallium complexes

Joseph S. Scott , '22

Recommended Citation

Scott, Joseph S. , '22, "Exploring the kinetics and thermodynamics of O–H bond activation by tripodal tris(nitroxide) aluminum and gallium complexes" (2022). *Senior Theses, Projects, and Awards*. 260.
https://works.swarthmore.edu/theses/260

Exploring the kinetics and thermodynamics of O–H bond activation by tripodal tris(nitroxide) aluminum and gallium complexes

Joseph S. Scott

Senior Course Thesis

Advisors: Christopher R. Graves & Paul R. Rablen

Department of Chemistry & Biochemistry

Submitted: 5/13/2022

Acknowledgments

In the past year, I have learned a vast amount of chemistry — organic, inorganic, and synthetic, just to name my favorites. However, I have learned an even greater amount about being a chemist in the laboratory, and being a scientist in general. Of course, I owe this my advisor, Dr. Chris Graves, for catalyzing this intellectual and personal development of mine. I am extremely grateful for the ideal balance of his hands-on mentorship and his hands-off philosophy that he implemented, all in the name of my development as a synthetic chemist. I am also very thankful for him making me not only be prepared, but *feel* prepared to pursue a Ph.D. in chemistry.

I want to thank Dr. Paul R. Rablen for his patience and generosity in working with me to perform electronic structure calculations to explore the wet chemistry I was doing computationally. His knowledge and support are key in the making of this thesis, as well in much of the work that goes on in the Graves Group. I also appreciate his willingness to talk about any sort of chemistry that I happen to be thinking about as we occasionally cross paths on campus.

I would like to thank the undergraduate members of the Graves Group with which I have worked: Omar Saleh, Richard Cardrino, and Julia LeBlanc. Not only do I greatly appreciate their eagerness to talk about chemistry and lend a hand in the lab, but the fun of working in the lab with these friends is something I will dearly miss. I would also like to thank past member of the Graves Group Mika Maenaga for her early mentorship in the lab before the start of the COVID-19 pandemic, her assistance in applying to graduate schools, and her friendship.

I want to thank Patrick Carrol and Michael Gau at the University of Pennsylvania for solving my crystal structure.

I am grateful for the Department of Chemistry and Biochemistry at Swarthmore College. They are responsible for my growth as a student, chemist, and teacher; I will always love to learn and do chemistry, and help others understand it. I can already tell they have prepared me extraordinarily well for my future endeavors.

Lastly, I owe an endless amount of gratitude to my family for their support throughout my undergraduate experience, and my life thus far. Without them, I would not have achieved as much as I have, nor would I be the person I am today. Thank you.

Abstract

Aluminum is one of earth's most abundant and cheapest metals, and it is also non-toxic and environmentally friendly. This makes it an ideal candidate to be implemented in organometallic chemistry as a greener alternative to metal-based systems based on heavy and/or precious metals. One of the realms in which aluminum and other group 13 elements show promise is metal-ligand cooperative chemistry, which can afford transition metal-reminiscent small molecule activation chemistry. Our studies of organic ligands with nitroxide-functionalities within Al and Ga coordinative systems has led us to the discovery of tripodal tris(nitroxide) Al and Ga complexes with abilities to engage in metal-ligand cooperativity, including in their reaction with small molecule alcohol substrates. In an effort to better understand the mechanism of the O-H bond activation mechanism exhibited by these complexes, we report the results of various kinetics experiments that explore how alcohol O-H acidity (pK_a) and metal center (Al, Ga) affect reaction rate, as well as an observable kinetic isotope effect. We also report the results of the screening of various alcohol substrates with these complexes, and find a strong correlation between general reactivity and alcohol acidity.

List of common abbreviations

dipp = 2,6,-Diisopropylphenyl

dpp-bian = 1,2-Bis[(2,6-diisopropylphenyl)imino]acenaphthene)

$(^{R}\text{pyNO}^{-})$ = *N*-*tert*-butyl-*N*-(2-(5-R-pyridyl))nitroxyl, R = H, CH_3, CF_3)

MLC = metal-ligand cooperativity

ELC = element-ligand cooperativity

(TriNOx) = $[\{(2\text{-}^{t}\text{BuNO})C_6H_4CH_2\}_3N]^{3-}$

THF = tetrahydrofuran

G4 = a hybrid method

Table of Contents

1. Introduction

1.1 Catalysis and sustainable alternatives to the late transition metals

Throughout the history of modern chemistry, catalysis has been a major field of study, and is frequently found at the heart of many applications within the chemical sciences. In 1836, the Swedish chemist Jöns Jacob Berzelius defined a catalyst as a substance that increases the rate of a chemical reaction without being consumed in the process.[1] Not only is catalysis occurring inside our bodies in the form of enzymatic reactions that are necessary to sustain our lives, but many people may recognize non-biological catalysis in two aspects of everyday life: the catalytic converters that clean up motor vehicle emissions, and the Haber-Bosch process, which produces the fertilizers necessary for the production of the food we eat every day. Catalytic converters commonly employ the precious transition metals Pt and Rh, which react with NO_X, CO, and hydrocarbons and convert them to reduced N-containing species, and to CO_2 and other oxidized, less toxic C-containing species, respectively.[1] With the help of transition metal catalysts, the Haber-Bosch process converts H_2 and atmospheric N_2 into "fixed" nitrogen (NH_3 and NH_4^+) that goes on to be used for fertilizer in agriculture. These two forms of everyday catalysis can be characterized as small-molecule activation reactions, which make up a field that has many industrial implications for chemical feedstocks, climate change and energy sustainability,[2] and for potential uses in chemical synthesis. Of course, catalysis can applied in the synthetic realm on not-so-small molecules, and can afford impressive chemical transformations, such as stereospecific C–C bond formation,[3] olefin metathesis,[4] and cross-coupling reactions,[5] that would simply not proceed in the absence of these catalysts.[6]

Since Berzelius' time, many industrial and synthetic catalysts feature the precious, late transition metals at the heart of their reactivity. This is because these metals, such as Rh, Pd, Pt, Ru, Ir, and Os, are stable, are resistant to unintended oxidation, demonstrate pi-bond acidity, and display useful reaction selectivities. Sadly, there is a downside to using these precious elements — they are expensive, toxic, and limited in abundance,[6] all factors that potentially encourage unethical mining practices and environmental policies. In recent decades, there has been a large movement to try and achieve rare transition metal-like reactivity in catalysts that contain non-precious elements, namely with the cheaper, less toxic first-row transition metals and the even less expensive main group elements[7]. However, although the prices of these elements are lower[8], the catalytic abilities of the main group elements are not as immediately accessible as those of the transition metals. This is due to the strong "preference" of these elements to be in their usual stable, unreactive oxidation states; attempting to perform redox catalysis with them can prove to be challenging. Therefore, research chemists have been seeking ways to get around the unreactivity and redox inactivity of the main group elements.

The Graves Lab at Swarthmore College contributes to the effort of improving the reactivity of main group elements and combines it with the environmentally benevolent prospects of implementing the Group 13 metals aluminum and gallium as sources of catalysis. Aluminum is the most abundant metal in the earth's crust (~8% by weight); with the benefit of being non-toxic,[9] it is one of the cheapest elements on earth, being priced at ~$2/kg as of 2019.[8] Gallium (~$213/kg, 2019), while not as cheap as aluminum but still much more affordable than a number of the transition metals,[8] has moderate abundance in earth's crust. These two main group metals are prime candidates for catalytic development with non-innocent ligand reactivity; while they are very redox stable at their +3 oxidation state, compounds of Al(III) and Ga(III) have been used as homogenous catalysts for more than a century. Simple Lewis acidic salts like aluminum trichloride are used for Friedel-Crafts alkylations and acylations,[10] and for oxidation/reduction of alcohols/ketones, alkene epoxidation, and C–H bond activation.[11] Aluminum tris(*tert*-butoxide) is used in the Oppenhauer oxidation of alcohols,[12] and in the opposite reaction direction, the reduction of ketones in the Meerwein-Ponndorf-Verley reduction.[13] Additionally, Al(III) and Ga(III) have engaged in catalysis when coordinated to both redox-inactive and redox-active ligands.[11]

1.2 Non-innocent ligands improve the reactivity of transition metals and main group elements via metal/element ligand cooperativity

Much work is being done to overcome the unreactivity of non-precious transition metals and main group elements. A promising route around the obstacle is the complexation of non-innocent ligands to these redox-stable elements in order to enhance the reactivity of the chemical system. Non-innocent ligands refer to a broad class of ligands that are either redox-active, or are actively involved in bond-making or bond-breaking processes; the latter phenomenon can also be described as chemically "non-innocent", or "cooperative".[14] Put another way, redox-active non-innocence describes a ligand's participation in electron acceptance or donation with the metal to which it is bonded, while chemical non-innocence (further referred to as metal/element-ligand cooperativity) refers to a ligand's direct participation in formal two-electron processes with a substrate.

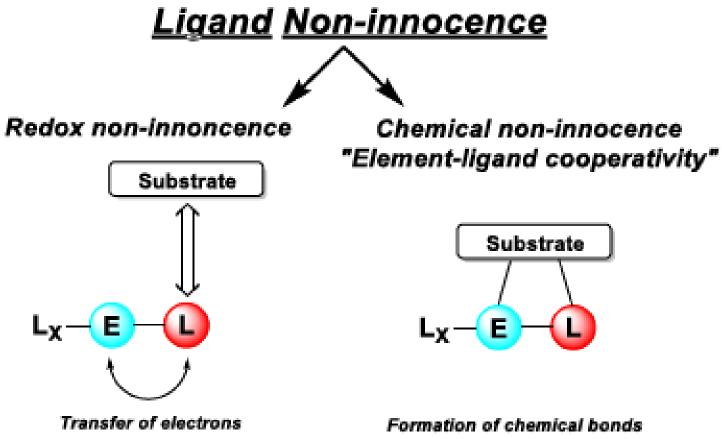

Figure 1. The difference in reactivity between redox and cooperative non-innocence. Adapted from Greb et al. 2020.[15]

Metal-ligand cooperativity (MLC) has been well-documented among the transition metals, both precious and non-precious, for a few decades now, particularly within pincer-type ligand systems. Some notable examples of transition MLC, with both precious and base metals, feature metals such as Ru,[16,17] Ir,[18] Ni,[19] Fe,[20] Sc,[21] and Mn.[22] Fortunately, there is also a sizeable presence in the literature of greener main group elements engaging in element-ligand cooperativity (ELC); elements such as B,[23] Si,[24] and Ge[25] are forefront in this realm. Main group MLC or ELC can be succinctly stated as a main group metal or element and its ligand's ability to perform synergistic substrate activation by formally two-electron processes, and is a field of chemistry that is only just beginning to grow.[15]

MLC and ELC reactivities displayed by main group complexes are unified by a key similarity: the metal/element and its corresponding ligand(s) both play a key mechanistic role in their reactivity with a small molecule substrate. In many cases, this reactivity can generally be described as the splitting of a substrate's X–H bond across the metal/element–ligand complex, wherein the Lewis acidic metal/element accepts the (X^-)-containing substrate fragment, and a Lewis basic atom on the ligand accepts the proton (H^+). The dual presence of sites of Lewis acidity and basicity within the metal-ligand framework seems to unite all cases of MLC/ELC. This is certainly not absent from the literature discussing group 13 MLC catalysis, which is what the next section will primarily be focused on, along with how it serves as the context of the research project I conducted in the laboratory under the supervision of Dr. Christopher Graves.

1.3 Aluminum and gallium can engage in metal-ligand cooperativity to activate X–H bonds

Aluminum-ligand cooperativity was first reported by the Jordan group in 1998; they reported the impressive 1,4 cycloaddition of ethylene to a cationic aluminum β-diketiminato complex, the product of which could lose ethylene via cycloreversion when exposed to nucleophiles (**Scheme 1**).[26]

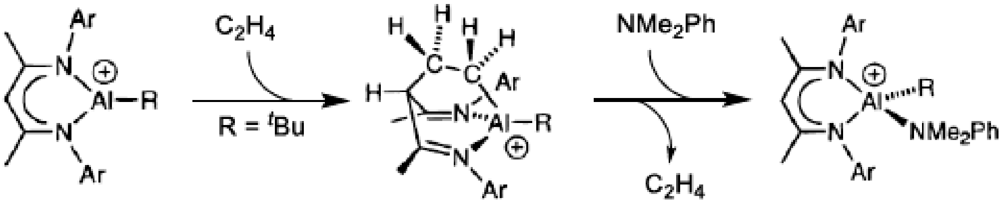

Scheme 1. The cycloaddition of ethylene to a cationic aluminum β-diketiminato *tert*-butyl complex, and subsequent cycloreversion upon addition of a nucleophile (dimethylphenylamine). Adapted from Jordan et al. 1998.[26]

MLC performed by β-diketiminato aluminum and gallium complexes has been reported many times over the past two decades. With this type of complex, Abdalla et al. achieved the activation of a range H–X bonds of different polarities; furthermore, H_2 bond activation by these complexes gives way to gallium-hydrides that enable the selective catalytic reduction of CO_2 to a methanol derivative (**Scheme 2**).[27] This metal-ligand framework is very similar to the work of Yao et al. 2008, in which the main group elements at play were the Group 14 elements Si and Ge.[25]

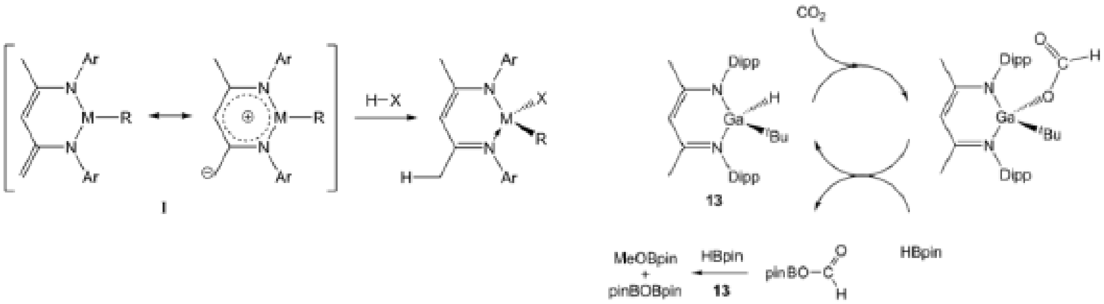

Scheme 2. H–X bond activation by a β-diketiminato gallium complex, followed by selective reduction of CO_2 by a β-diketiminato gallium hydride complex to form a methanol derivative. Reproduced from Abdalla et al. 2015.[27]

Hitzfeld and Kretschmer 2020 used the same metal-ligand system to achieve the activation of the X–H bonds of dihydrogen, ammonia, hydrogen sulfide, and silane (**Scheme 3A**).[28] Additionally, Feld et al. 2021 reported the X–H bond activation of water, amines, phenylacetylene, and phenylphosphine by a modified β-diketiminato phosphanyl-phosphagallene complex.[29] As can be seen in **Scheme 3B**, the Lewis pair on the phosphanyl ligand is working cooperatively with the Lewis acidic Ga metal center to activate a X–H bond — a mechanism similar to that of frustrated Lewis pair systems.[15]

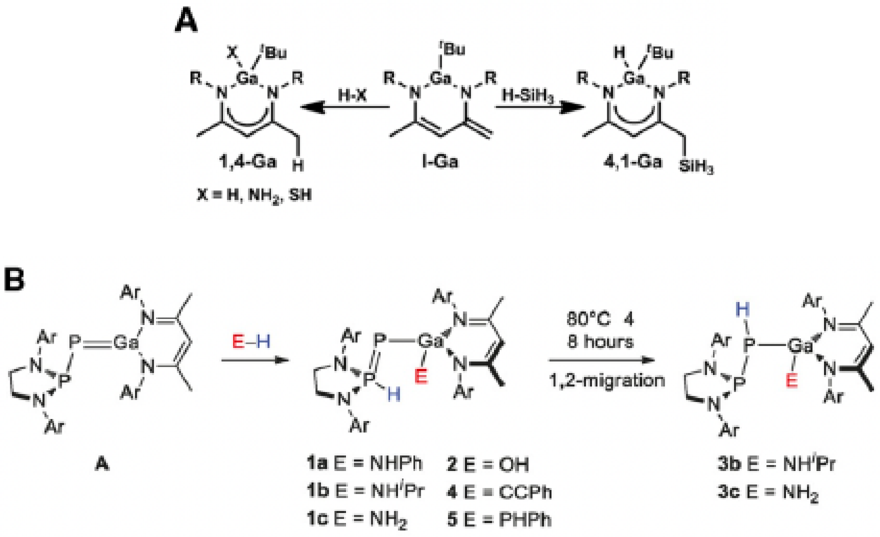

Scheme 3. **A**. A β-diketiminato gallium complex activating various X–H bonds via MLC. Reproduced from Hitzfeld and Kretchmer 2020.[28] **B**. The scope of X–H (E–H in the reference) bond activation performed by a phosphanyl-phosphagallane complex. Reproduced from Feld et al. 2021.[29]

Besides β-diketiminato metal complexes, Fedushkin reported the reversible addition of simple alkynes to diamide aluminum and gallium complexes[30], shown in **Scheme 4A**. This chemistry has the potential to form new C–C bonds, which is an essential practice in chemical synthesis. In 2013, Piskunov et al. reported the addition of allyl halides across the metal-ligand framework of a bis-*o*-amidophenolate Ga (III) complex; this reactivity is seen in **Scheme 4B**.[31] More recently, reversible O–H bond activation was facilitated by a calix[4]pyrrolato aluminate complex by Sigmund and Greb (**Scheme 4C**).[32]

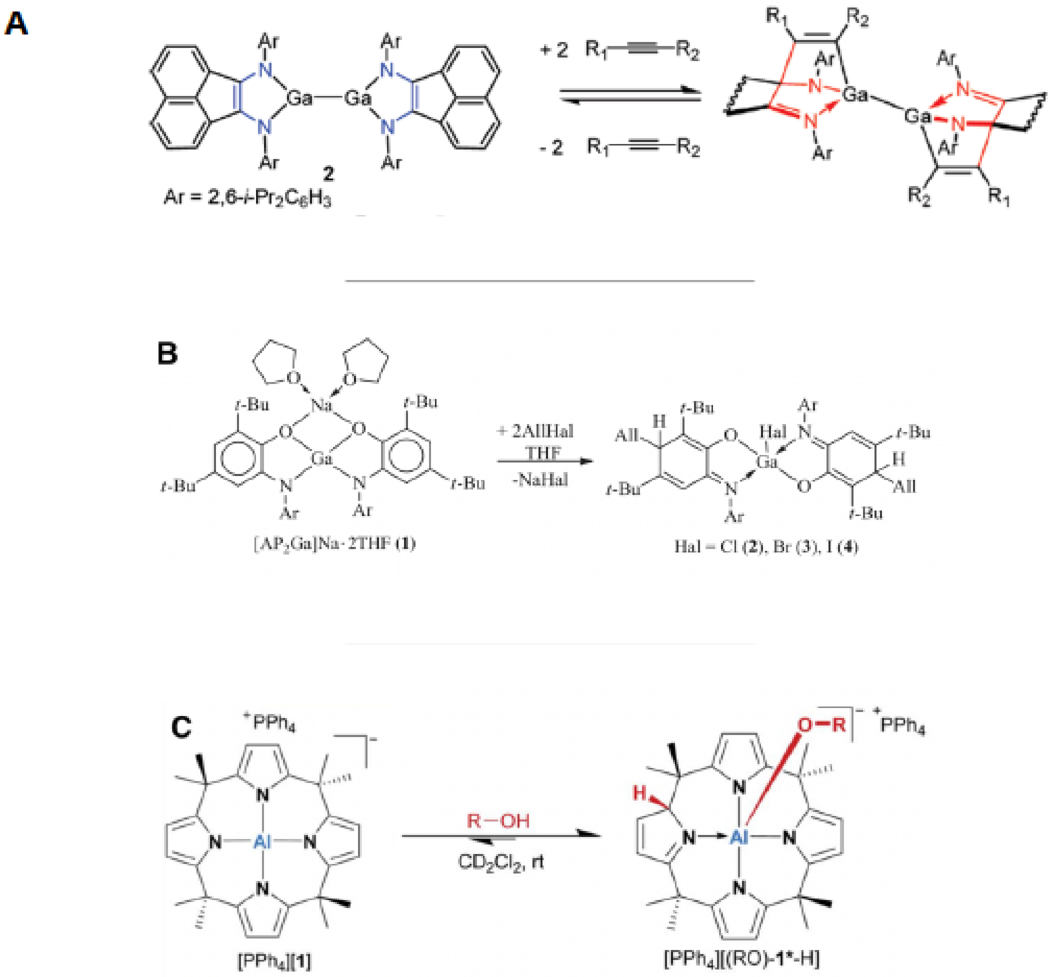

Scheme 4. **A**. Reversible addition of alkynes to diamide aluminum and gallium complexes. Reproduced from Fedushkin et al. 2010.[30] **B**. Activation of allyl halides across a bis-*o*-amidophenolate Ga (III) complex. Reproduced from Piskunov et al. 2013.[31] **C**. Activation of simple alcohol O–H bonds facilitated by an aluminate complex. Adapted from Sigmund and Greb 2020.[32]

However, when it comes to small molecule bond activation with aluminum-ligand cooperativity, the Berben group at U.C. Davis has made significant contributions to the literature, both in proof of concept and mechanistic investigation. Their aluminum bis(imino)pyridine pincer-type complexes have demonstrated impressive small molecule substrate scope, and present lots of promise for sustainable catalysis, carbon remediation, and dinitrogen fixation. Taking inspiration from Milstein's 2007 work with Ru pincer complexes[16], her group installed an Al(III) center to a tridentate bis(imino)pyridine ligand to form an aluminum hydride complex. This system was first reported to engage in MLC to activate N–H bonds of anilines, and subsequently release dihydrogen upon dehydrogenation.[33] Soon after, the complex was shown to have the ability to activate a wide range of X–H bonds, including sulfonamide N–H bonds, aromatic and benzylic alcohol O–H bonds, and the formic acid O–H bond. The products afforded from O–H activation can undergo dehydrogenation upon heating or addition of a second alcohol or formic acid.[34,35] The reaction schemes that generalize this impressive reactivity can be seen in **Scheme 5A**, while Berben's proposed catalytic cycles for dehydrogenation of small molecules (formic acid and benzylamine specifically) are shown in **Scheme 5B**.

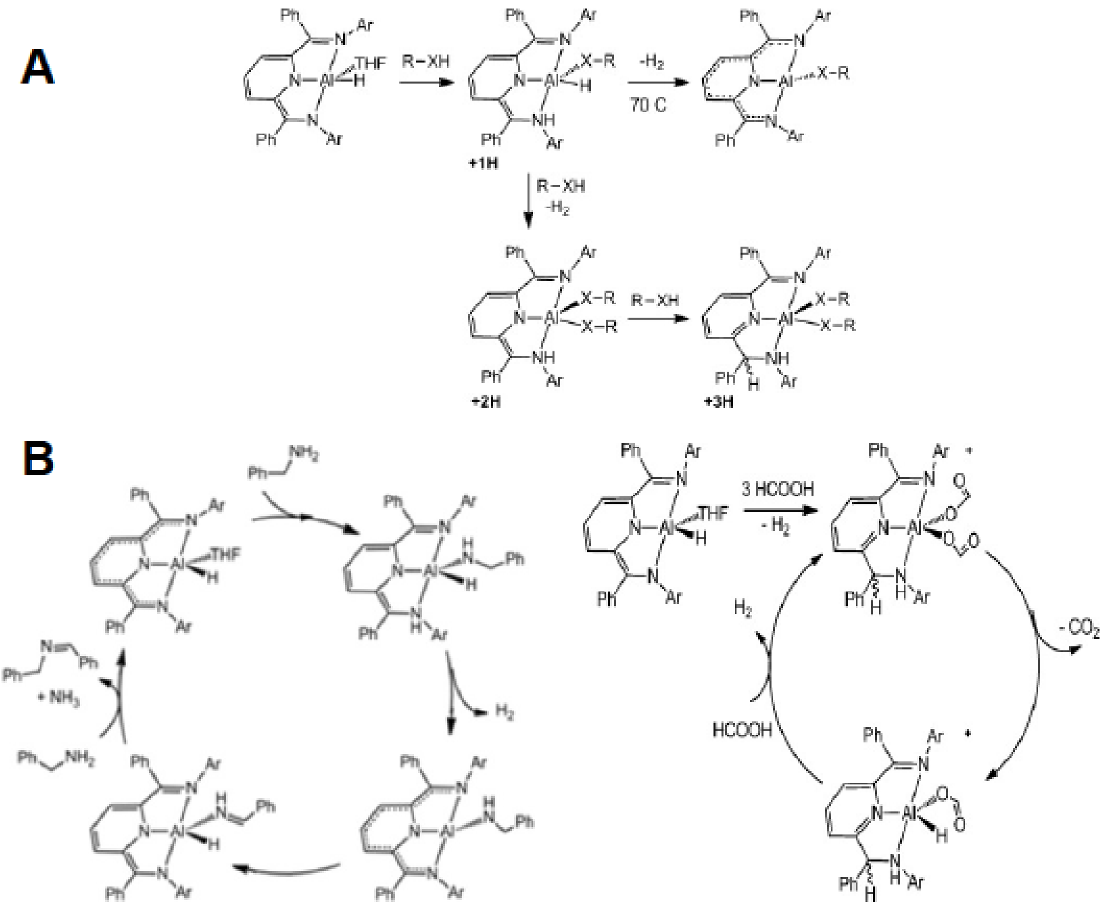

Scheme 5. **A**. N–H and O–H (X = N, O) bond activation of amines, alcohols, and formic acid upon reaction with the aluminum bis(imino)pyridine pincer complex. Reproduced from Berben 2015.[36] **B**. Catalytic cycles for the dehydrogenation of benzylamine (left) and formic acid (right). Reproduced from Berben 2015.[36]

1.4 The Graves Lab studies Group 13 MLC with (TriNOx)Al and (TriNOx)Ga

As mentioned above, The Graves Lab is interested in sustainable catalysis design by attempting to improve the reactivity of the Group 13 metals in catalytic and redox systems. The lab mainly synthesizes redox-active ligands that permit the Group 13 metals to achieve oxidation states other than its highly stable +3 one; characterization and various methods of analysis to assess redox and catalytic abilities follow synthesis. As a result of the lab's work in investigating nitroxide ligands, the group reported a redox-active pyridyl nitroxide ligand that doubly binds to aluminum and gallium; the resulting complexes exhibit electrochemical reversibility, demonstrated by cyclic voltammetry (**Figure 2**).[37,38] Therefore, this (^{R}pyNO^{-}) ligand can be considered a redox non-innocent ligand.[15]

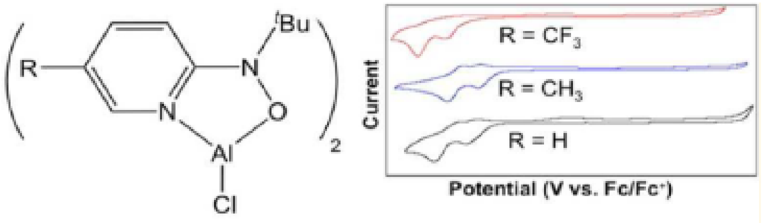

Figure 2. The (^{R}pyNO^{-})$_2$AlCl complexes, and their electrochemical reversibility, from the Graves lab in 2015. Reproduced from Poitras et al.[37]

The Graves lab also synthesizes a cooperative ligand, referred to as (TriNOx)H_3 [or (TriNOx)$^{3-}$ in its deprotonated/chelated form]. Initially, the (TriNOx)H_3 ligand was synthesized in 2015 to optimize the separation of the rare earth metals neodymium and dysprosium by the Schelter group[39]; its synthesis was based off of the Chen et al. protocol to synthesize *tris*-2-bromobenzylamine.[40] The Graves group took synthetic inspiration from this work, and chose to explore the potential redox capabilities of the ligand when bound to Group 13 metals. With the ligand in hand, the series (TriNOx)M (M = Al, Ga) was synthesized; the current, optimized synthesis route is diagramed in **Scheme 6**.

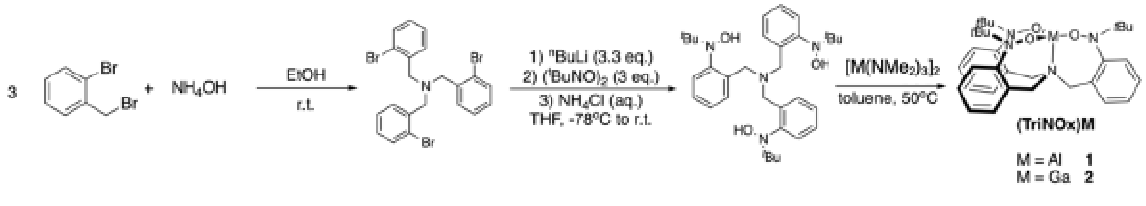

Scheme 6. Current synthetic route to (TriNOx)M.

2-bromo-benzylbromide undergoes triplicate substitution in ammoniacal ethanol solution. The resulting tris-2-bromobenzylamine is then treated with stoichiometric *n*-butyllithium, and then applied with stoichiometric nitroso-tert-butane dimer, and finally protonated with aqueous ammonium chloride, giving us the (TriNOx)H_3 ligand. Then, the ligand undergoes reaction with $M(NMe_2)_3$ dimer (M = Al, Ga) to give the solid (TriNOx)M product.

In 2019, Woodside and Smith of the Graves group published the synthesis and characterization of the (TriNOx)Al complex[41]; in this investigation it was found that the complex did not display redox-activity, but rather likely participated in aluminum-ligand cooperative chemistry when it was observed to catalyze the hydroboration of carbonyls. The proposed catalytic mechanism is shown in **Scheme 7**.

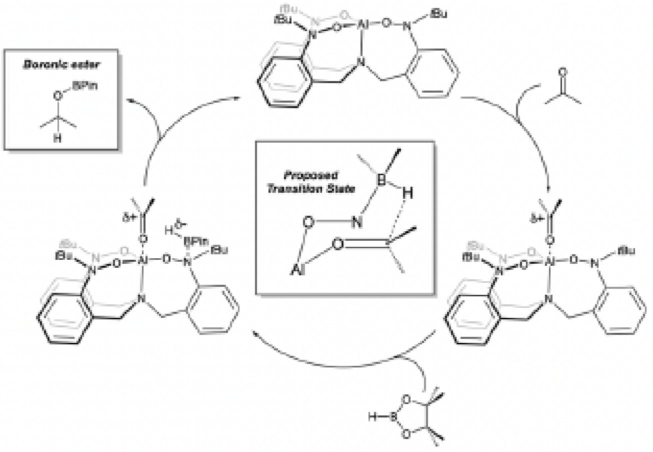

Scheme 7. The proposed catalytic cycle for the hydroboration of carbonyls via element-ligand cooperativity by (TriNOx)Al. Reproduced from Woodside et al. 2019.[42]

The first step of the catalytic cycle involves the coordination of the ketone to the Lewis acidic metal center. Then, the TriNOx ligand N lone pair coordinates to the boron in pinacolborane. This is the step in which (TriNOx)Al engages in MLC; the Al center and Lewis basic ligand cooperate to coordinate the ketone and borane reactants in a geometry that makes their interactions ideal for the proceeding transformation to take place.

Finally, the ketone undergoes hydroboration by the pinacolborane, forming a boronic ester. The cycle then restarts.

Hydroboration reactions with loaded with (TriNOx)Al had higher yields than those loaded with (TriNOx)Al-pyridine adduct; this supported the idea that the Al metal center is involved in competitive coordination with the pyridine and the ketone that undergoes reduction. This aligns with the fact that the (TriNOx)Al metal center is Lewis acidic, with an experimentally calculated Gutmann-Beckett acceptor number of 75.[43,44] Considering this with the fact that the neighboring N atoms of the nitroxide groups are Lewis basic (as evidenced by their ability to be methylated by excess methyl triflate[42]), Woodside et al. concluded that MLC was likely at play in the reactivity of the hydroboration catalyzed by (TriNOx)Al. This conclusion is evidence-based; we see in the literature that nearby sites of Lewis acidity and basicity within an organometallic complex frequently have the ability to engage in MLC in their catalytic mechanisms.

Since the findings of Woodside et al., the (TriNOx)Ga complex has been synthesized and characterized; this and all work after has yet to be published. Continued investigation into the reactivity of (TriNOx)M conducted by Mika Maenaga ’21 revealed that the complex facilitates the activation of O–H bonds of alcohols. Two structures of (TriNOx)M-alcohol products, namely products **3** and **6**, formed from the reaction of **1** with *tert*-butanol and **2** with phenol respectively (see **Scheme 8**), were verified via single-crystal X-ray crystallography (XRCD) (**Figure S1, S3**).

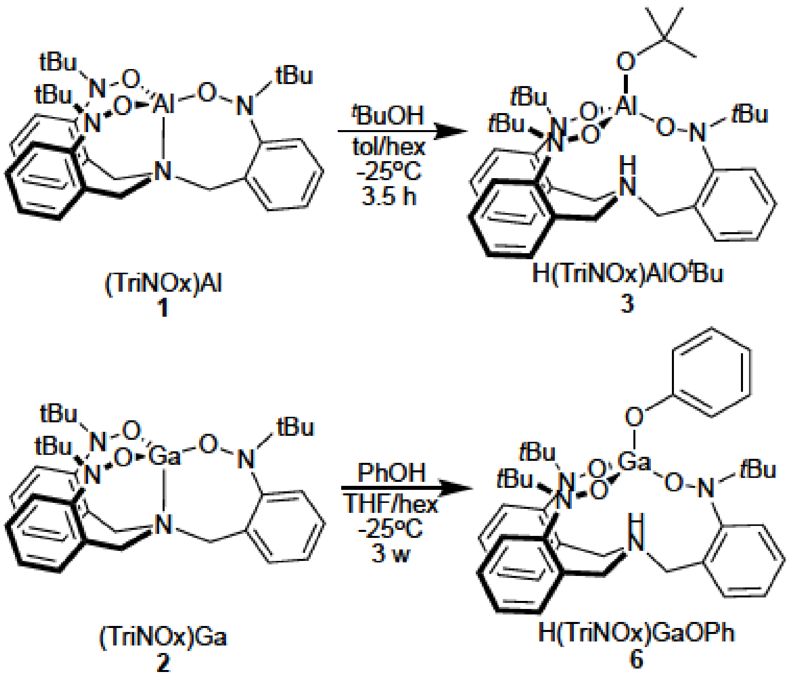

Scheme 8. The early syntheses of H(TriNOx)AlO^{t}Bu (**3**) and H(TriNOx)GaOPh (**6**).

Maenaga then continued research into the element-ligand cooperativity displayed by (TriNOx)M via a computational mechanistic analysis. Her findings show that the product formation mechanism proceeds through neutral compounds; this supports an MLC-type mechanism, which as we have mentioned, involves concerted substrate bond-breaking and bond-formation events across the metal-ligand framework. Furthermore, Maenaga found that the acidity of the substrate O–H bond has an effect on reaction pathway, including activation barrier height, and overall reaction exergonicity.[45]

Based on Maenaga's observations and theoretical conclusions about the MLC reactivity demonstrated by (TriNOx)M, we decided to follow up on her findings by further exploring the O–H bond activation demonstrated by (TriNOx)M in the laboratory, with a focus on how O–H bond acidity and metal center Lewis acidity affects reaction kinetics and thermodynamics. To better understand these aspects of the chemical system, kinetic studies were conducted on reactions of **1** and **2** with *tert*-butanol, isopropanol, and methanol. We performed a kinetic isotope experiment with complex **1** and *tert*-butanol/*tert*-butanol-OD to gain mechanistic insight to the bond activation event, and performed further kinetics experiments with the other two alcohols to demonstrate the effect of (TriNOx)M metal center and alcohol acidity (measured by pK_a) on reaction rate. Then, we ran a screening experiment with a range of alcohols of different acidities to demonstrate dependence relationships between both (TriNOx)M metal center and alcohol pK_a with the % conversion and equilibrium constant of a given alcohol addition reaction. Not only will this work clarify the (TriNOx)M chemical system and potentially open it up to new modes of catalysis, but it will ideally contribute to the growing field of sustainable MLC catalysis.

2. Results & Discussion

2.1 Synthesis and characterization of (TriNOx)M alcohol addition products

Syntheses of the following compounds were achieved: H(TriNOx)AlO^{t}Bu (**3**), H(TriNOx)AlOPh (**5**), H(TriNOx)GaOPh (**6**), H(TriNOx)AlOBn (**7**), and H(TriNOx)GaOBn (**8**). Partial syntheses H(TriNOx)GaO^{t}Bu (**4**) and H(TriNOx)GaOBn (**8**) are also reported here; these reports and the observations that come with them are the launch pad for the exploration that we describe in this thesis. **Scheme 9** illustrates these syntheses.

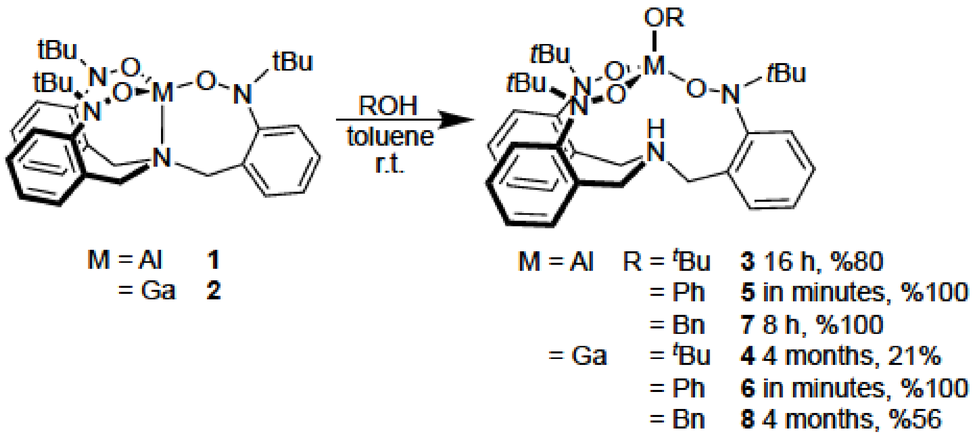

Scheme 9. The syntheses of H(TriNOx)MOR alcohol addition products.

To synthesize **3**, (TriNOx)Al (**1**) was reacted with three molar equivalents of *tert*-butanol via an overnight stir in toluene at room temperature. **1** isn't immediately soluble in toluene, and therefore the reaction is not homogenous to start. However, as the reaction proceeds, the solution becomes more and more translucent as **1** gets "pulled" into solution while it is converted to **3**. After 24 h, the solvent was evaporated via vacuum pump; dried **3** appeared as a light tan solid, with a yield of 81%. **3** is soluble in benzene, toluene, chloroform; it decomposes in pyridine, as evidenced by ^{1}H NMR. When **3** is dissolved in pyridine-d5, a mixture of starting material **1** and product **3** is yielded, indicating that pyridine deprotonates **3** and gives back **1.**

Note that we push the reaction of **1** with *tert*-butanol forward by adding three molar equivalents of the alcohol; adding stoichiometric *tert*-butanol gives a mixture of product **3** and starting complex **1** (see **Table 2** for an exact % conversion to **3**). This is evidence that the system is in a state of equilibrium; however, greater evidence lies in results of the reactions of (TriNOx)Ga (**2**) with *tert*-butanol in the attempts to synthesize **4**. Even with the addition of excess *tert*-butanol to a solution of **2** dissolved in toluene or

THF, the equilibrium of this reaction at room temperature lies significantly to the left; the major species in solution after multiple days of allowed reaction time remains as the starting complex **2**. Additionally, the attempt to crystalize **4** via reaction of excess *tert*-butanol in hexane layered onto **2** dissolved in THF at -25°C is unsuccessful, but gives a reactant-to-product ratio of about 1:4 (determined by ^{1}H NMR spectroscopy of the isolated, non-crystalline solid that crashed out over the course of 4 months). This suggests that the outcome of the reaction has a temperature dependence, which is more evidence for the system being one in a state of equilibrium. Note that we also tried to synthesize **4** via a salt metathesis reaction of stoichiometric potassium *tert*-butoxide added to a solution of H(TriNOx)AlCl dissolved in THF; the product of this reaction is **1**, indicating that HCl is eliminated from H(TriNOx)AlCl via deprotonation by the *tert*-butoxide base.

To synthesize compounds **5** and **6**, the appropriate (TriNOx)M compound (**1** or **2**) was reacted with a stoichiometric amount of phenol for 8 h in toluene at room temperature. These products are insoluble in toluene and benzene, and is evidenced by its crashing out as a white solid as the reaction proceeds to completion, which occurs notably faster than the translucency change that occurs during the synthesis of **3**. These solids, which are soluble in bromobenzene, and slightly soluble in chloroform and THF, are collected via vacuum filtration and washed with cold hexane, and provide yields of 43% for **5** and 67% for **6**. Similarly to **3**, pyridine causes these products to undergo deprotonation and reversion back to **1** and **2**, but not nearly to the same degree as it does for **3**.

The synthesis of **7** is quite similar to that of **5** and **6**; a stoichiometric amount of benzyl alcohol is added to a solution of **1** dissolved in toluene, and is allowed to stir for 12 h at room temperature. This product also crashes out of solution, although not to the same degree as **5** and **6** since it is slightly soluble in toluene. Therefore, the solid collected via vacuum filtration and washed with cold hexane most likely does not provide an optimized yield, which we report as 20%. This solid is soluble in benzene, chloroform, and THF. Reaction with pyridine was not explored. However, synthesis of **8** via the same procedure (performed with **2** instead of **1**) does not go to completion. Instead, we observe only a 56% conversion to **8** — 44% of **2** remains unreacted in solution, according to crude NMR analysis of the solid evaporated of solvent. Layered crystallization attempts of **8** at -25°C failed to give pure solid, but rather a 3:4 reactant-to-product ratio (not much better than the room temperature, stirred reaction), determined by ^{1}H NMR spectroscopy of the isolated, non-crystalline solid. Adding excess benzyl alcohol to the reaction improves the % conversion of **8**, but not to completion.

All of the isolable H(TriNOx)MOR alcohol addition products have been characterized by ^{1}H NMR spectroscopy, and their corresponding spectra can be found in the Supplemental Data section (**Figures S1, S4-6**). In each spectra, the TriNOx ligand *tert*-butyl groups appear as the most upfield signals, integrating consistently to 27H. Additionally, the most downfield signal in all of the spectra of these products is a broad singlet (or a pair of broad singlets) that integrate to 1H, representative of the basal N–H proton — this appears around δ 11 ppm consistently. The most notable uniting feature of these spectra, however, is the consistent, "diagnostic" migration of the more upfield diastereotopic methylene proton signal from δ 2.84 ppm to around δ 2.4 ppm (for spectra taken in C_6D_6), and its transformation from a doublet to a doublet of doublets, that occurs upon product formation. The doublet of doublets arises from its J coupling with the methylene proton with which it shares its diastereotopic relationship ($J_{Hd\text{-}Hdd} \approx 11.2$ Hz) [also present in the ^{1}H NMR spectrum of (TriNOx)M], and the additional J coupling it experiences from the basal N–H proton ($J_{Hd\text{-}NH} \approx 9.6$ Hz). The more downfield diastereotopic methylene proton signal, however, barely migrates upon formation of product, and does not experience an additional observable J coupling with the basal N–H proton. For more discussion on how the upfield diastereotopic methylene proton signal is used in kinetic and thermodynamic analysis, see Section 4.3.1.

Of course, since the apical alkoxylate ligand of products **3**, **5**, **6**, and **7** differ depending on the alcohol with which **1** or **2** underwent reaction, these signals are unique to the ^{1}H NMR spectra. In the spectrum of **3** (**Figure S1**), the *tert*-butoxyl ligand appears as a 9H singlet around δ 1.81 ppm. In the spectra of **5** and **6** (**Figures S5 & S4**), the phenoxy aryl protons appear in the aryl-H region; these signals are not assigned, as the aryl-H region poorly is defined, and adulterated by residual solvent signals from toluene. In the spectrum of **7** (**Figure S6**), the benzyloxy methylene appears as two doublets, which may indicate that these protons are diastereotopic and that this benzyl alkoxylate ligand is not permitted to freely rotate around its Al–O bond (however, performing temperature-dependent NMR studies would confirm this). The doublets are centered around δ 5.59 ppm, each spin-coupled to each other, with $J = 14.4$ Hz.

Figures S2 and **S3** display the ^{1}H NMR spectra of the impure solids of **4**, produced via unsuccessful, 4 month layered crystallization reactions at -25°C and room temperature, respectively. The chilled reaction yielded the best % conversion (80%)

while the room temperature reaction yielded a 30% conversion. These values are derived from the ratio of product signal to reactant signals on their respective NMR spectra, which notably show the signals of both species. In both **Figure S2** and **S3**, the signals of the TriNOx ligand *tert*-butyl groups and diastereotopic methylene protons for both the starting material **2** and product **4** are visible; taking the ratio of these signals allows for the determination of % conversion, and to see how much (TriNOx)Ga went unreacted (see Section 4.3.1 for a more in-depth description of this analysis). However, the product signals on these spectra are identical to those on the ^{1}H NMR spectrum of **3**; see the discussion above. Similarly, in the ^{1}H NMR spectrum of impure **8** (**Figure S7**), the signals from both starting complex **2** and product **8** are present, and their integration can be used to determine % conversion. More specifically, **Figure S7** displays the spectrum of the isolated solid that crashed out the reaction that took place after three equivalents of benzyl alcohols in toluene layered onto complex **8** dissolved in toluene, and then stored at room temperature for 4 months. These reaction conditions gave rise to a 56% conversion, which is determined by taking the ratio of signals of **2** to signals of **8** (see section 4.3.1). The product signals in this spectrum are identical to those found in the ^{1}H NMR spectrum of **7**, which is discussed above.

Proton-decoupled ^{13}C NMR spectra of the isolable products **3**, **5**, **6**, and **7** have also been collected, and are presented in **Figures S17-20**. In each of these spectra, the signals from the nine methyl carbons of the TriNOx ligand *tert*-butyl groups appear as the most upfield signal (a). The three quaternary carbons of the TriNOx ligand *tert*-butyl groups appear as signal (b), are shifted more downfield due to their attachment to the nitroxyl nitrogen atoms. The methylene carbons appear at peak (e), and are similar in chemical shift to (b). Five of the six TriNOx ligand aryl carbons are resolved on these spectra; the sixth is probably obscured by the solvent residual peak. In the spectrum of **3** (**Figure S17**) specifically, the apical *tert*-butoxyl ligand has two types of carbons — the methyls of this ligand (c), which have a similar chemical shift to the methyls of the TriNOx ligand *tert*-butyl groups, and the quaternary carbon (d) attached to the oxygen bound to the Al atom, which is the most downfield singlet that integrates to 1C. The ^{13}C NMR spectra of products **5** and **6** (**Figures S18 & S19**) are nearly identical, as the compounds only differ in composition by metal center. These spectra share the same common signals as those mentioned above for **3**; considering the phenoxy ligand, the aryl carbon attached to the oxygen atom bound to the M atom appears most downfield on these spectra, and the other five aryl carbon signals appear in the Ar-C region. Finally, in the ^{13}C NMR spectrum of product **7** (**Figure S20**), in addition to the shared spectra features mentioned above, the apical benzyl alkoxylate ligand brings four aryl carbon signals and a significantly downfield signal that represents the carbon of the benzyl methylene, which is attached to the oxygen bound to the Al atom.

Crystal structures of products **3**, **5**, and **6** have been obtained by single-crystal X-ray diffraction crystallography (XRCD). The crystal structures of **3** and **6** have been collected as part of previous work, and can be found in the Supplemental Information section in **Figures S21**. Since the elucidation of the crystal structure of **5** is a relatively recent advancement, it is presented here (**Figure 3**); its collection parameters are listed in **Table S1**.

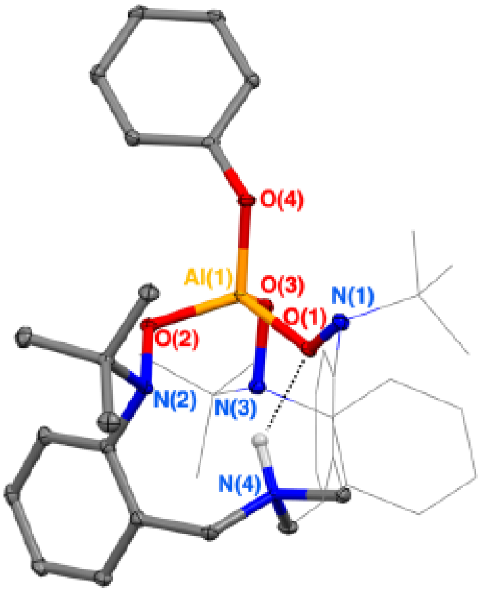

Figure 3. Solid state single crystal structure of H(TriNOx)AlOPh (**5**). Ellipsoids are projected at 30% probability. Non-interacting hydrogen atoms have been omitted for clarity. Two "arms" of the organic ligand are shown in wireframe representation for clarity. R_1=0.0612; τ_4[Al(1)]=0.94. Note the hydrogen bond that exists between one of the ligand oxygens and the basal N–H proton.

These crystal structures provide further evidence that supports the chemical structures we have assigned to not only products **3**, **5**, and **6**, but also the rest of the products; since these structures match what is predicted by ^{1}H and ^{13}C NMR spectroscopies exactly, it is probably a good assumption that the structures we have assigned to products **4**, **7**, and **8** are accurate. Additionally, these crystal structures give us information about the conformational preferences of these products; notably, for all of the crystal structures reported here, we observe a hydrogen bond between the basal N–H proton and one of the nitroxyl oxygen atoms. This causes the ligand "arm" containing this oxygen atom to reach downwards towards the basal N–H.

2.2 Key observations involving the kinetics and equilibria of (TriNOx)M reactivity with alcohols

The syntheses of products **3**, **5**, **6**, and **7**, and the partial syntheses of products **4** and **8**, have led us to make a few key observations, which are as follows:

1) These alcohol addition reactions are dictated by equilibria, as evidenced by the "pushing" of the synthesis of **3** to completion by adding two extra equivalents of *tert*-butanol. This is also supported by the following observation: while the stirred reaction of **2** with *tert*-butanol at room temperature produces minimal **4**, the crystallization attempt of **4** at -25°C results in the crashing out of non-crystalline **4**, which leads to the "pulling" of the reaction forward due to the loss of **4** in solution. This is LeChatelier principle behavior, and supports the idea that these reactions are in equilibrium.
2) These reactions reach equilibrium within 24 h when run at room temperature. This is evidenced by the lack of signal changes in the crude ^{1}H NMR spectra of the alcohol addition product formation reactions after 24 h. This observation simply allows us to operate more soundly under the assumption that these reactions are dictated by equilibria.
3) The reactions of both **1** and **2** with more acidic alcohols, like phenol and benzyl alcohol, have faster rates than those with less acidic alcohols like *tert*-butanol. This is supported by the precipitation of white solid **5**, **6**, and **7** that occurs much faster than the increase in translucency indicative of product **3**

formation. This leads us to theorize that increased alcohol acidity increases alcohol addition reaction rate.

4) Reactions of *tert*-butanol with **1** are faster than with **2**. This is evidenced by the significant yield of **3** we obtain after 24 h of reaction time at room temperature, versus the less impressive yield of **4** we obtain after 4 months of reaction time at -25°C. Based on this, we theorize that the (TriNOx)M metal center has an impact on reaction rate — more specifically, that the higher Lewis acidity of Al compared to Ga increases reaction rate significantly.
5) The % conversion of reactions of both **2** with more acidic alcohols is higher than that with less acidic alcohols. This is evidenced by the completion of the reaction of **2** with phenol, the 56% conversion of **2** to **8** when reacting with benzyl alcohol, and the extremely low conversion to **4** we see when **2** reacts with *tert*-butanol. We theorize that increased alcohol acidity, in addition to increasing reaction rate, also increases reaction yield or % conversion.
6) The % conversion of reactions of alcohols with complex **1** are higher than those with complex **2**. This is evidenced by the comparatively plentiful yields of **3** and **7** we obtain versus the very poor yield of **4** and **8** we obtain when we react one equivalent of *tert*-butanol and benzyl alcohol with both **1** and **2**, respectively. This leads us to theorize that the higher Lewis acidity of the Al atom found in complex **1** compared to the Ga atom found in complex **2** encourages larger % conversion values.

To properly assess the validity of our theories based on the observations above, we decided to explore both the kinetics and thermodynamics of the O–H bond activation reactions of compounds **1** and **2** with alcohols with further experimentation. These experiments include kinetic isotope experiments using *tert*-butanol and *tert*-butanol-OD to demonstrate a kinetic isotope effect (KIE) that should give mechanistic insight into the O–H bond activation of *tert*-butanol by **1**. Additionally, with the alcohols *tert*-butanol, isopropanol, and methanol, we perform experiments to determine the initial rates of these reactions; the results of these experiments can reveal the effects that metal center and alcohol acidity have on reaction rate. Finally, we perform experiments to explore how well the equilibria of the reactions of **1** and **2** with various alcohols are affected by alcohol substrate acidity (pK_a), as well as by metal center.

2.3 Determination of a normal kinetic isotope effect reveals mechanistic insight into the reaction of (TriNOx)Al with tert-*butanol*

Following the procedures described in Section 4.3, kinetic isotope experiments were performed on the reactions of **1** with *tert*-butanol and *tert*-butanol-OD. These reactants were picked due to their easy-to-track reactions and the ready availability of *tert*-butanol-OD in the laboratory. The reaction conditions for each trial were identical: initial equimolar loadings of **1** and appropriate alcohol were introduced to each other in an airfree, septum-sealed NMR tube, after the addition of the internal standard (hexamethylcyclotrisiloxane) at one-sixth the molarity of the reactants. Stock solutions of starting materials were dispensed using gastight syringes to improve accuracy. Reaction progress was tracked using ^{1}H NMR spectra recorded at regular time intervals. Raw data is displayed in **Figure S22**.

Figure 4A shows the reaction profiles of the reaction between **1** and *tert*-butanol and *tert*-butanol-OD for one selected experimental trial; the increase of the concentration of product **3** over time in minutes is observed to be faster than that for **3-D**. **Figure 4B** shows the linear approximations of the initial rates of both reactions in the same trial. Over a total of three trials, the KIE displayed in the conversion of **1** to **3** & **3-D** averages to a value of 1.18. This is a small KIE value, and it suggests the transition state of the alcohol deprotonation step is non-linear.[46]

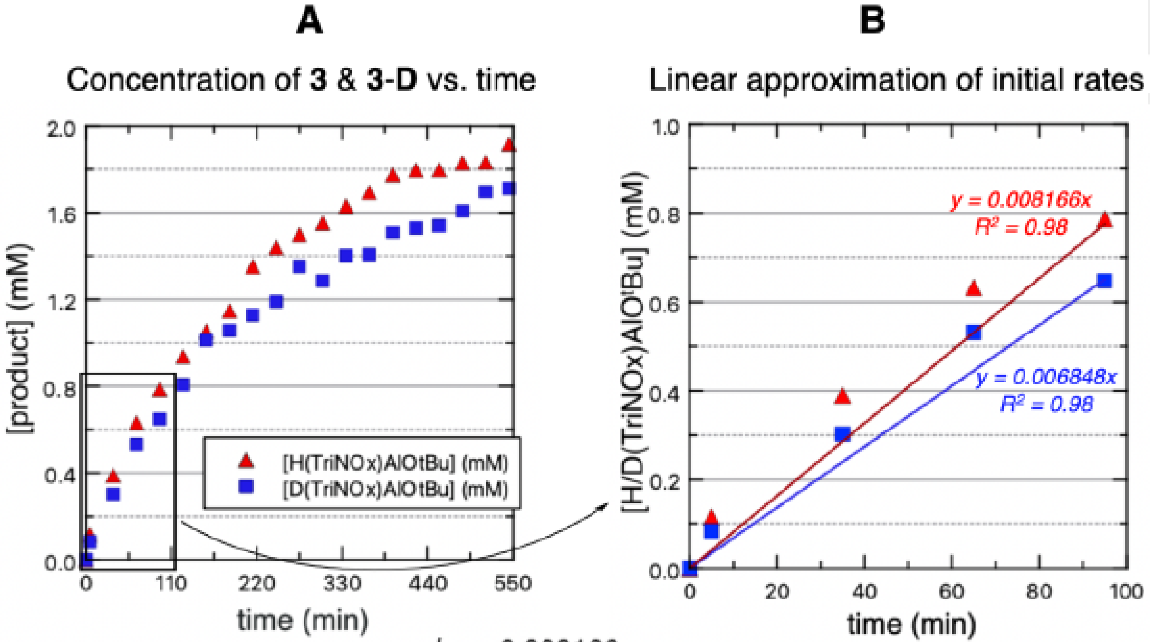

$$\frac{k_h}{k_d} = \frac{0.008166}{0.006848} = 1.19$$

Figure 4. **A**. Kinetics of the formation of product **3** and its isotopologue **3-D** over time of reaction in minutes. Loaded concentrations of (TriNOx)Al and ^{t}BuOH/OD were 6 mM. Trial data representative of *n* = 3 experimental trials. **B**. Linear fits of initial rates of the same reactions over time of reaction.

This result agrees with the findings of Maenaga and Graves, in which they computationally derived a square-like transition state at the point of O–H bond activation.[45] A square-like transition state, such as the one portrayed in **Figure 5**, would consist of predominantly O–H bond bending modes rather than stretching modes, and would therefore be more consistent with the low KIE we determine from this experiment.[46]

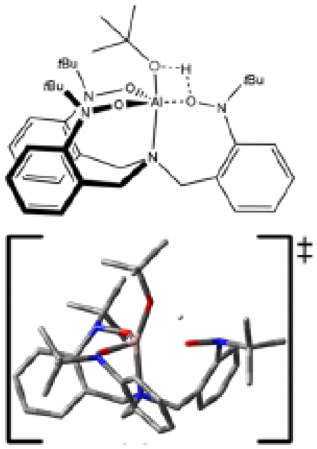

Figure 5. Transition state representing the point of O–H bond activation in the conversion of complex **1** to product **3**. Note the square-like shape of the transition state. Reproduced from Maenaga and Graves.[45]

2.4 Kinetic measurements reveal the effects that Al and Ga Lewis acidity and alcohol pK_a *have on reaction rates*

Initial observations regarding reaction rate, such as witnessing the slow increase in translucence of the reaction of **1** with *tert*-butanol, or the fast precipitation of the white solid **5** upon reaction of **1** with phenol, indicated to us that alcohol acidity may have an impact on rate of reaction. Using the methods described in Section 4.3, ^{1}H NMR spectroscopy was implemented to track the initial rates of the reactions of complexes **1** and **2** with the alcohols *tert*-butanol (pK_a = 32.2), isopropanol (pK_a = 30.25), and methanol (pK_a = 29.0). Equimolar loadings of **1** and the appropriate alcohol were introduced to each other in an airfree, septum-sealed NMR tube, after the addition of the internal standard at one-sixth the molarity of the reactants. Stock solutions of starting materials were dispensed using gastight syringes to improve accuracy — note that these are the same conditions used to perform the kinetic isotope experiments detailed in Section 2.3. NMR spectra were recorded every 2 minutes, with the exception of the reactions between **1** and methanol, which instead had NMR spectra recorded every 1 minute. Alkoxylate ligand (-O^{t}Bu, -O^{i}Pr, and -OMe) signals of the product for each respective reaction were integrated; these values were converted into concentration of product with the implementation of the internal standard of known concentration, and then plotted against the time of reaction. Experiments were performed in triplicate. The observed initial rates of these trials are tabulated in **Table 1** and plotted as a function of alcohol pK_a per complex in **Figure 6**. The raw data plots and initial rates for all of the reactions can be found in **Figure S23-25**.

Table 1. Initial rates of reaction of complexes **1** and **2** with *tert*-butanol, isopropanol, and methanol, at loaded concentrations of 6 mM. Acidities represented by pK_a measured in DMSO.[47]

substrate	pK_a (DMSO)[47]	average initial rate (mM•min^{-1})	
		reaction with **1**	reaction with **2**
^{t}BuOH	32.2	0.0124 ± 0.0006	0.0007 ± 0.0003
^{i}PrOH	30.25	0.4333 ± 0.0410	0.0076 ± 0.0006
MeOH	29.0	0.9320 ± 0.0869	0.1838 ± 0.0124

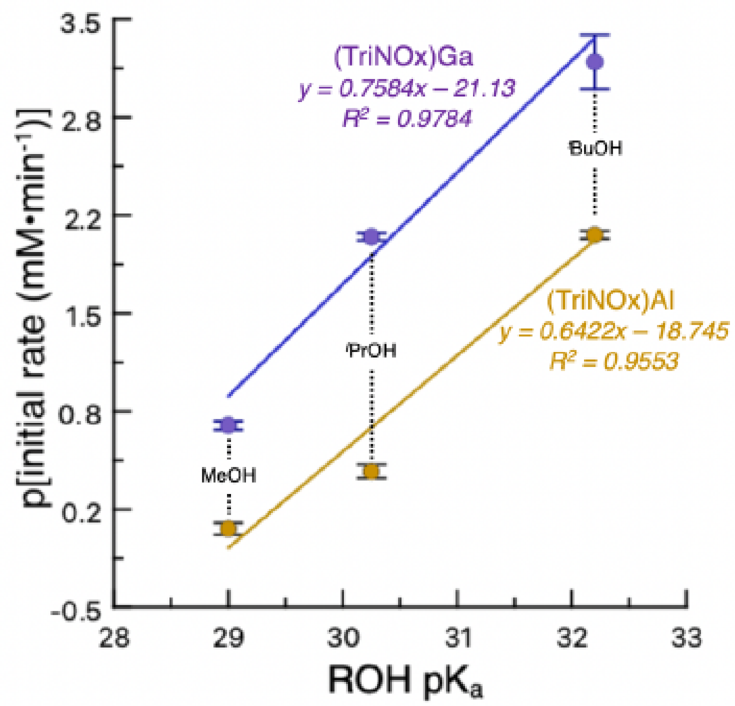

Figure 6. Proposed linear relationships of the negative logarithm of the initial reaction rates of complexes **1** and **2** with selected alcohols vs. the selected alcohol pK_a values.

The data displayed in **Figure 6** simultaneously illustrates two important findings: the first is that (TriNOx)Al (**1**) reacts with all the surveyed alcohols (and presumably alcohols in general) faster than (TriNOx)Ga (**2**). This is most likely a result of the higher Lewis acidity of **1** compared to **2**. This trend can be directly observed in **Figure 7**, which plots the reaction profiles of isopropanol reacting with complex **1** and **2**, the former of which is more Lewis acidic than the latter. One can clearly see that the more Lewis acidic complex **1** sees a faster reaction with isopropanol than complex **2** does.

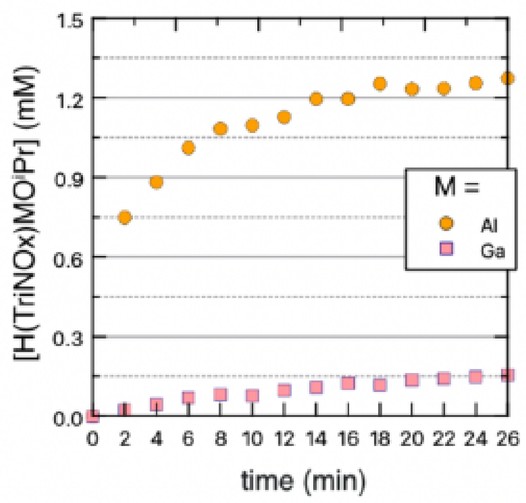

Figure 7. Reaction profiles of complexes **1** and **2** reacting with isopropanol in C_6D_6 at 20°C.

The second finding is that alcohol acidity leads to a positive correlation with reaction rate; in other words, the more acidic the alcohol, the faster it undergoes reaction with (TriNOx)M. **Figure 8** directly illustrates this; it plots the reaction profiles of complex **2** reacting with each of the three alcohols utilized in these kinetics experiments, each of which differ in p*K*$_a$ by one or two units.

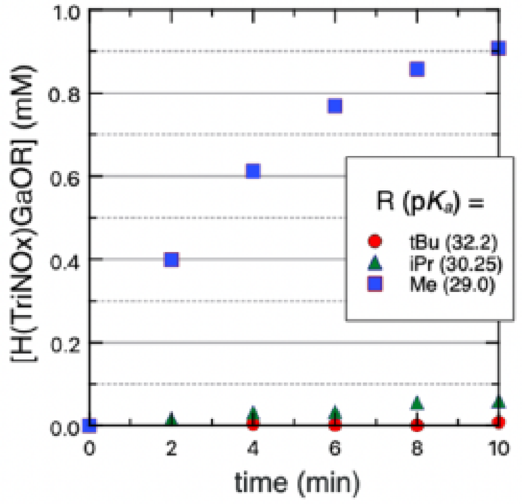

Figure 8. Reaction profiles of *tert*-butanol, isopropanol, and methanol reacting with complex **2** in C_6D_6 at 20°C.

The proposed exponential relationship between initial rate and alcohol acidity, plotted in **Figure 6**, needs to be further verified with more data points, ideally with the reactions of benzyl alcohol, 2,2,2-trifluoroethanol, and others, with complexes **1** and **2**. However, initial investigations into the kinetics of these reactions show that the reaction rates are far too fast for our NMR spectrometer to observe, since it is equipped with a sample loader that requires 30 seconds to inject the sample into the magnet (the reactions are nearly complete by that point).

The mechanistic implications of these findings align with those computationally explored in Maenaga & Graves; the gas phase, B3LYP calculated activation barrier of the reaction of **1** with *tert*-butanol was reported as 27.7 kcal/mol, while the same barrier for the reaction of **2** with phenol was 11.1 kcal/mol.[45] This suggests that alcohol acidity lowers the energetic height activation barrier in an impressive way — even in reaction with the less Lewis acidic, less reactive complex **2**, the higher alcohol acidity of phenol compared to *tert*-butanol lowered the activation barrier by 16.6 kcal/mol. This lowering in activation barrier implies faster reaction rates, which is exactly what we have reported here: reactions of **1** and **2** with more acidic alcohols results in faster initial rates of reaction.

2.5 Screening of O–H bond activation across range of alcohols elucidates the relationship between O–H bond acidity and reaction equilibrium constant

To explore the origin of the difference in reactivity between **1** and **2** towards alcohols, we set out to screen a range of alcohols with varying acidities with the two complexes, using the methods detailed in section 4.3. Based on our initial observations, we expected that **1** would exhibit higher reactivity towards alcohols across the range of acidity than **2** does; we also predicted that as O–H pK_a decreased, the K_{eq} of a given reaction would increase.

We selected alcohols that ranged from the least acidic alcohol listed in the Bordwell DMSO pK_a literature (*tert*-butanol, pK_a = 32.2) to phenol (pK_a = 18.0), the alcohol with which both **1** and **2** react completely. The alcohols we reacted with **1** and **2**, their corresponding pK_a values, the % conversion of each reaction, and the K_{eq} and pK_{eq} of each reaction is recorded in **Table 2**.

Table 2. Percent conversion, K_{eq}, and pK_{eq} values of reactions of various alcohols with compounds **1** and **2**. All reactions were run in benzene-d6 at room temperature. Experiments were performed once (n = 1); preliminary experiments show no reason to believe exceedingly low deviation occurs from these reported values.

	pK_a	**reaction with 1**			**reaction with 2**		
substrate	(DMSO)[47]	conversion, %	K_{eq}	pK_{eq}	conversion, %	K_{eq}	pK_{eq}
^{t}BuOH	32.2	78	1.08	0.0334	21	0.056	1.251
^{i}PrOH	30.25	100	—		28	0.085	1.071
MeOH	29.0	100	—		35	0.138	0.860
BnOH	28.15	100	—		56	0.482	0.3170
CF_3CH_2OH	23.45	100	—		78	2.686	0.4291
4-methoxyphenol	19.1	100	—		100	—	
phenol	18.0	100	—		100	—	

*The pK_a of benzyl alcohol in DMSO is not listed in the Bordwell pK_a compendium[47]. The value reported is approximated based on a set of electronic calculations performed in Gaussian 16. The prediction is based on a linear fit that plotted pK_a values derived from values of ΔG calculated by the G4 compound method to the Bordwell DMSO pK_a. See section 4.4 for computational details.

The data in **Table 2** is presented in **Figure 9**, which clearly illustrates that complex **1** exhibits higher reactivity towards all of the alcohols than **2** does. We attribute this to the difference in metal center Lewis acidity between the complexes. The oxygen atom of the alcohol will coordinate to the more Lewis acidic Al center in complex **1** more favorably than it will to the less Lewis acidic Ga atom in complex **2**; this manifests as the reaction coordinate energy of the alcohol-**1** adduct intermediate being lower than the energy of the alcohol-**2** adduct intermediate, which is also a computational finding of Maenaga & Graves. In their work, they calculated the ^{t}BuOH•**1** adduct intermediate to have a free energy of -14.3 kcal/mol (referenced to a zero-energy that represents the sum of the free energies of the isolated starting materials), and the ^{t}BuOH•**2** adduct intermediate to have a free energy of -12.7 kcal/mol — a difference of 1.6 kcal/mol.

More importantly, **Figure 9** displays the following trend, particularly with complex **2**: as alcohol pK_a value increases, reactivity (best represented by % conversion) with both **1** and **2** decrease. Since complex **2** is less reactive with alcohols, we get a more diverse set of % conversion values from their reactions, and we were able to examine the relationship between the K_{eq} of a reaction of **2** with an alcohol and the alcohol's pK_a. **Figure 10** suggests a possible linear relationship between the pK_{eq} of reaction and the pK_a of the alcohol substrate.

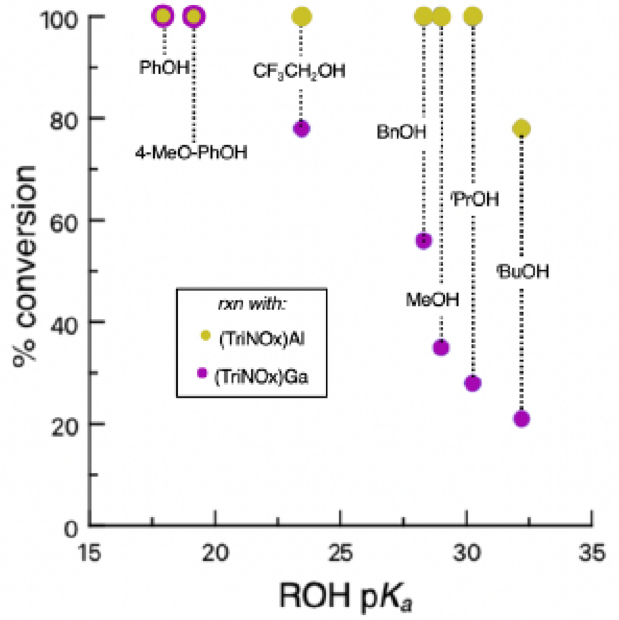

Figure 9. The % conversion of the starting complexes to their corresponding alcohol products, plotted against the pK_a of the alcohol substrate.

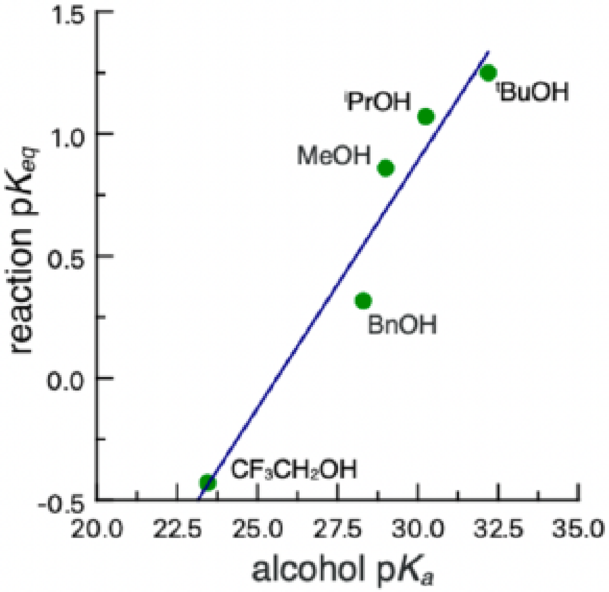

Figure 10. Negative logarithm of the equilibrium constant of reactions of **2** with alcohols of varying acidity plotted against the alcohol substrate pK_a value. The equation of best fit of this line is $y = 0.203x - 5.19$, with $R^2 = 0.943$. Since $n = 1$ for these experiments, there are no error bars provided.

While we suspect that there is a physical origin to the linear relationship between reaction pK_{eq} and alcohol pK_a presented in **Figure 10**, we do not present an explanation as to what this origin may be. More research is needed to make such a claim.

The findings presented here also align well with the findings of Maenaga & Graves regarding reaction thermodynamics: they found that the O–H activation of phenol (pK_a = 18.0) by **2** is 3.0 kcal/mol more exergonic than the O–H activation of *tert*-butanol (pK_a = 32.2) by **1**, and that the ΔG for complete formation of **6** is -28.6 kcal/mol, and for **3**, -23.3 kcal/mol. In other words, the reaction with the more acidic alcohol substrate (phenol) is more spontaneous than the reaction with the less acidic alcohol (*tert*-butanol). Similarly to the kinetic findings, the acidity of the alcohol overpowers the unreactivity of **2** compared to **1** — in this thermodynamic case, particularly when it comes to influencing reaction exergonicity and therefore K_{eq}. Our experimental observation of higher values of K_{eq} associated with more acidic alcohols, regardless of complex metal center, align with the computational findings of higher reaction exergonicity associated with acidic alcohols.

3. Conclusion & Future Work

The syntheses of a series of alcohol addition products of aluminum and gallium tripodal tris(nitroxide) complexes with simple alcohols were performed. Via element-ligand cooperative chemistry, the complexes (TriNOx)Al (**1**) and (TriNOx)Ga (**2**) facilitate the O–H bond activation of alcohols of varying acidities. Early observations suggested that identity of the complex metal center and acidity of the alcohol have major roles in affecting reaction. To study this, kinetic and equilibrium experiments were run with the utilization of ^{1}H NMR spectroscopy. Utilizing reaction progress kinetic analysis methods to record the increase in concentrations of H(TriNOx)MOR products, the kinetic experiments revealed that reactions of *tert*-butanol, isopropanol, and methanol with **1** are globally faster than those with **2**, most likely due the presence of a more Lewis acidic metal center in **1**. These experiments also confirmed the computationally predicted result that alcohols of higher acidity display faster reaction kinetics. Also using ^{1}H NMR spectroscopy, % conversion and equilibrium constants of the reactions of **1** and **2** with seven alcohols ranging in acidity from pK_a = 18.0 to pK_a = 32.2 were determined. Positive relationships between metal center Lewis acidity and alcohol acidity were observed; both higher metal center Lewis acidity and alcohol acidity result in larger values for reaction K_{eq}. Additionally, a brief kinetic isotope experiment was performed on the reaction of *tert*-butanol with complex **1** — this uncovered a small KIE ($k_h/k_d = 1.18$). This value reveals a key mechanistic insight: the transition state of the O–H bond activation event is significantly nonlinear, and thus does not result in much of a KIE. This experimentally determined value agrees with the square-like transition state previously predicted via computational methods.

As mentioned previously mentioned, immediate future work will focus on expanding the range of alcohols we react with the (TriNOx)M complexes. This will involve performing the same kinetics experiments outlined above with alcohols of different acidities than the ones tested in this work. Since alcohols more acidic than methanol react faster than the time it takes for the automated sample loader to inject the sample into the NMR spectrometer, we will either have to use an instrument that does not have an automated sample loader, or cool down the reaction to a lower temperature so that the initial rates are not faster than the automated sample loader. Additionally, we will need to implement the correlation curve of the computationally predicted pK_a values to Bordwell literature DMSO pK_a values, since the Bordwell literature lacks data on alcohols of acidities above pK_a = 32.2, between pK_a = 29.0 and pK_a = 24.0, and between pK_a = 23.0 and pK_a = 20.0. We can use this correlation (i.e., the linear fit relationship in **Figure 12**) to predict the structures of alcohols that will have pK_a values in these ranges. This will allow us to have more data points to further support our claims based on the kinetics and equilibrium experiments.

To truly test the effect metal center Lewis acidity has on both kinetics and equilibria, it would be best to have more than just two (TriNOx)M complexes (M = Al and Ga). We plan on reimplementing the synthesis of (TriNOx)In, and designing and preforming a synthesis of (TriNOx)B, in order to react the same set of alcohols with these new complexes and see how the reactivity compares what we see with complex **1** and **2**. Importantly, this will involve the quantification of the Lewis acidity of all four of these (TriNOx)M complexes (M = B, Al, Ga, In), with various methods, such as the Gutman-Beckett method,[43,44] the Childs method,[48] and a novel fluorescence method;[49,50] this is to ensure that any relationship we find between reaction rate or equilibrium and Lewis acidity is founded on quantitatively sound grounds.

To further explore the mechanism and thermodynamics of the O–H (and potentially E–H) bond activation demonstrated by (TriNOx)M, future work will consist of determining the reaction order of the reaction of (TriNOx)M with an alcohol substrate. Running the same types of kinetics experiments (section 2.3) while changing the initial concentrations of alcohol or (TriNOx)M will allow us to determine reaction order with respect to the reactants. Performing these experiments will allow us to quantitatively determine rate equations and rate constants for these reactions. Additionally, we plan on experimentally deriving the Gibbs energy, enthalpy, and entropy of activation of these chemical systems by running these kinetic experiments at different temperatures and implementing the Eyring equation and the concepts of transition state theory. Finally, if we determine the equilibrium constant (the same way we have done so in section 2.4) of a given reaction of (TriNOx)M with an alcohol at different temperatures, we can perform a van't Hoff analysis and obtain the thermodynamic parameters of this family of chemical reactions.

To further explore the scope of E–H bond activation possible by the (TriNOx)M complex, we plan to eventually perform the same equilibrium and kinetics experiments with N–H, S–H, and C_{sp}–H containing substrates. Preliminary investigations show that both complexes **1** and **2** are capable of activating N–H bonds of sulfonamides and carbamates. Additionally, complex **1** may be able to react with simple amines, such as diethylamine, under strict conditions. This screening process will increase the likelihood of finding new ways to implement the (TriNOx)M complex as a sustainable catalyst, which is the ultimate goal of this research project. This project is ripe with potential research directions, and there are many realms in which to explore this fascinating chemical system.

4. Materials & Methods

4.1 Physical measurements

All ^1H NMR spectra were recorded at 293 K using a Bruker 400 MHz spectrometer (399.78 MHz for ^1H). Chemical shifts were referenced to residual solvent. s = singlet, bs = broad singlet, d = doublet, t = triplet, q = quartet, p = pentet, td = triplet of doublets, m = multiplet, bm = broad multiplet, at = apparent triplet. X-ray diffraction data was collected either on a Bruker APEXII CCD area detector or a Rigaku XtaLAB Synergy-S diffractometer equipped with an HPC area detector, both employing graphite-monochromated Mo-Kα radiation (λ=0.71073Å) at 100 K.

4.2. Preparation of compounds

All reactions and manipulations were performed under an inert atmosphere (N_2) using standard Schlenk techniques or in a Vacuum Atmospheres, Inc. NextGen drybox equipped with oxygen and moisture purifier systems. Glassware was dried overnight at 150°C before use. C_6D_6, $CDCl_3$, and THF-d8 were degassed and stored over 3 Å and 4 Å molecular sieves prior to use. Tetrahydrofuran, toluene, dichloromethane, hexane, and pentane were sparged for 20 min with dry argon and dried using a commercial two-column solvent purification system comprising of two columns packed with neutral alumina (for tetrahydrofuran and dichloromethane) or Q5 reactant then neutral alumina (for hexanes, toluene, and pentane). Any benzene or pyridine used was purchased anhydrous and further dried over 4 Å molecular sieves prior to use. The $(TriNOx)H_3$ ligand precursor was prepared according to literature procedures.[39] All other reagents were purchased from commercial sources and used as received. Liquid reagents were stored over 4 Å molecular sieves prior to use.

4.2.1 Synthesis of H(TriNOx)AlOtBu (3)

To synthesize **3**, three molar equivalents (38.8 mg, 0.524 mmol) of *tert*-butanol were added to 100 mg of **1** (0.175 mmol) dissolved in toluene in a vial and were allowed to stir overnight at room temperature. Solvent was removed from the reaction vessel via vacuum evaporation and 88.8 mg of solid **3** was collected (81% yield). A ^{1}H NMR was obtained in C_6D_6 (**Figure S1**). ^{1}H NMR (C_6D_6): δ 10.95 (bs, 1H), δ 7.82 (d, $J = 8.28$ Hz, 3H), δ 7.02 (d, $J = 7.6$ Hz, 3H), δ 6.89 (t, J = 7.4, 3H), δ 6.70 (d, $J = 7.64$ Hz, 3H), δ 4.71 (d, $J = 11.72$ Hz, 3H), δ 2.24 (dd, $J = 11.2$ Hz, $J = 9.6$ Hz, 3H), δ 1.81 (s, 9H, $OC(CH_3)_3$), δ 1.00 (s, 27H, $C(CH_3)_3$). A proton-decoupled ^{13}C NMR was also obtained in C_6D_6 (**Figure S17**). ^{13}C NMR (C_6D_6): δ 154.27 (1C), δ 132.08 (3C), δ 131.72 (3C), δ 129.49 (3C), δ 126.08 (3C), δ 124.34 (3C), δ 61.52 (3C), δ 57.12 (3C), δ 34.63 (3C), δ 26.73 (9C). Single-crystal structure obtained via XRCD has been previously reported; the structure can be found in **Figure S21A**.

4.2.2 Synthesis of H(TriNOx)AlOPh (5)

One molar equivalent (16.5 mg, 0.175 mmol) of phenol was added to 100 mg of **1** (0.175 mmol) dissolved in toluene in a vial. The reaction was allowed to stir overnight at room temperature. The product precipitates out of solution as a white solid, which is collected over a glass frit via vacuum filtration. The collected solid is then washed with cold hexane, and then transferred to a vial with pentane to ensure maximum collection from the frit. The pentane is then evaporated from the suspension, leaving the white solid behind. A yield of 50.0 mg (43% yield) was recovered. An ^{1}H NMR was obtained in $CDCl_3$ (**Figure S5**). ^{1}H NMR ($CDCl_3$): δ 11.02 (bs, 1H), δ 5.03 (d, $J = 11.8$ Hz), δ 3.20 (at, $J = 10.4$ Hz, $J = 11.0$ Hz, 3H), δ 0.73 (s, 27H, $C(CH_3)_3$). ^{13}C NMR ($CDCl_3$): δ 153.06 (1C), δ 132.33 (2C), δ 129.18 (3C), δ 129.18 (3C), δ 128.47 (3C), δ 128.37 (3C), δ 125.68 (1C), δ 124.55 (2C), δ 68.13 (3C), δ 61.66 (3C), δ 26.22 (9C).

*4.2.3 Crystallization of H(TriNOx)AlOPh (**5**)*

50 mg (0.0873 mmol) of **1** was dissolved in 5 mL of toluene, and 10.1 mg (0.107 mmol) of phenol was dissolved in 2 mL of toluene. The phenol solution was then layered onto the solution of **1** and allowed to rest at room temperature for one month, at which point translucent, colorless, sand-like crystals had crashed out. The crystals were suitable for X-ray diffraction, and a single-crystal structure was collected (**Figure 3**). Its collection parameters can be found in **Table S1**.

*4.2.4 Synthesis of H(TriNOx)GaOPh (**6**)*

Approximately one molar equivalent (15.4mg, 0.164 mmol) of phenol was added to 100 mg of **2** (0.163 mmol) dissolved in toluene in a vial. The reaction was allowed to stir overnight at room temperature. The product precipitates out of solution as a white solid, which is collected over a glass frit via vacuum filtration. The collected solid is then washed with cold hexane, and then transferred to a vial with pentane to ensure maximum collection from the frit. The pentane is then evaporated from the suspension, leaving the white solid behind. A yield of 77.4 mg (67% yield) was recovered. An ^{1}H NMR was obtained in $CDCl_3$ (**Figure S4**). ^{1}H NMR ($CDCl_3$): δ 10.89 & 10.58 (dbs, 1H), δ 4.94 (d, $J = 11.5$ Hz), δ 3.12 (at, $J = 9.6$ Hz, $J = 21$ Hz, 3H), δ 0.66 (s, 27H, $C(CH_3)_3$). Aryl protons are not reported due to poor peak definition in the chemical shift range of δ 8.0 – 6.5 ppm. A single-crystal structure obtained via XRCD has been previously reported; the structure can be found in **Figure S17B**. ^{13}C NMR ($CDCl_3$): δ 149.58 (1C), δ 59.29 (3C), δ 56.19 (3C), δ 26.44 (9C). Aryl protons are not reported due to poor peak definition in the chemical shift range of δ 8.0 – 6.5 ppm.

4.2.5 Synthesis of H(TriNOx)AlOBn (7)

Approximately one molar equivalent (19.0 mg, 0.1757 mmol) of benzyl alcohol was added to 99.7 mg of **1** (0.174 mmol) dissolved in toluene in a vial. The reaction was allowed to stir overnight at room temperature. The product precipitates out of solution as a white solid, which is collected over a glass frit via vacuum filtration. The collected solid is then washed with cold hexane, and then transferred to a vial with pentane to ensure maximum collection from the frit. The pentane is then evaporated from the suspension, leaving the white solid behind. A yield of 23.7 mg (20% yield) was recovered. An ^{1}H NMR was obtained in C_6D_6 (**Figure S6**). ^{1}H NMR (C_6D_6): δ 11.04 (bd, 1H), δ 7.95 (d, $J = 6.4$ Hz, 2H), δ 7.87 (d, $J = 8.4$ Hz, 3H), δ 7.39 (t, $J = 7.4$ Hz, 2H), δ 7.02 (d, $J = 7.02$ Hz, 3H), δ 6.90 (t, $J = 7.0$ Hz, 3H), δ 6.72 (d, $J = 8.8$ Hz, 3H), δ 5.61(d, $J = 14.4$ Hz, 1H), δ 5.56 (d, $J = 14.4$ Hz, 1H), δ 4.70 (d, $J = 12$ Hz), δ 2.27 (dd, $J = 10.8$ Hz, $J = 10.4$ Hz, 3H), δ 0.97 (s, 27H, $C(CH_3)_3$). A proton-decoupled ^{13}C NMR was also obtained in C_6D_6 (**Figure S20**). ^{13}C NMR (C_6D_6): δ 154.01 (2C), δ 132.18 (3C), δ 131.68 (3C), δ 129.60 (3C), δ 126.74 (2C), δ 126.07 (2C), δ 1245.64 (1C), δ 124.54 (3C), δ 61.66 (3C), δ 57.05 (3C), δ 26.54 (9C).

4.2.6 Synthesis of H(TriNOx)GaOCH$_2$CF$_3$ for ^{1}H NMR spectrum reference collection

Three molar equivalents (15 mg, 0.15 mmol) of 2,2,2-trifluoroethanol were added to 30.8 mg of **2** (0.05 mmol) dissolved in toluene in a vial. The reaction was allowed to stir overnight at room temperature. The product precipitates out of solution as a white solid, which is collect over a glass frit via vacuum filtration. The collected solid is then washed with cold hexane, and then transferred to a vial with pentane to ensure maximum collection from the frit. The pentane is then evaporated from the suspension, leaving the white solid behind. No yield was recorded, as all the solid was subsequently dissolved in CDCl$_3$ and then analyzed by ^{1}H NMR (**Figure S10**). ^{1}H NMR (CDCl$_3$): δ 11.02 & 10.65 (bs, 1H), δ 5.00 (dd, J = 11.2 Hz, J = 10.0 Hz), δ 4.27 (dp, J = 62.4, J = 9.6, 1H), δ 3.18 (dd, J = 22.8 Hz, J = 13.2 Hz, 3H), δ 0.73 (s, 27H, C(CH$_3$)$_3$). Aryl protons are not reported due to poor peak definition in the chemical shift range of δ 8.0 – 6.5 ppm.

4.3.1 Implementing ^{1}H NMR spectroscopy to perform reaction progress kinetic analyses and calculate reaction equilibrium constants

Here we describe how we utilized ^{1}H NMR spectroscopy to track both the kinetics of the reactions between compounds **1** and **2** with various alcohols, as well as the equilibrium constants of these reactions. To track kinetics, we implemented techniques closely related to what is known as reaction progress kinetic analysis (RPKA), which involves the analysis of reactant and product concentration as a function of time. This concentration data is then processed to be transformed into variables convenient for visual analysis,[51] i.e., graphs that plot product concentration vs. time. In this study, we measure the concentration of (TriNOx)M-alcohol products over time using ^{1}H NMR spectroscopy; the intensities of the ^{1}H signals originating from these products are directly proportional to product concentration, which goes on to be calculated exactly with the implementation of an internal standard of known concentration (see *4.3.2*). To determine equilibrium constants, we analyzed signals of protons from the reactants and products that originate from the same positions on the TriNOx ligand of each species to determine the reactant-to-product ratios. However, an internal standard isn't necessary to determine the concentration of either specie if the only two species in solution are the reactant (**1** or **2**) and its alcohol product; fortunately, this is consistently the case in these studies. We simply took the reactant-to-product ratios and normalized them to the initial loaded concentration of reactant (see *4.3.3*).

To perform these kinetic and equilibrium experiments, we needed to choose strong, ideally isolated NMR peaks that accurately represent the reactants and products. **Figure 8** illustrates that the chemical system we study in this thesis is ideal for this task; not only are there two highly isolated signals that represent the diastereotopic ligand methylene protons, but the more upfield one reliably undergoes significant, "diagnostic" migration to a more upfield chemical shift and experiences an additional J coupling upon product formation. Furthermore, the signals of the protons on the product alkoxylate ligand (-OR) are usually quite unique, and can be easily analyzed to record the increase in concentration of the product.

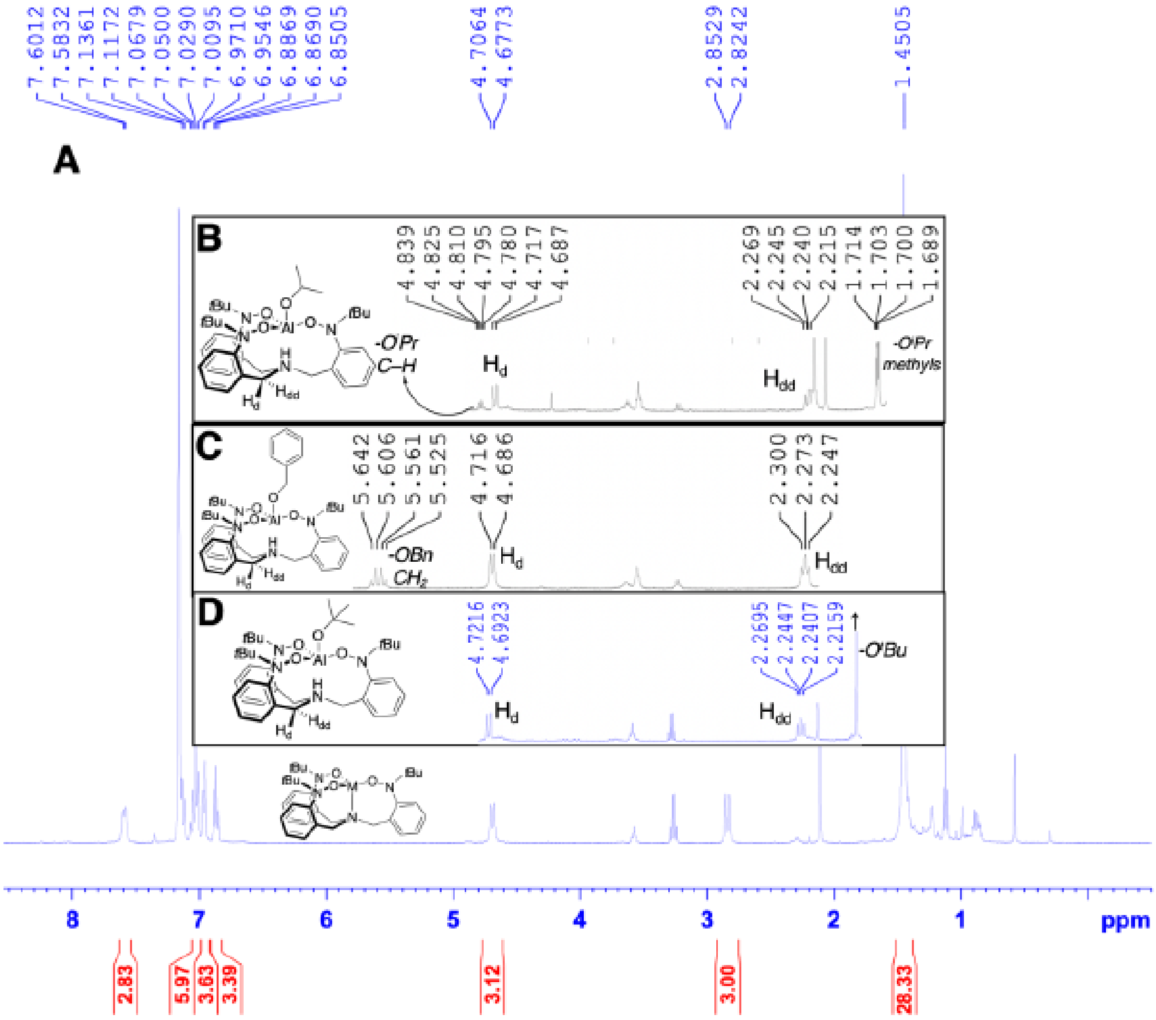

Figure 8. ^{1}H NMR spectrum of **A.** (TriNOx)M, and the diagnostic signal regions of its alcohol products H(TriNOx)AlO^{i}Pr (**B.**), H(TriNOx)AlOBn (**C**), and H(TriNOx)AlO^{t}Bu (**D**) in C_6D_6. Each upfield (TriNOx)M diastereotopic methylene 3H doublet (~δ2.84 ppm) consistently migrates to a more upfield chemical shift upon product formation with an alcohol; the more upfield doublet (~δ2.45) ppm also gains a coupling to the basal N-H, turning into a doublet of doublets. In **B.**, **C.**, and **D.**, the unique alkoxylate ligand signals of -O^{i}Pr, -OBn, and O^{t}Bu, respectively, are indicated.

As illustrated in **Figure 8**, the signals that originate from protons on the product alkoxylate ligands usually appear visually isolated and strong on the NMR spectra. These signals are ideal to analyze and track the increase in product concentration when performing the kinetics experiments. However, when calculating reactant-to-product ratios, the diastereotopic methylene signals of both the reactant and product are more applicable due to the following diagnostic property: the more upfield methylene doublet turns into a doublet of doublets ($J_{Hd\text{-}Hdd}$ = 11.6 Hz, $J_{NH\text{-}Hdd}$ = 9.6 Hz) and consistently migrates to an even more upfield chemical shift, around δ 2.45 ppm, upon alcohol product formation. When (TriNOx)M is in equilibrium with its given alcohol product, the upfield methylene signals of both the starting complex and the product are present in the NMR spectrum; these can be integrated, and a ratio to reactant-to-product can be determined. This ratio can be normalized to the initial/maximum concentration of (TriNOx)M/product, and thus, equilibrium concentrations and equilibrium constants can be calculated.

*4.3.2 Preparation of stock solutions of **1**, **2**, hexamethylcyclotrisiloxane internal standard, and alcohols*

To ensure accurate loadings of starting materials for both the kinetics and equilibrium determination experiments, stock solutions of compounds **1** and **2**, the selected alcohol substrates, and the internal standard (i.s.), hexamethylcyclotrisiloxane, were prepared in C_6D_6; this way reactants could be dispensed using volumetrically precise, gastight syringes. **Table 3** lists the concentrations of all stock solutions prepared to perform these experiments; it also lists the masses of reactants and volumes of solvent that were used each time a new stock solution was prepared.

Table 3. Concentrations of stock solutions prepared for kinetics and equilibrium determination experiments.

compound	concentration (mM)	mass dissolved (mg)	mmol of compound	volume of C_6D_6 (mL)
1	9.0	30.9	0.054	6.0
2	9.0	33.2	0.054	6.0
hexamethylcyclotrisiloxane	6.0	6.7	0.030	5.0
***tert*-butanol**	36.0	8.0	0.108	3.0
***tert*-butanol-OD**	35.5	12.0	0.160	4.5
isopropanol	36.6	4.4	0.073	2.0
methanol	35.9	2.3	0.072	2.0
benzyl alcohol	36.1	7.8	0.063	2.0
2,2,2-trifluoroethanol	36.7	2.2	0.022	0.6
4-methoxyphenol	34.8	2.7	0.022	0.6
phenol	35.4	2.0	0.021	0.6

To prepare a stock solution for a given compound, its mass indicated in **Table 3** was weighed out and dissolved in the volume of C_6D_6 indicated and stored in a vial.

4.3.3 Procedure for kinetics experiments (including KIE experiments)

We used alcohols that had pK_a values listed in the Bordwell collection of experimentally derived pK_a values in a DMSO solvent.[47] There is currently no reliable way to experimentally measure the acidity of a compound in nonpolar solvents such as benzene (the solvent used in this experiment), and thus there is no reliable source of directly applicable pK_a values. However, there should ideally be a consistent correlation (perhaps a proportional relationship) between the relative acidities of alcohols in DMSO and in benzene; therefore, we believe that using a non-benzene pK_a scale should be sufficient. Note that this is a foundational assumption we make in order to go forth with this experiment.

For a given experiment, 0.5 mL of the stock solution of **1** or **2** and 0.125 mL of i.s. stock solution were dispensed into an air-free NMR tube, which was then sealed with a screw cap containing a septum. Meanwhile, a syringe was loaded with 0.125 mL of alcohol (^{t}BuOH, ^{i}PrOH, or MeOH) stock solution, and then sealed by penetrating the syringe tip into a rubber stopper. These two vessels were then transported to an NMR spectrometer.

An ^{1}H NMR spectrum was recorded of the solution in the NMR tube before the dispensing of the alcohol; the analyte signals on this spectrum represent the $t = 0$ data point. Then, immediately after dispensing the preloaded volume of alcohol solution into the tube through the septum and inverting the tube once, ^{1}H NMR spectra of the reactions were recorded at two-minute time intervals, with the exception of the reactions of **1** with MeOH — these reactions were probed at one-minute intervals. Spectra were recorded for at least 10 minutes with the spectrometer temperature probe set to 20°C. For each experiment, $[\mathbf{1}]_0$ or $[\mathbf{2}]_0 = [\mathrm{ROH}]_0 = 6$ mM, and [i.s.] = 1 mM. The total reaction volume is 0.75 mL.

For each NMR spectra recorded, protons on the apical alkoxylate ligands (-OR) of the products were analyzed to calculate the concentration of product in solution at each time interval; these signals are the 9H *tert*-butoxyl (-O^{t}Bu) singlet at δ1.81 ppm for products **3** and **4**, the 6H isopropoxyl (-O^{i}Pr) doublet of doublets at δ1.70 ppm for the H(TriNOx)MO^{i}Pr products, and the 3H methoxyl (-OMe) singlet at δ4.38 ppm. These apical ligand signals grow into the spectrum as their respective formation reactions proceed, and are integrated against the 18H hexamethylcyclotrisiloxane i.s., which is always loaded into the reaction at 1 mM concentration. Using **Equation 1**, we can directly calculate the concentration of product forming in solution:

$$[product] = \frac{\frac{product\ -OR\ signal\ integral}{no.\ of\ -OR\ protons} * [i.s.]}{\frac{i.s.\ signal\ integral}{no.\ of\ i.s.\ protons}} \qquad \textbf{(Eq. 1)}$$

Note that the integrals must be normalized; in our studies we normalize the i.s. signal to 1.00. Since the [i.s.] in all trials is 1 mM, **Equation 1** can be simplified to the following expression (**Equation 2**):

$$[product] = \frac{\frac{product\ -OR\ signal\ integral}{no.\ of\ -OR\ protons} * [1\ mM]}{\frac{1}{18}} = 18 * \frac{product\ -OR\ signal\ integral}{no.\ of\ -OR\ protons} \qquad \textbf{(Eq. 2)}$$

This equation allows for the plotting of [H(TriNOx)MOR] vs. reaction time, which is the primary source of data for kinetic analysis.

For the majority of the data, initial rates were linearly approximated by taking the best fit line between the first data point ($t = 2$ min) and the origin ($t = 0$ min). However, for the reactions with *tert*-butanol (for both the KIE and regular kinetics experiments), the best fit lines were taken with more points considered, due to exacerbated error in NMR signals associated with the low concentrations of product **4**.

4.3.4 Procedure for equilibrium constant determination experiments

For a given experiment, 0.5 mL of the stock solution of **1** or **2**, 0.125 mL of i.s. stock solution, and 0.125 mL of alcohol solution were dispensed into a small vial. A small stir bar was added, and the vial was capped; the reaction was allowed to stir at room temperature overnight to ensure completion. The next day, all 0.75 mL of the reaction were taken up into an NMR tube, and an ^{1}H NMR spectrum was recorded. For each spectra, the reactant-to-product integral ratio of the diastereotopic methylene signals and the ligand *tert*-butyl signals were recorded, and then normalized to 6 mM to calculate the concentrations of reactant and product at reaction equilibrium. These concentrations were then plugged into **Equation 3** to determine the reaction equilibrium constant (K_{eq}):

$$K_{eq} = \frac{[\mathrm{H(TriNOx)M{-}OR}]}{[\mathrm{(TriNOx)M}][\mathrm{RO{-}H}]} \qquad \textbf{(Eq. 3)}$$

Note that since the alcohols and the (TriNOx)M reactants were loaded in equimolar stoichiometry, [RO-H] was set equal to [(TriNOx)M] (the integral-based concentration of **1** or **2** in solution) for each K_{eq} calculation.

4.4 Computational detail of alcohol acidity electronic calculations

To approximate the pK_a of benzyl alcohol in DMSO, we implemented electronic structure calculations to attempt to reproduce the pK_a values of alcohols in DMSO listed in the Bordwell literature.[47] All calculations were performed with the Gaussian '16, Revision C.01 program[52] using the G4 compound method[53] with a self-consistent reaction field applied to mimic the electrostatic effects of a DMSO solvent (scrf=solvent=DMSO). The calculations were carried out without symmetry restrictions. The energies used in analysis were the electronic energies with Gibbs free energy corrections at 298 K taken into account.

Free energies of the following alcohols and their corresponding alkoxylates were calculated: *tert*-butanol, isopropanol, ethanol, methanol, 2,2,2-trifluoroethanol, 4-methoxyphenol, phenol, and 1,1,1,3,3,3-hexafluoro-2-propanol. Using the free computed energies, ΔG values (in kcal/mol) were calculated by subtracting the energy of an alcohol from its corresponding alkoxylate; this represents the ΔG of deprotonation of the alcohol. These ΔG values were converted to pK_a values via **Equation 4**; these values were then defined relative to the pK_a of 2,2,2-trifluoroethanol [pK_a(ROH) - pK_a(CF_3CH_2OH)]. Finally, these relative pK_a values were plotted against their Bordwell literature values. This correlation plot can be found in **Figure 9**.

$$\mathrm{p}K_a = -log(10^{\frac{-\Delta G_{deprot}}{1.36424409}}) = \frac{\Delta G_{deprot}}{1.36424409} \qquad \textbf{(Eq. 4)}$$

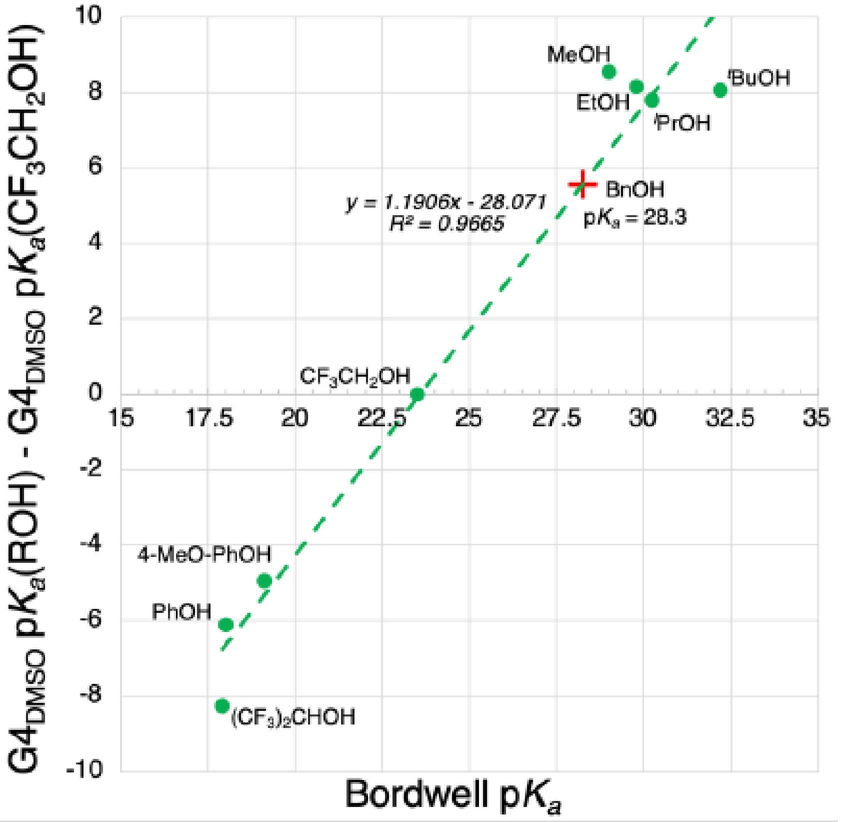

Figure 9. G4 method with SCRF(DMSO) calculated pK_a values (relative to the calculated pKa of 2,2,2-trifluoroethanol) of selected alcohols plotted against Bordwell literature pK_a values in DMSO.[47] The G4 method predicted pK_a value for benzyl alcohol is plotted according to the equation of the line of best fit.

To predict the pK_a of benzyl alcohol, we calculated its ΔG of deprotonation, and solved for its pK_a using the equation of the line of best fit of the correlation plot in **Figure 9**. This predicted pK_a value for benzyl alcohol is plotted with a red + in **Figure 9**; this value is used in the equilibrium experiments (section 2.4).

(17) Weismann, J.; Scharf, L. T.; Gessner, V. H. Cooperative P–H Bond Activation with Ruthenium and Iridium Carbene Complexes. *Organometallics* **2016**, *35* (15), 2507–2515. https://doi.org/10.1021/acs.organomet.6b00408.

(18) Musa, S.; Shaposhnikov, I.; Cohen, S.; Gelman, D. Ligand-Metal Cooperation in PCP Pincer Complexes: Rational Design and Catalytic Activity in Acceptorless Dehydrogenation of Alcohols. *Angew. Chem. Int. Ed.* **2011**, *50* (15), 3533–3537. https://doi.org/10.1002/anie.201007367.

(19) Gutsulyak, D. V.; Piers, W. E.; Borau-Garcia, J.; Parvez, M. Activation of Water, Ammonia, and Other Small Molecules by PC $_{carbene}$ P Nickel Pincer Complexes. *J. Am. Chem. Soc.* **2013**, *135* (32), 11776–11779. https://doi.org/10.1021/ja406742n.

(20) Bichler, B.; Holzhacker, C.; Stöger, B.; Puchberger, M.; Veiros, L. F.; Kirchner, K. Heterolytic Cleavage of Dihydrogen by an Iron(II) PNP Pincer Complex via Metal–Ligand Cooperation. *Organometallics* **2013**, *32* (15), 4114–4121. https://doi.org/10.1021/om400241x.

(21) LeBlanc, F. A.; Berkefeld, A.; Piers, W. E.; Parvez, M. Reactivity of Scandium β-Diketiminate Alkyl Complexes with Carbon Dioxide. *Organometallics* **2012**, *31* (3), 810–818. https://doi.org/10.1021/om2012002.

(22) Vigneswaran, V.; Abhyankar, P. C.; MacMillan, S. N.; Lacy, D. C. H $_2$ Activation across Manganese(I)–C Bonds: Atypical Metal–Ligand Cooperativity in the Aromatization/Dearomatization Paradigm. *Organometallics* **2022**, *41* (1), 67–75. https://doi.org/10.1021/acs.organomet.1c00606.

(23) Dureen, M. A.; Stephan, D. W. Reactions of Boron Amidinates with CO $_2$ and CO and Other Small Molecules. *J. Am. Chem. Soc.* **2010**, *132* (38), 13559–13568. https://doi.org/10.1021/ja1064153.

(24) Swamy, V. S. V. S. N.; Raj, K. V.; Vanka, K.; Sen, S. S.; Roesky, H. W. Silylene Induced Cooperative B–H Bond Activation and Unprecedented Aldehyde C–H Bond Splitting with Amidinate Ring Expansion. *Chem. Commun.* **2019**, *55* (24), 3536–3539. https://doi.org/10.1039/C9CC00296K.

(25) Yao, S.; van Wüllen, C.; Driess, M. Striking Reactivity of Ylide-like Germylene toward Terminal Alkynes: [4+2] Cycloaddition versus C–H Bond Activation. *Chem. Commun.* **2008**, No. 42, 5393. https://doi.org/10.1039/b811952j.

(26) Radzewich, C. E.; Coles, M. P.; Jordan, R. F. Reversible Ethylene Cycloaddition Reactions of Cationic Aluminum β-Diketiminate Complexes. *J. Am. Chem. Soc.* **1998**, *120* (36), 9384–9385. https://doi.org/10.1021/ja9818405.

(27) Abdalla, J. A. B.; Riddlestone, I. M.; Tirfoin, R.; Aldridge, S. Cooperative Bond Activation and Catalytic Reduction of Carbon Dioxide at a Group 13 Metal Center. *Angew. Chem. Int. Ed.* **2015**, *54* (17), 5098–5102. https://doi.org/10.1002/anie.201500570.

(28) Hitzfeld, P. S.; Kretschmer, R. Cooperative H–X Bond Activation by Electron-Precise Aluminium and Gallium Compounds Incorporating Β-Diketiminate Ligands. *Eur. J. Inorg. Chem.* **2020**, *2020* (17), 1624–1630. https://doi.org/10.1002/ejic.201901320.

(29) Feld, J.; Wilson, D. W. N.; Goicoechea, J. M. Contrasting E−H Bond Activation Pathways of a Phosphanyl-Phosphagallene. *Angew. Chem. Int. Ed.* **2021**, *60* (40), 22057–22061. https://doi.org/10.1002/anie.202109334.

(30) Fedushkin, I. L.; Nikipelov, A. S.; Lyssenko, K. A. Reversible Addition of Alkynes to Gallium Complex of Chelating Diamide Ligand. *J. Am. Chem. Soc.* **2010**, *132* (23), 7874–7875. https://doi.org/10.1021/ja103467a.

(31) Piskunov, A. V.; Ershova, I. V.; Fukin, G. K.; Shavyrin, A. S. Addition of Allyl Halides to the New Bis-o-Amidophenolate Gallium(III) Complex. *Inorg. Chem. Commun.* **2013**, *38*, 127–130. https://doi.org/10.1016/j.inoche.2013.10.029.

(32) Sigmund, L. M.; Greb, L. Reversible OH-Bond Activation and Amphoterism by Metal–Ligand Cooperativity of Calix[4]Pyrrolato Aluminate. *Chem. Sci.* **2020**, *11* (35), 9611–9616. https://doi.org/10.1039/D0SC03602A.

(33) Myers, T. W.; Berben, L. A. Aluminum–Ligand Cooperative N–H Bond Activation and an Example of Dehydrogenative Coupling. *J. Am. Chem. Soc.* **2013**, *135* (27), 9988–9990. https://doi.org/10.1021/ja4032874.

(34) Sherbow, T. J.; Carr, C. R.; Saisu, T.; Fettinger, J. C.; Berben, L. A. Insight into Varied Reaction Pathways for O–H and N–H Bond Activation by Bis(Imino)Pyridine Complexes of Al(III). *Organometallics* **2016**, *35* (1), 9–14. https://doi.org/10.1021/acs.organomet.5b00743.

(35) Myers, T. W.; Berben, L. A. Aluminium–Ligand Cooperation Promotes Selective Dehydrogenation of Formic Acid to H $_2$ and CO $_2$. *Chem Sci* **2014**, *5* (7), 2771–2777. https://doi.org/10.1039/C4SC01035C.

(36) Berben, L. A. Catalysis by Aluminum(III) Complexes of Non-Innocent Ligands. *Chem. — Eur. J.* **2014**, *2015* (11), 2734–2742. https://doi.org/10.1002/chem.201405400.

(37) Poitras, A. M.; Bogart, J. A.; Cole, B. E.; Carroll, P. J.; Schelter, E. J.; Graves, C. R. Synthesis and Characterization of Aluminum Complexes of Redox-Active Pyridyl Nitroxide Ligands. *Inorg. Chem.* **2015**, *54* (22), 10901–10908. https://doi.org/10.1021/acs.inorgchem.5b01941.

(38) Kirsh, J.; Woodside, A.; Manor, B.; Carroll, P.; Rablen, P.; Graves, C. Synthesis and Characterization of (PyNO−)2GaCl: A Redox-Active Gallium Complex. *Inorganics* **2018**, *6* (2), 50. https://doi.org/10.3390/inorganics6020050.

(39) Bogart, J. A.; Lippincott, C. A.; Carroll, P. J.; Schelter, E. J. An Operationally Simple Method for Separating the Rare-Earth Elements Neodymium and Dysprosium. *Angew. Chem. Int. Ed.* **2015**, *54* (28), 8222–8225. https://doi.org/10.1002/anie.201501659.

(40) Chen, Q.; Buss, C. E.; Young, V. G.; Fox, S. Synthesis and Structural Studies of Tris-2-Chlorobenzylamine and Tris-2-Bromobenzylamine. *J. Chem. Crystallogr.* **2005**, *35* (3), 177–181. https://doi.org/10.1007/s10870-005-2954-5.

(41) Woodside, A. J.; Smith, M. A.; Herb, T. M.; Manor, B. C.; Carroll, P. J.; Rablen, P. R.; Graves, C. R. Synthesis and Characterization of a Tripodal Tris(Nitroxide) Aluminum Complex and Its Catalytic Activity toward Carbonyl Hydroboration. *Organometallics* **2019**, *38* (5), 1017–1020. https://doi.org/10.1021/acs.organomet.8b00933.

(42) Woodside, A. J.; Smith, M. A.; Herb, T. M.; Manor, B. C.; Carroll, P. J.; Rablen, P. R.; Graves, C. R. Synthesis and Characterization of a Tripodal Tris(Nitroxide) Aluminum Complex and Its Catalytic Activity toward Carbonyl Hydroboration. *Organometallics* **2019**, *38* (5), 1017–1020. https://doi.org/10.1021/acs.organomet.8b00933.

(43) Gutmann, V. Solvent Effects on the Reactivities of Organometallic Compounds. *Coord. Chem. Rev.* **1976**, *18* (2), 225–255. https://doi.org/10.1016/S0010-8545(00)82045-7.

(44) Beckett, M. A.; Strickland, G. C.; Holland, J. R.; Sukumar Varma, K. A Convenient n.m.r. Method for the Measurement of Lewis Acidity at Boron Centres: Correlation of Reaction Rates of Lewis Acid Initiated Epoxide Polymerizations with Lewis Acidity. *Polymer* **1996**, *37* (20), 4629–4631. https://doi.org/10.1016/0032-3861(96)00323-0.

(45) Maenaga, M. L.; Graves, C. R. A Mechanistic Study: O–H Bond Activation by Tripodal Tris(Nitroxide) Aluminum and Gallium Complexes.

(46) Anslyn, E. V.; Dougherty, D. A. Isotope Effects for Linear vs, Non-Linear Transition States. In *Modern Physical Organic Chemistry*; University Science Books, 2006; p 428.

(47) Bordwell, F. G. Equilibrium Acidities in Dimethyl Sulfoxide Solution. *Acc. Chem. Res.* **1988**, *21* (12), 456–463. https://doi.org/10.1021/ar00156a004.

(48) Childs, R. F.; Mulholland, D. L.; Nixon, A. The Lewis Acid Complexes of α,β-Unsaturated Carbonyl and Nitrile Compounds. A Nuclear Magnetic Resonance Study. *Can. J. Chem.* **1982**, *60* (6), 801–808. https://doi.org/10.1139/v82-117.

(49) Gaffen, J. R.; Bentley, J. N.; Torres, L. C.; Chu, C.; Baumgartner, T.; Caputo, C. B. A Simple and Effective Method of Determining Lewis Acidity by Using Fluorescence. *Chem* **2019**, *5* (6), 1567–1583. https://doi.org/10.1016/j.chempr.2019.03.022.

(50) Bentley, J. N.; Elgadi, S. A.; Gaffen, J. R.; Demay-Drouhard, P.; Baumgartner, T.; Caputo, C. B. Fluorescent Lewis Adducts: A Practical Guide to Relative Lewis Acidity. *Organometallics* **2020**, *39* (20), 3645–3655. https://doi.org/10.1021/acs.organomet.0c00389.

(51) Ben-Tal, Y.; Boaler, P. J.; Dale, H. J. A.; Dooley, R. E.; Fohn, N. A.; Gao, Y.; García-Domínguez, A.; Grant, K. M.; Hall, A. M. R.; Hayes, H. L. D.; Kucharski, M. M.; Wei, R.; Lloyd-Jones, G. C. Mechanistic Analysis by NMR Spectroscopy: A Users Guide. *Prog. Nucl. Magn. Reson. Spectrosc.* **2022**, *129*, 28–106. https://doi.org/10.1016/j.pnmrs.2022.01.001.

(52) Frisch, M. J.; Trucks, G. W.; Schlegel, H. B.; Scuseria, G. E.; Robb, M. A.; Cheeseman, J. R.; Scalmani, G.; Barone, V.; Petersson, G. A.; Nakatsuji, H.; Li, X.; Caricato, M.; Marenich, A. V.; Bloino, J.; Janesko, B. G.; Gomperts, R.; Mennucci, B.; Hratchian, H. P.; Ortiz, J. V.; Izmaylov, A. F.; Sonnenberg, J. L.; Williams-Young, D.; Ding, F.; Lipparini, F.; Egidi, F.; Goings, J.; Peng, B.; Petrone, A.; Henderson, T.; Ranasinghe, D.; Zakrzewski, V. G.; Gao, J.; Rega, N.; Zheng, G.; Liang, W.; Hada, M.; Ehara, M.; Toyota, K.; Fukuda, R.; Hasegawa, J.; Ishida, M.; Nakajima, T.; Honda, Y.; Kitao, O.; Nakai, H.; Vreven, T.; Throssell, K.; Montgomery, J. A., Jr.; Peralta, J. E.; Ogliaro, F.; Bearpark, M. J.; Heyd, J. J.; Brothers, E. N.; Kudin, K. N.; Staroverov, V. N.; Keith, T. A.; Kobayashi, R.; Normand, J.; Raghavachari, K.; Rendell, A. P.; Burant, J. C.; Iyengar, S. S.; Tomasi, J.; Cossi, M.; Millam, J. M.; Klene, M.; Adamo, C.; Cammi, R.; Ochterski, J. W.; Martin, R. L.; Morokuma, K.; Farkas, O.; Foresman, J. B.; Fox, D. J. *Gaussian 16, Revision C.01*; Gaussian, Inc.: Wallingford CT, 2016.

(53) Curtiss, L. A.; Redfern, P. C.; Raghavachari, K. Gaussian-4 Theory. *J. Chem. Phys.* **2007**, *126* (8), 084108. https://doi.org/10.1063/1.2436888.

Supplementary Information

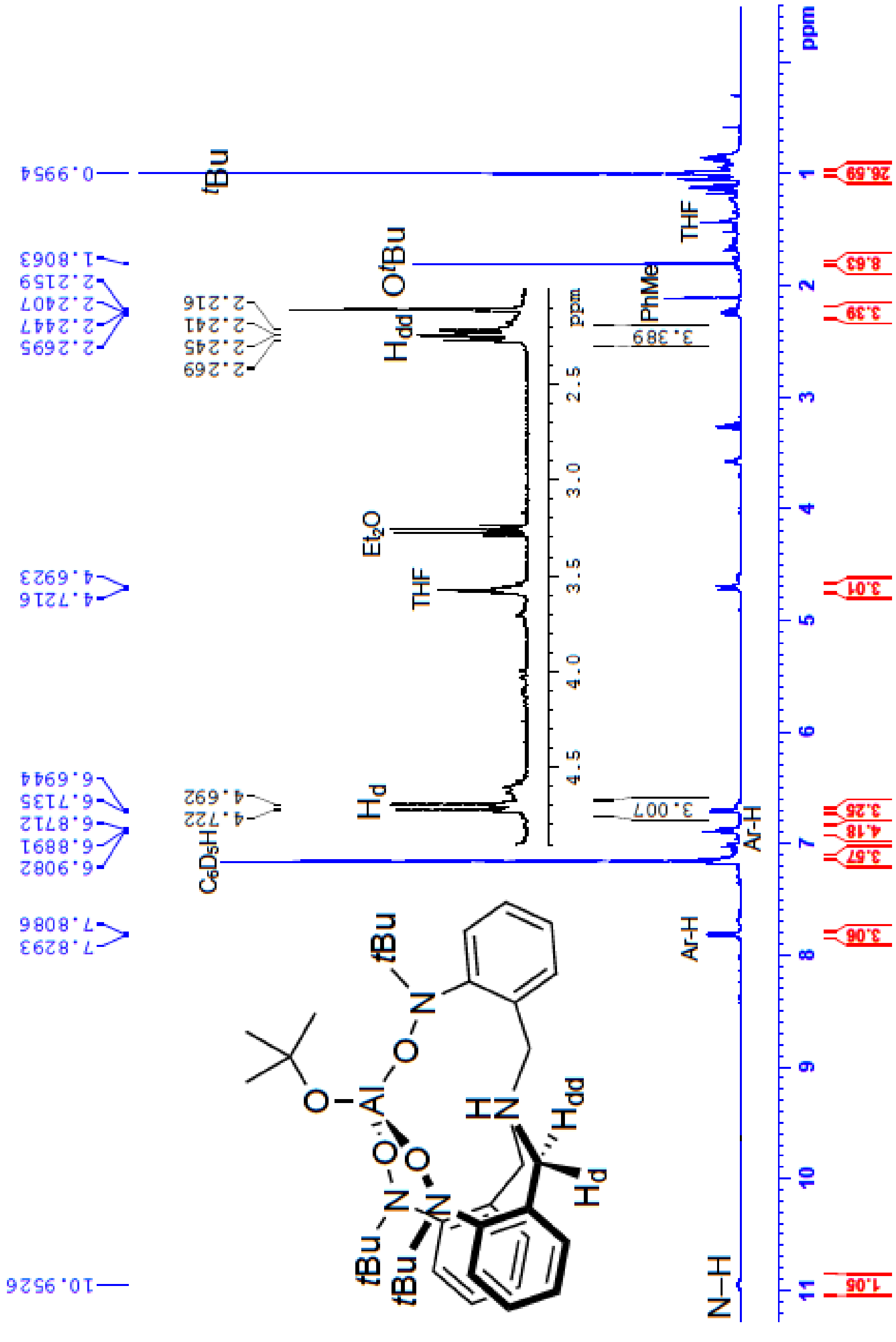

Figure S1. ^{1}H NMR spectrum of H(TriNOx)AlO^{t}Bu (**3**) in C_6D_6 at 25°C.

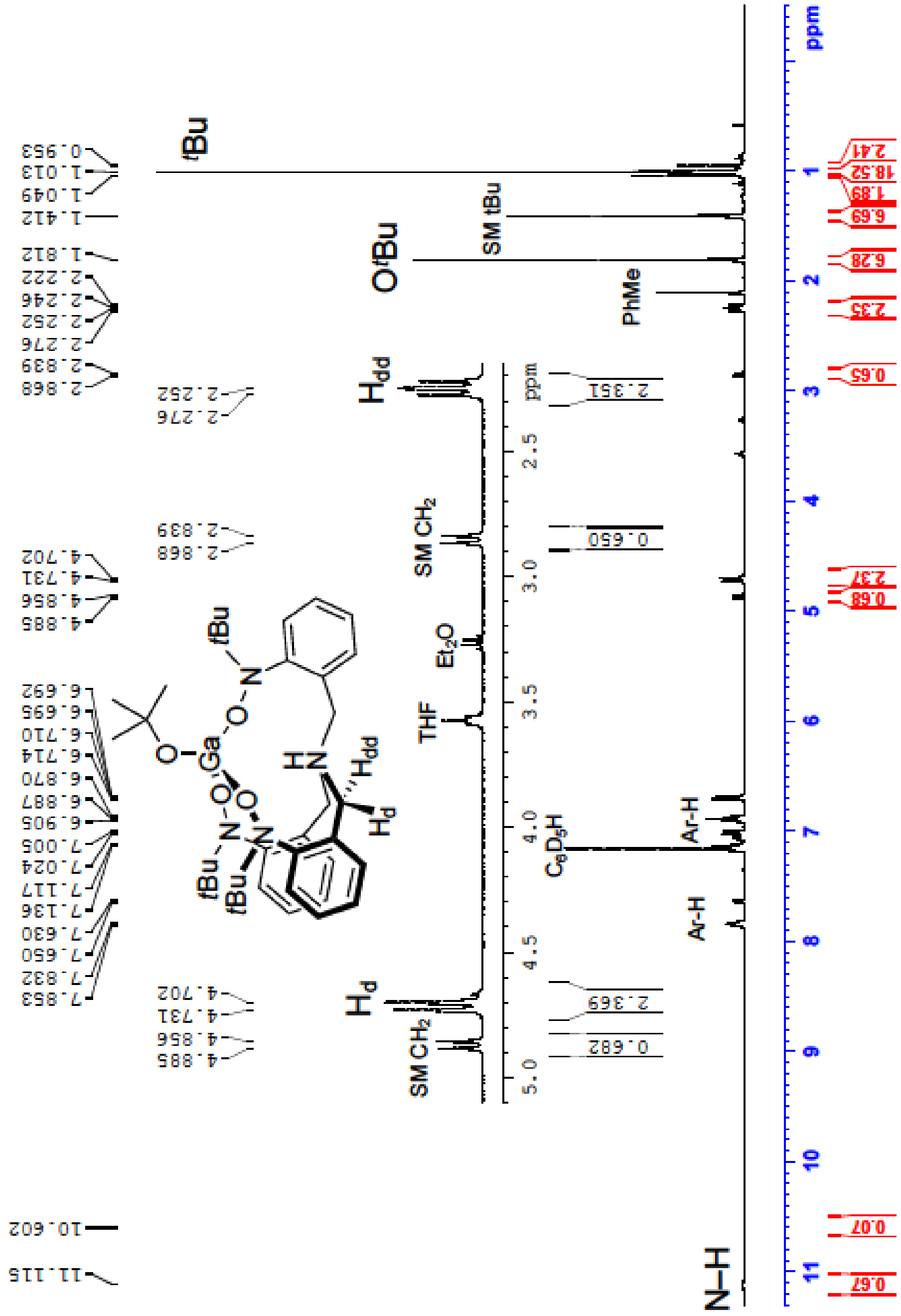

Figure S2. ^{1}H NMR spectrum of solid collected from crystallization attempt of H(TriNOx)GaO^{t}Bu (**4**) from layered reaction of (TriNOx)Ga (**2**) in THF and ^{t}BuOH in hexane at -25°C THF. It represents an approximately 1:4 mixture of **2** and **4**, respectively, in C_6D_6 at 25°C.

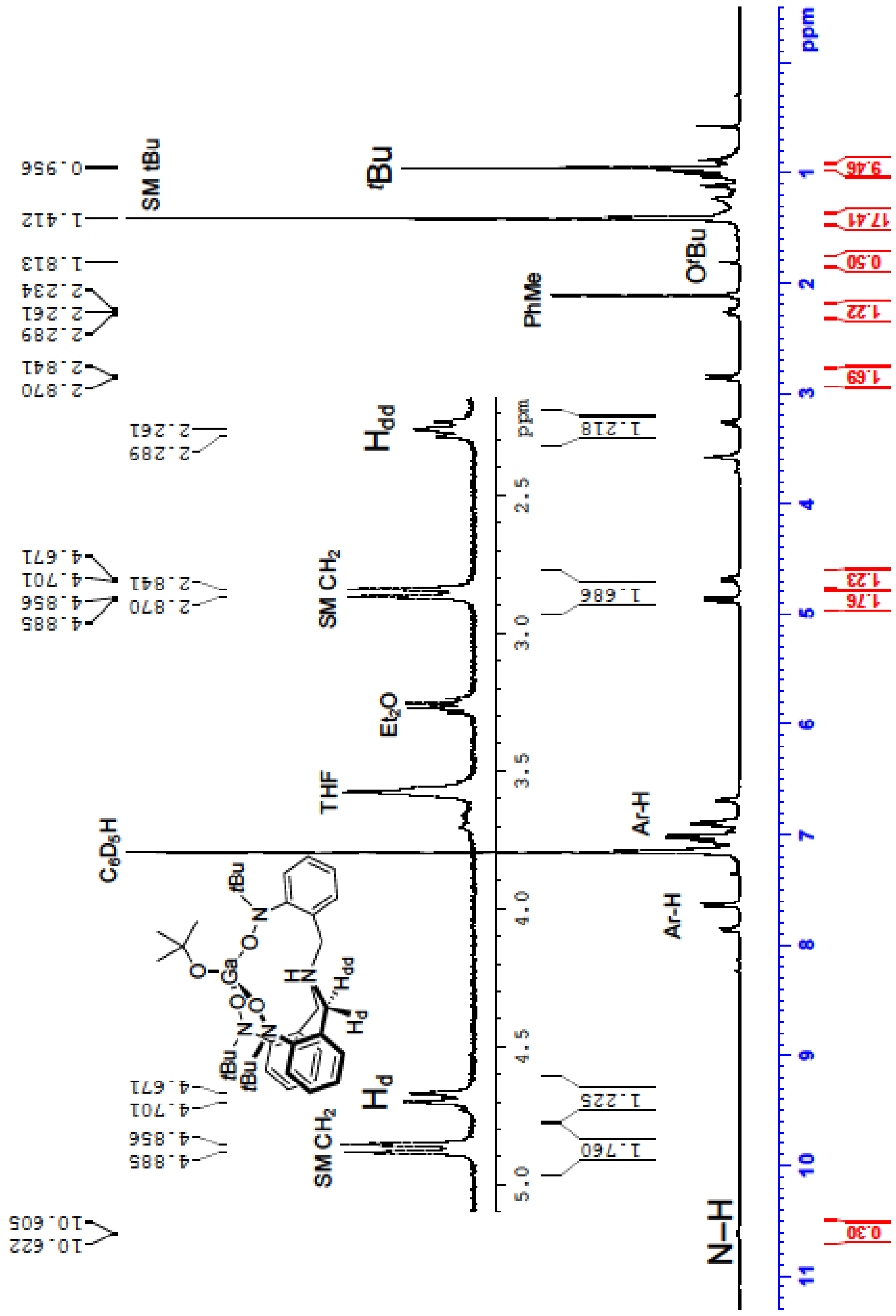

Figure S3. ^{1}H NMR spectrum of solid collected from crystallization attempt of H(TriNOx)GaO^{t}Bu (**4**) from layered reaction of (TriNOx)Ga (**2**) in THF and ^{t}BuOH in hexane at room temperature. It represents a 7:3 mixture of **2** and **4**, respectively, in C$_6$D$_6$ at 25°C.

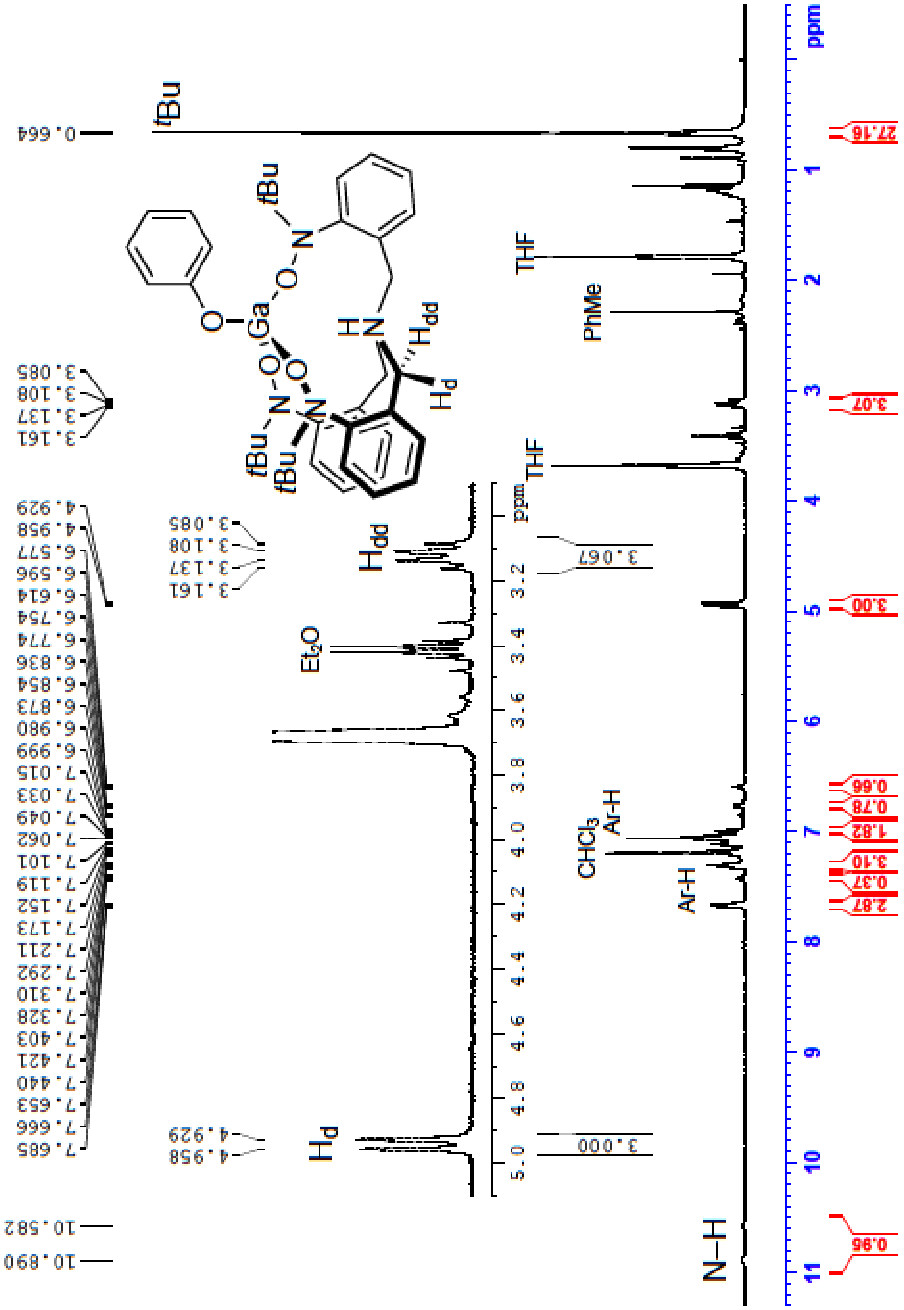

Figure S4. ^{1}H NMR spectrum of H(TriNOx)GaOPh (**6**) in $CDCl_3$ at 25°C.

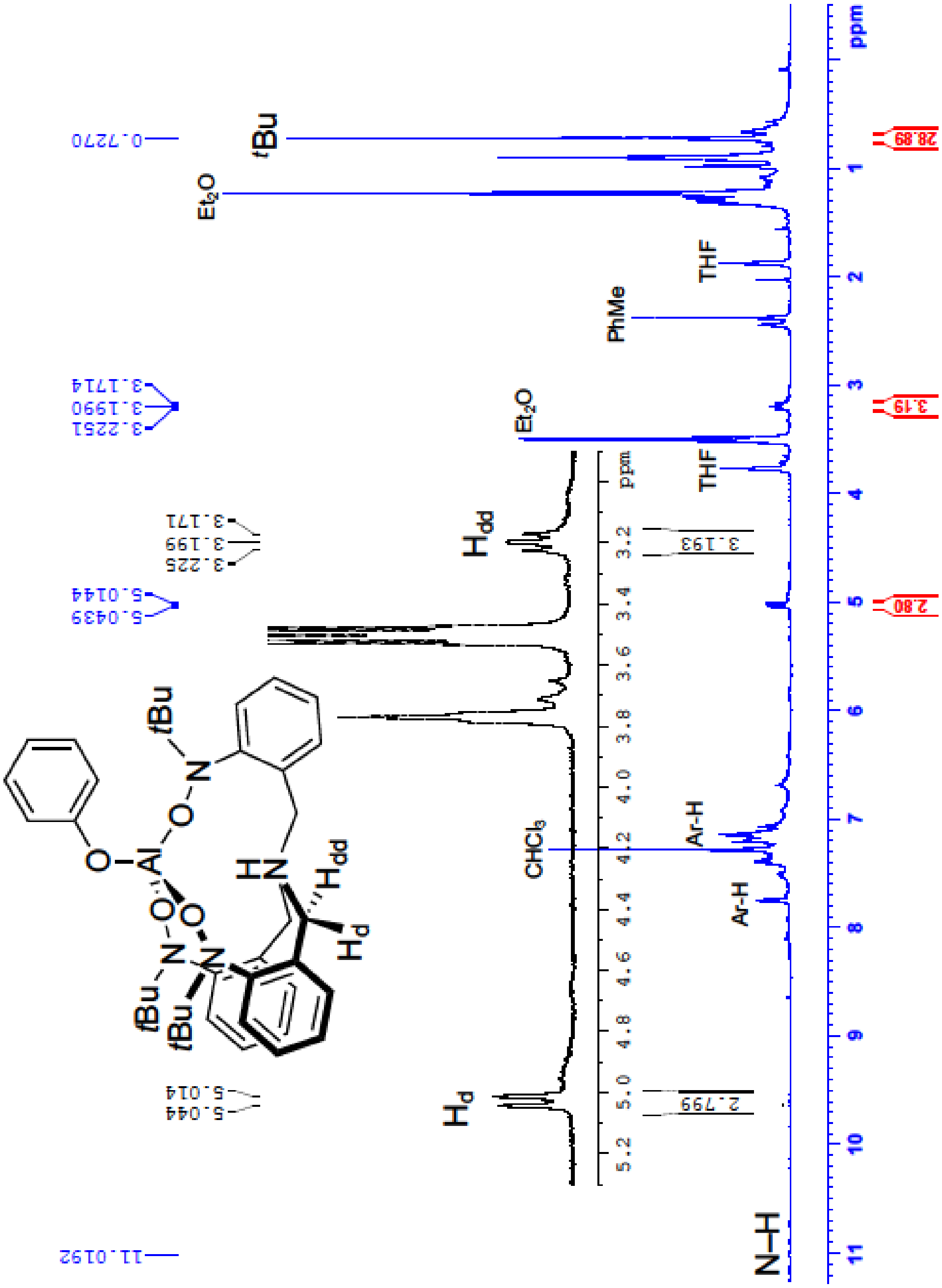

Figure S5. ^{1}H NMR spectrum of H(TriNOx)AlOPh (5) in $CDCl_3$ at 25°C.

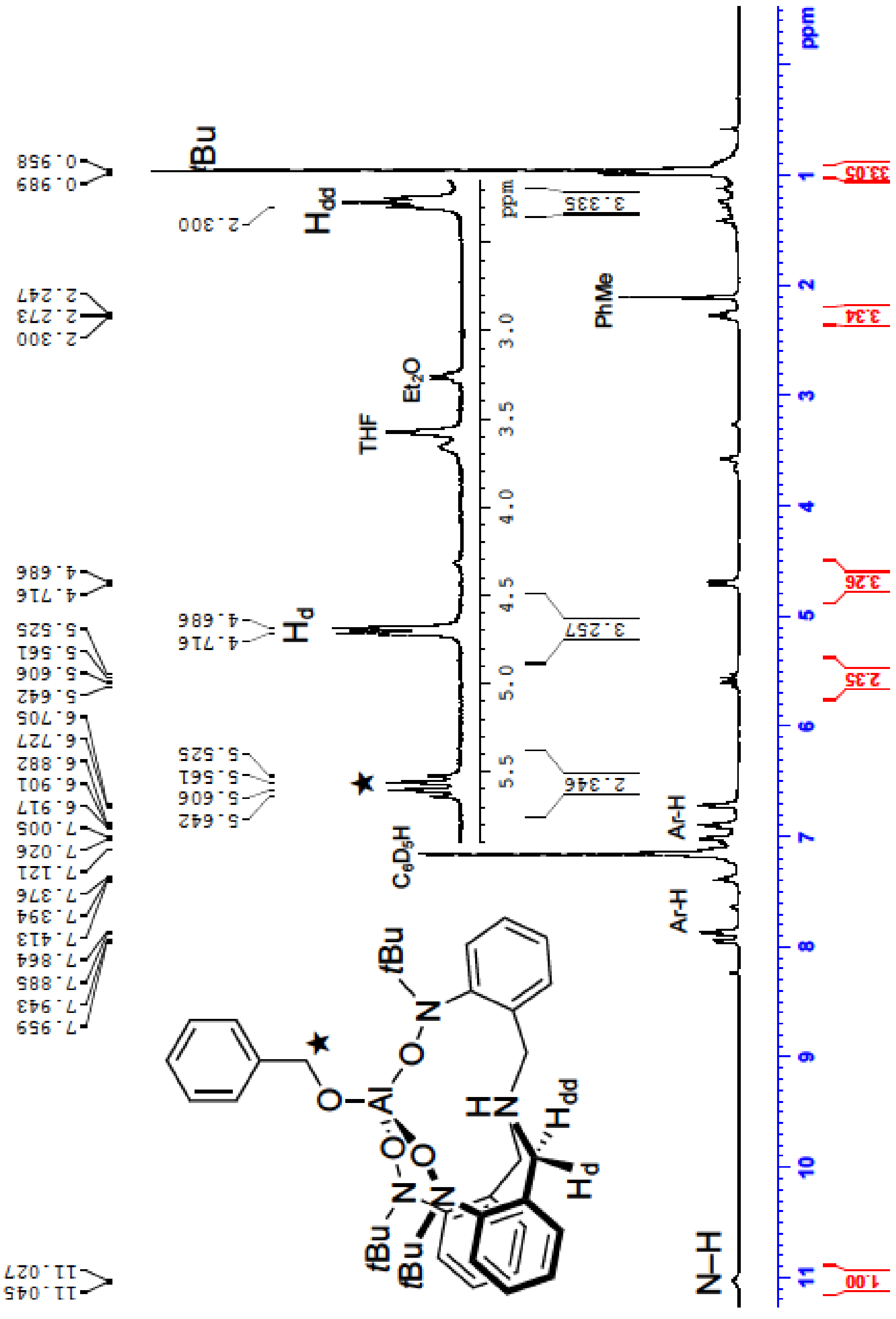

Figure S6. ^{1}H NMR spectrum of H(TriNOx)AlOBn (7) in C_6D_6 at 25°C.

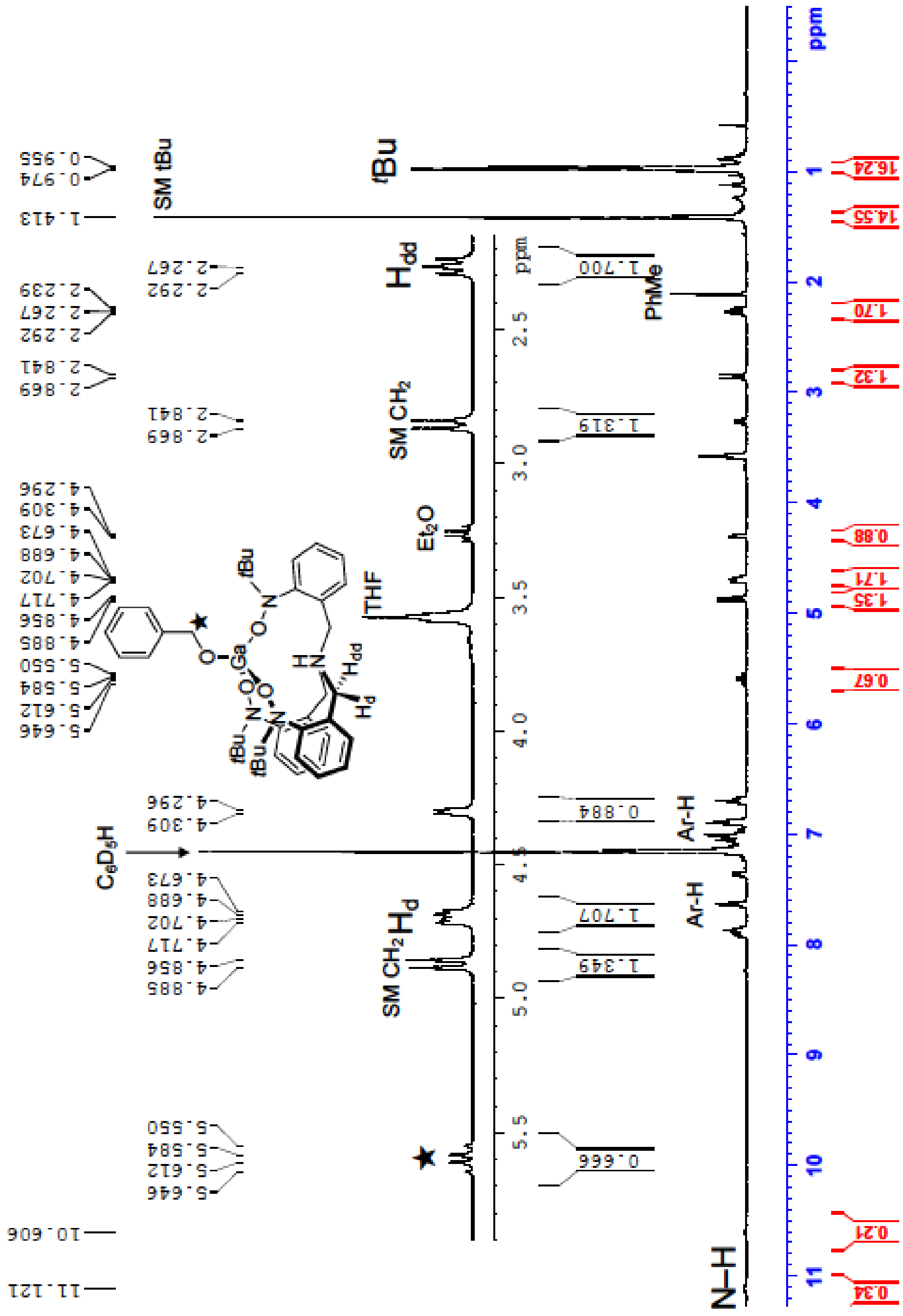

Figure S7. ^{1}H NMR spectrum of (TriNOx)Ga (**2**) and H(TriNOx)GaOBn (**8**) in equilibrium in C_6D_6 at 25°C.

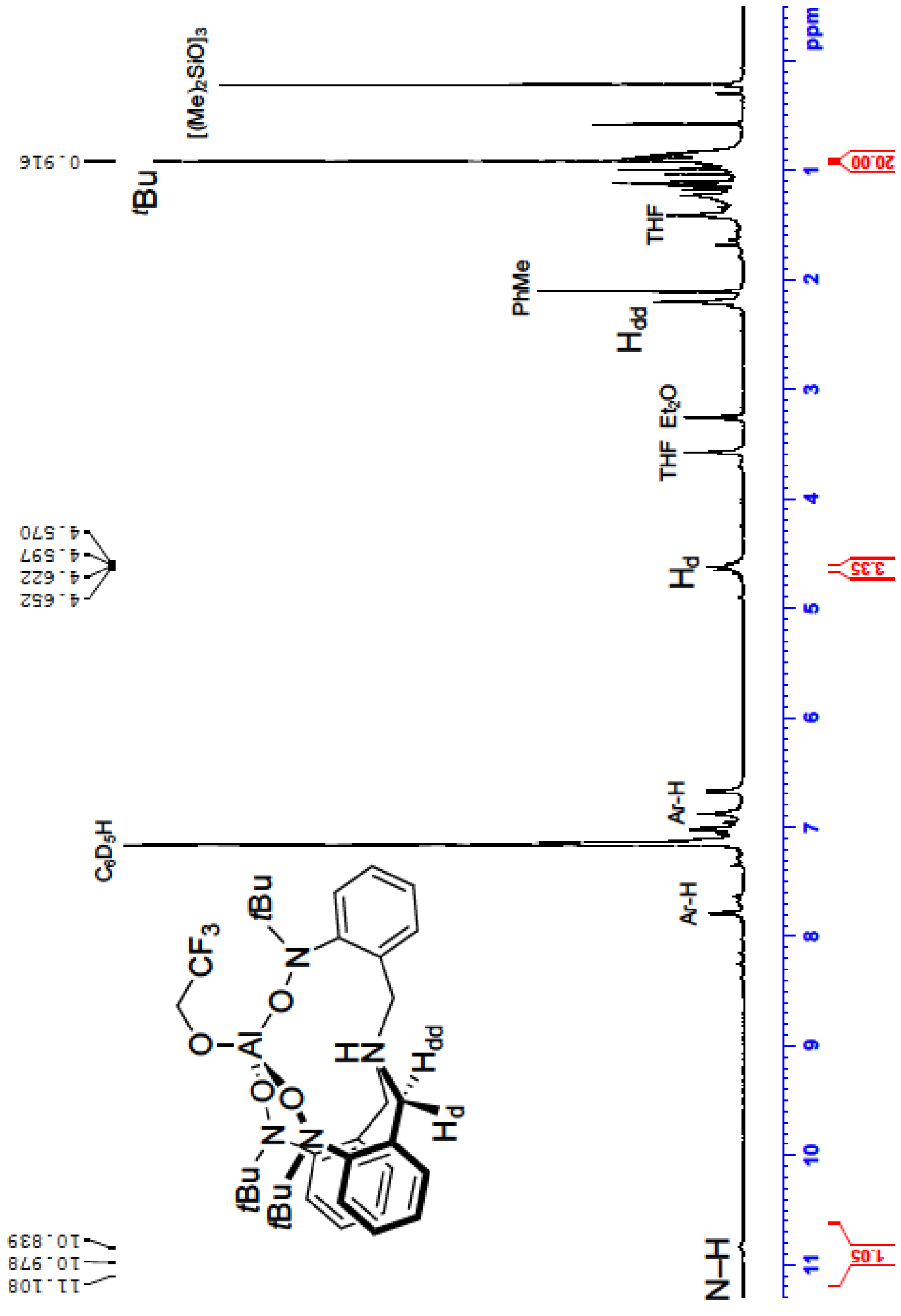

Figure S8. ^{1}H NMR spectrum of H(TriNOx)AlOCH$_2$CF$_3$ in CDCl$_3$ at 20°C.

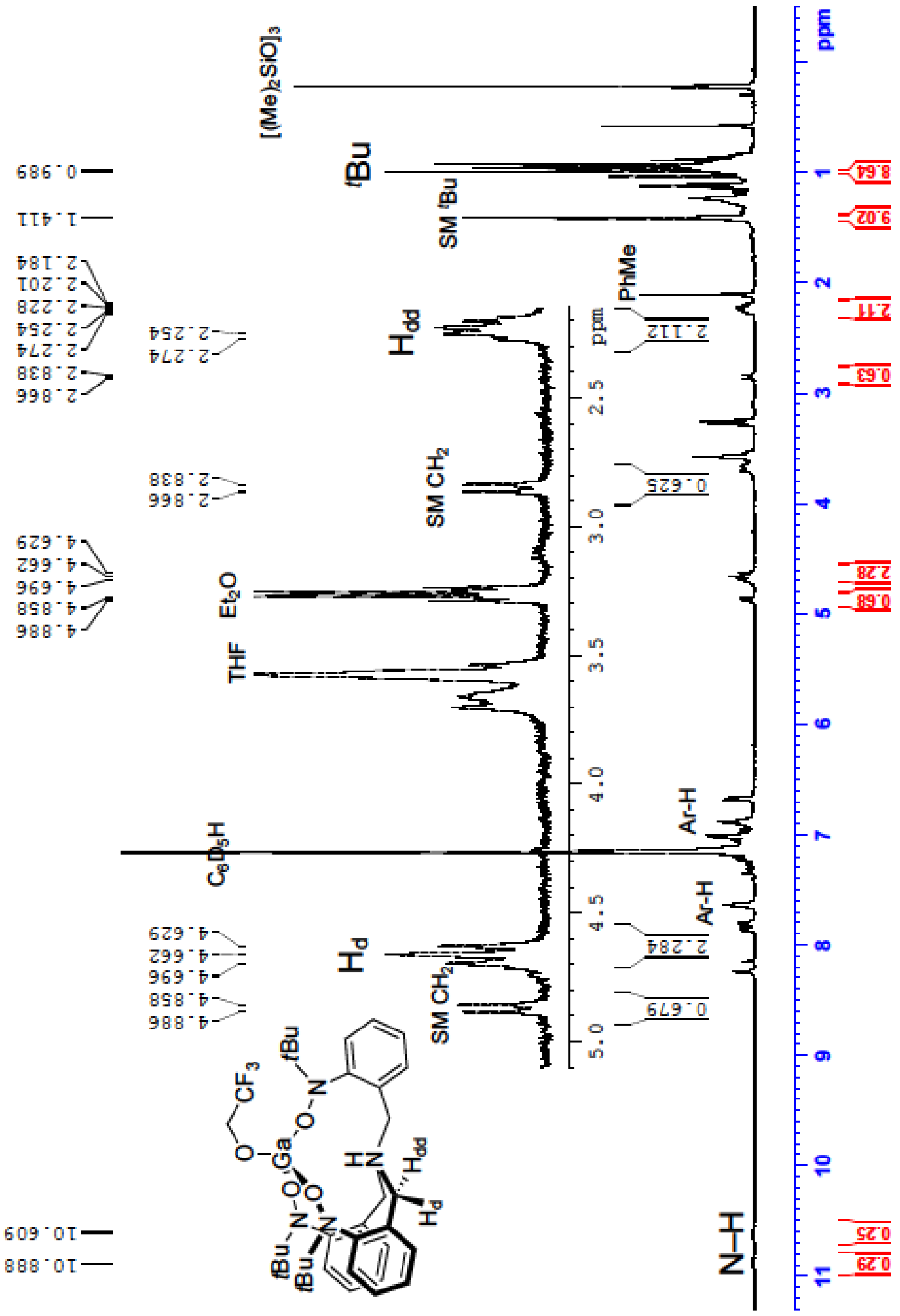

Figure S9. ^{1}H NMR spectrum of (TriNOx)Ga (**2**) and H(TriNOx)GaOCH$_2$CF$_3$ in equilibrium in C_6D_6 at 20°C.

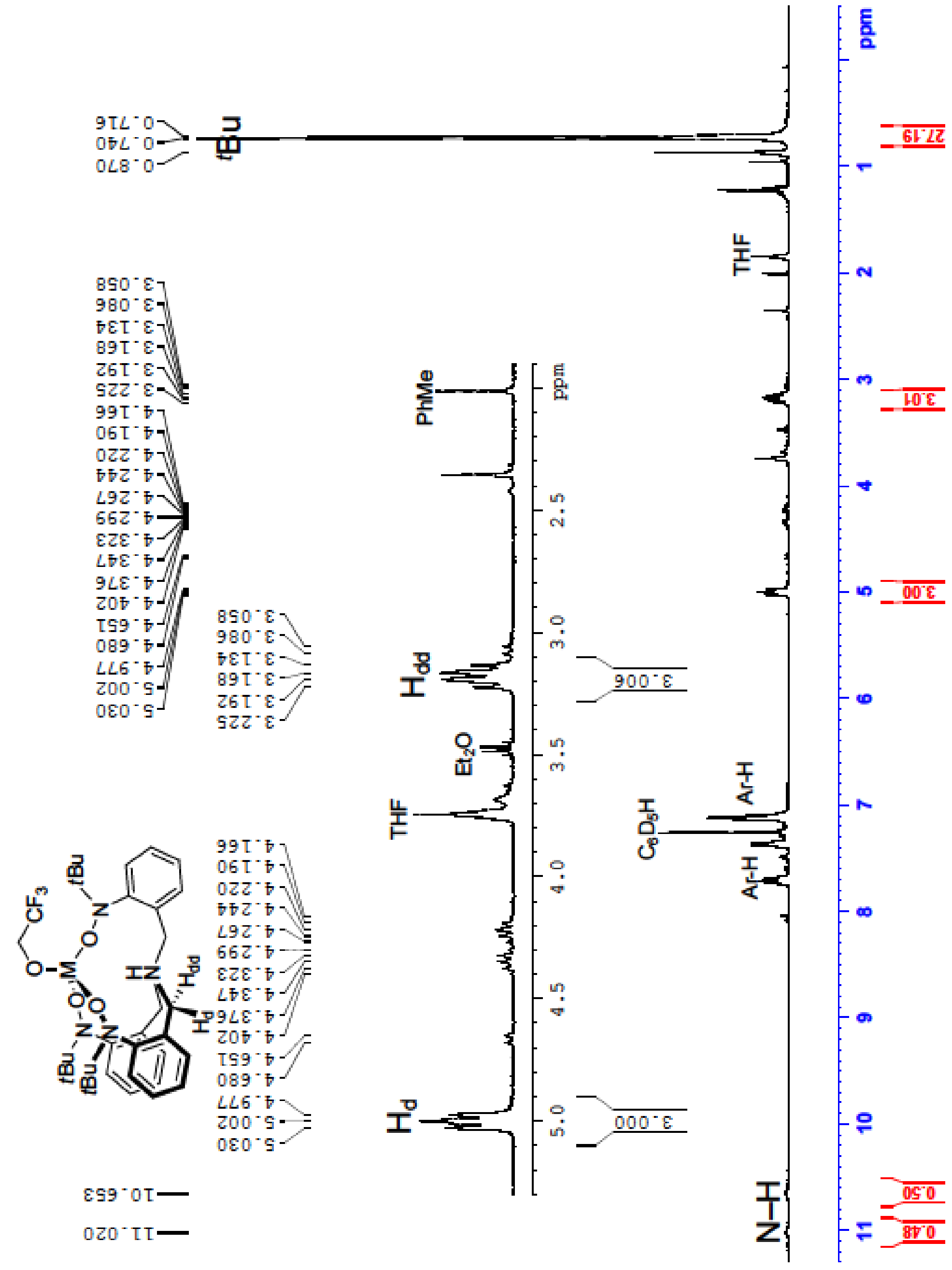

Figure S10. ^{1}H NMR spectrum of H(TriNOx)MOCH$_2$CF$_3$ in CDCl$_3$ at 25°C.

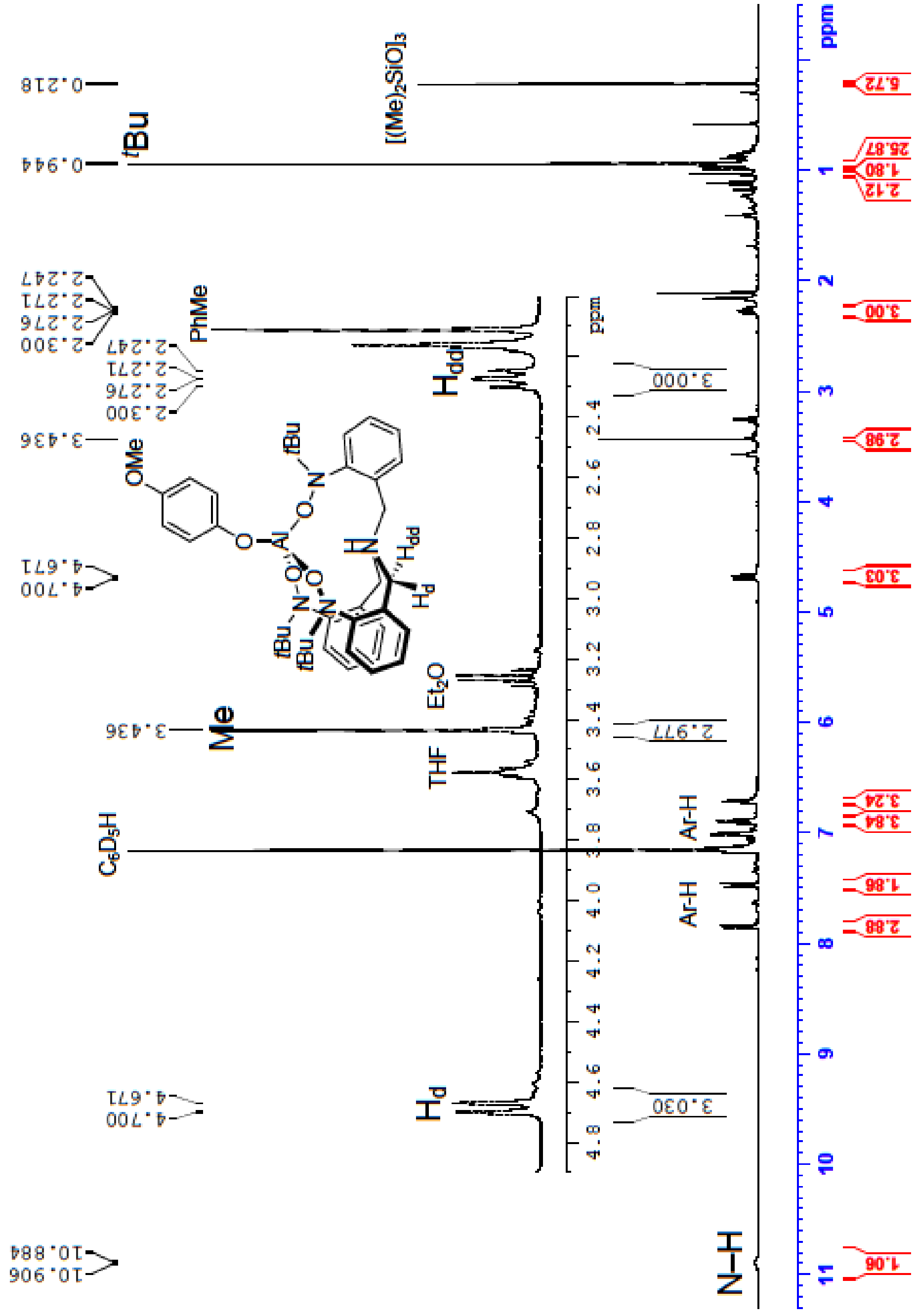

Figure S11. ^{1}H NMR spectrum of 4-MeO-PhOAl(TriNOx)H in C_6D_6 at 20°C.

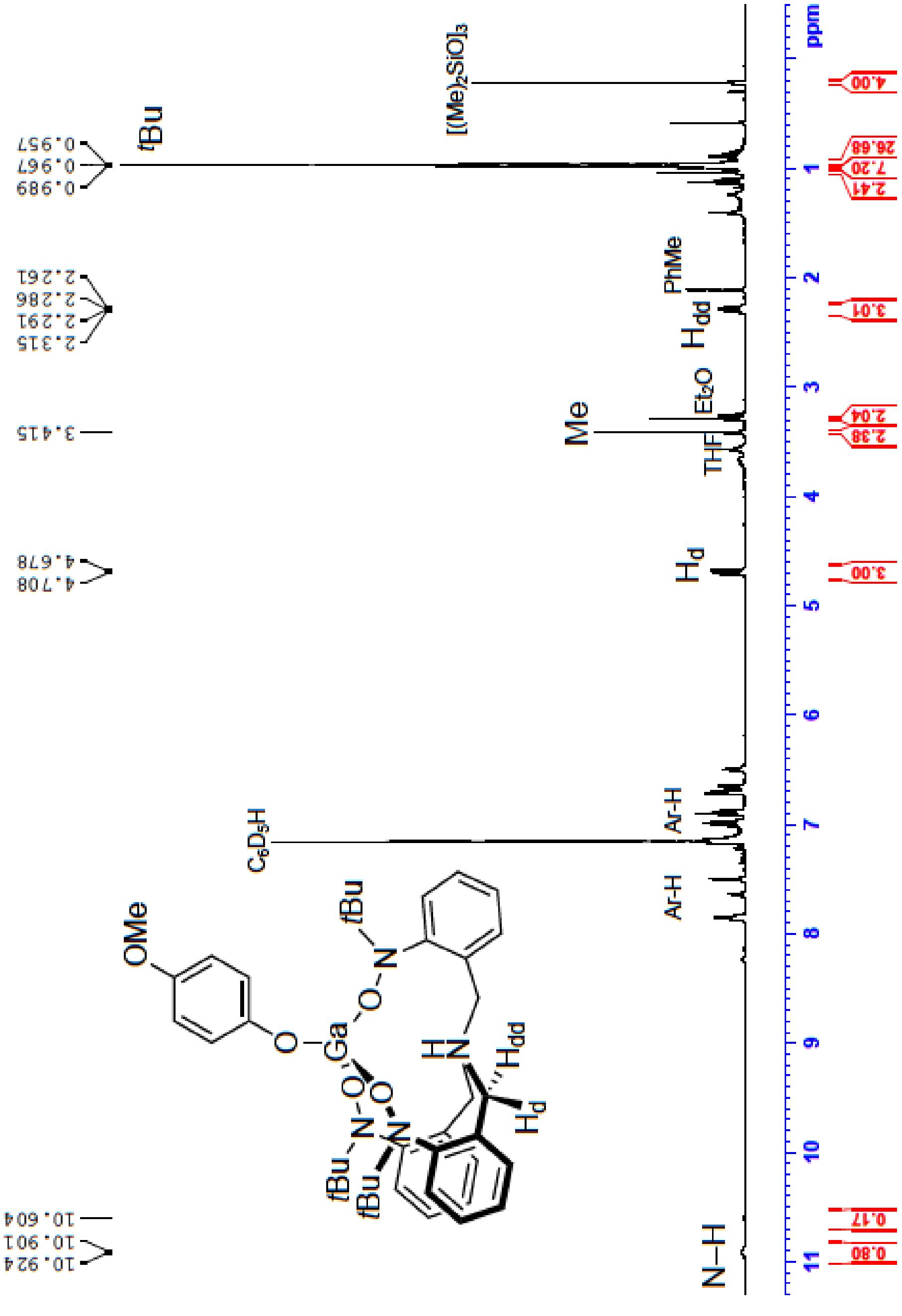

Figure S12. ^{1}H NMR spectrum of 4-MeO-PhOGa(TriNOx)H in C_6D_6 at 20°C.

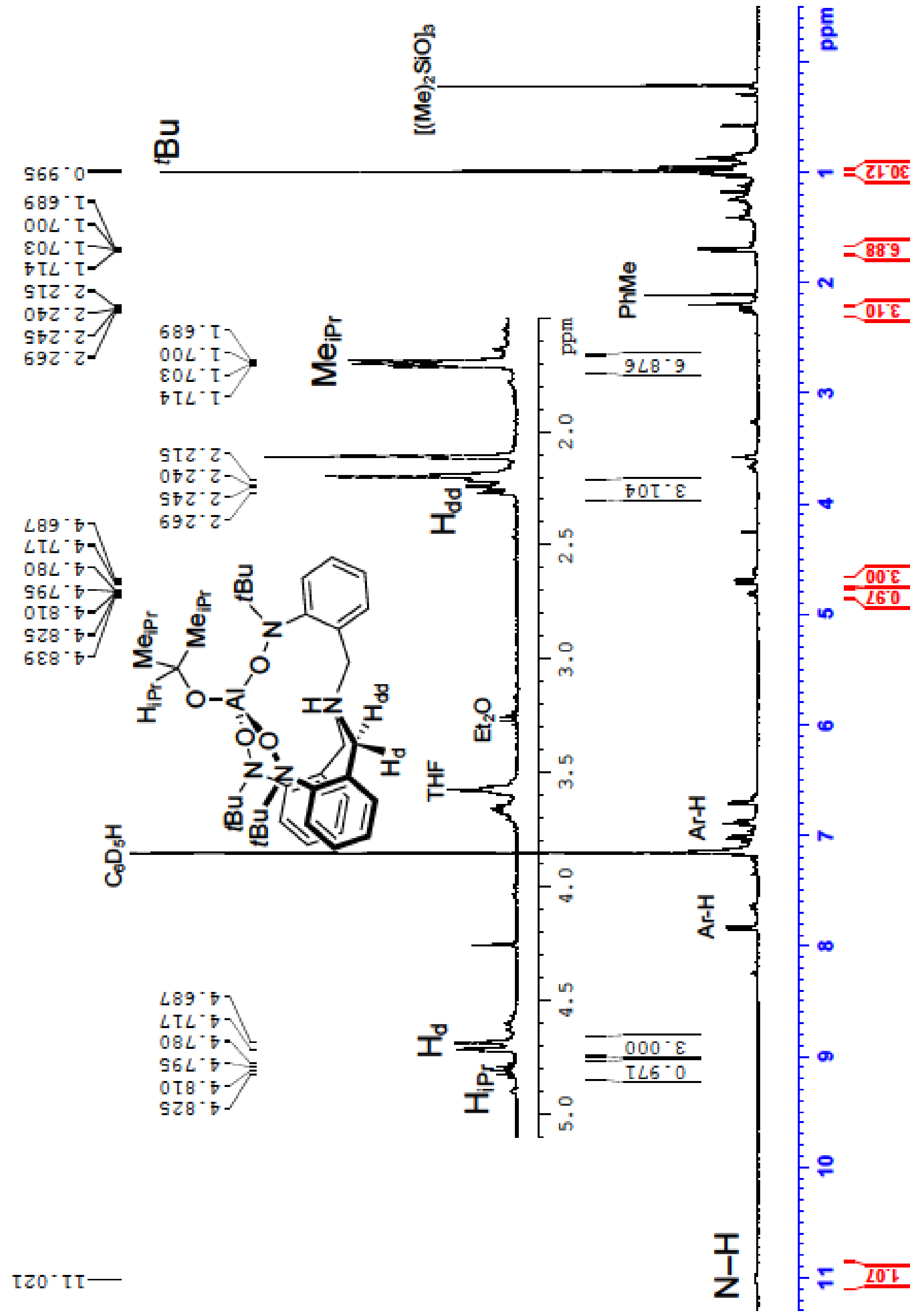

Figure S13. ^{1}H NMR spectrum of H(TriNOx)AlO^{i}Pr in C_6D_6 at 20°C.

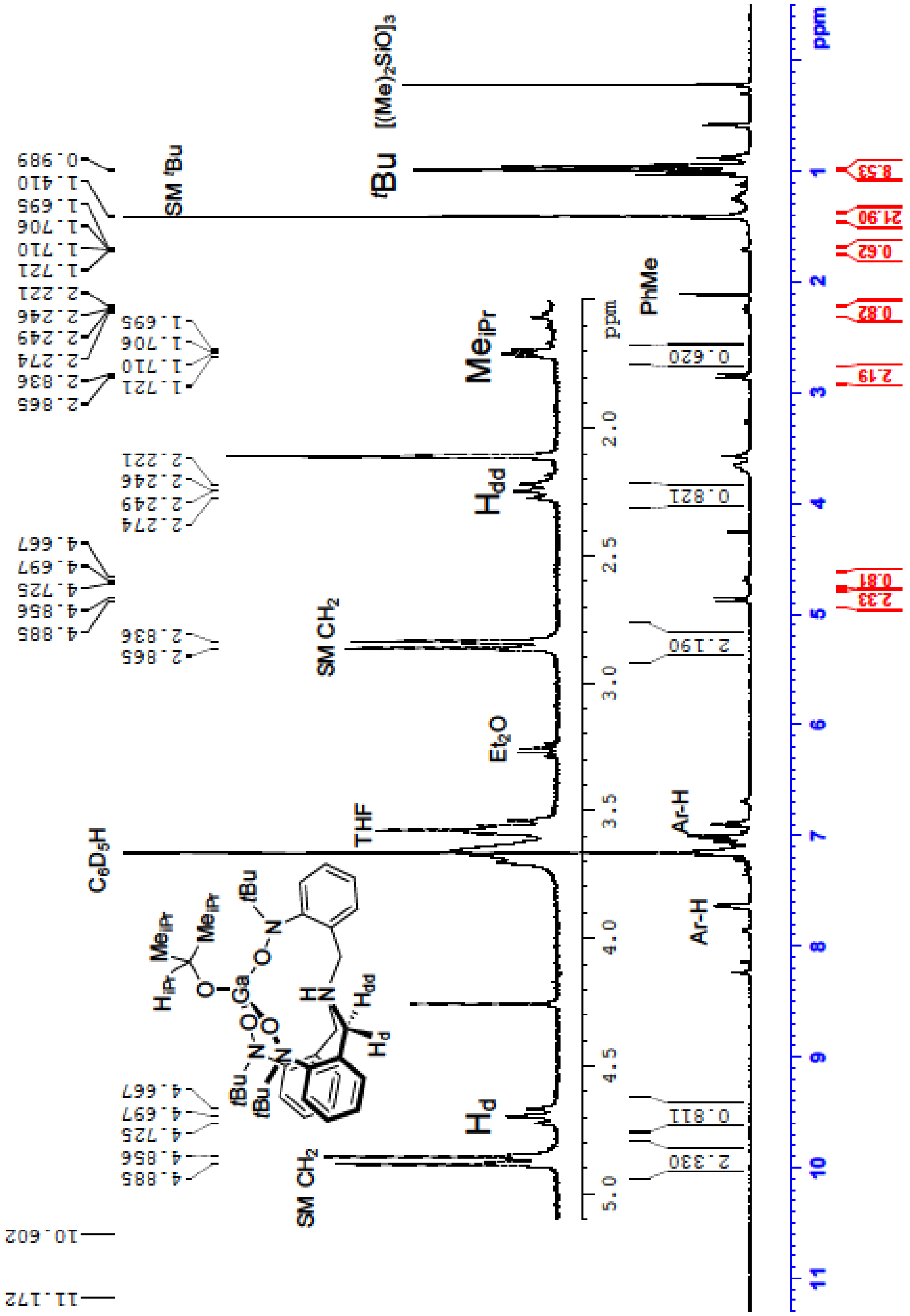

Figure S14. ^{1}H NMR spectrum of (TriNOx)Ga (**2**) and H(TriNOx)GaO^{i}Pr in equilibrium in C$_6$D$_6$ at 20°C.

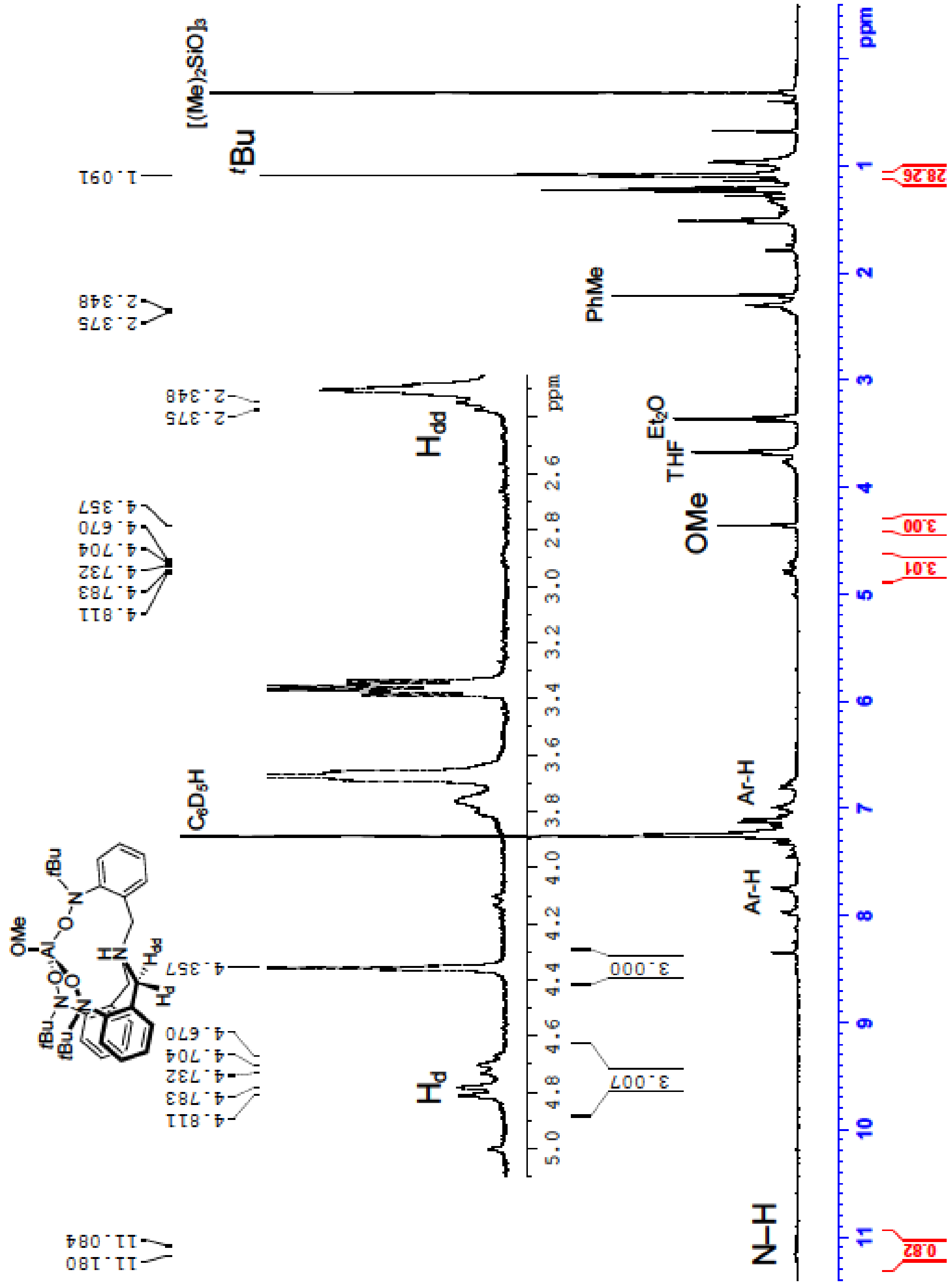

Figure S15. ^{1}H NMR spectrum of H(TriNOx)AlOMe in C_6D_6 at 20°C.

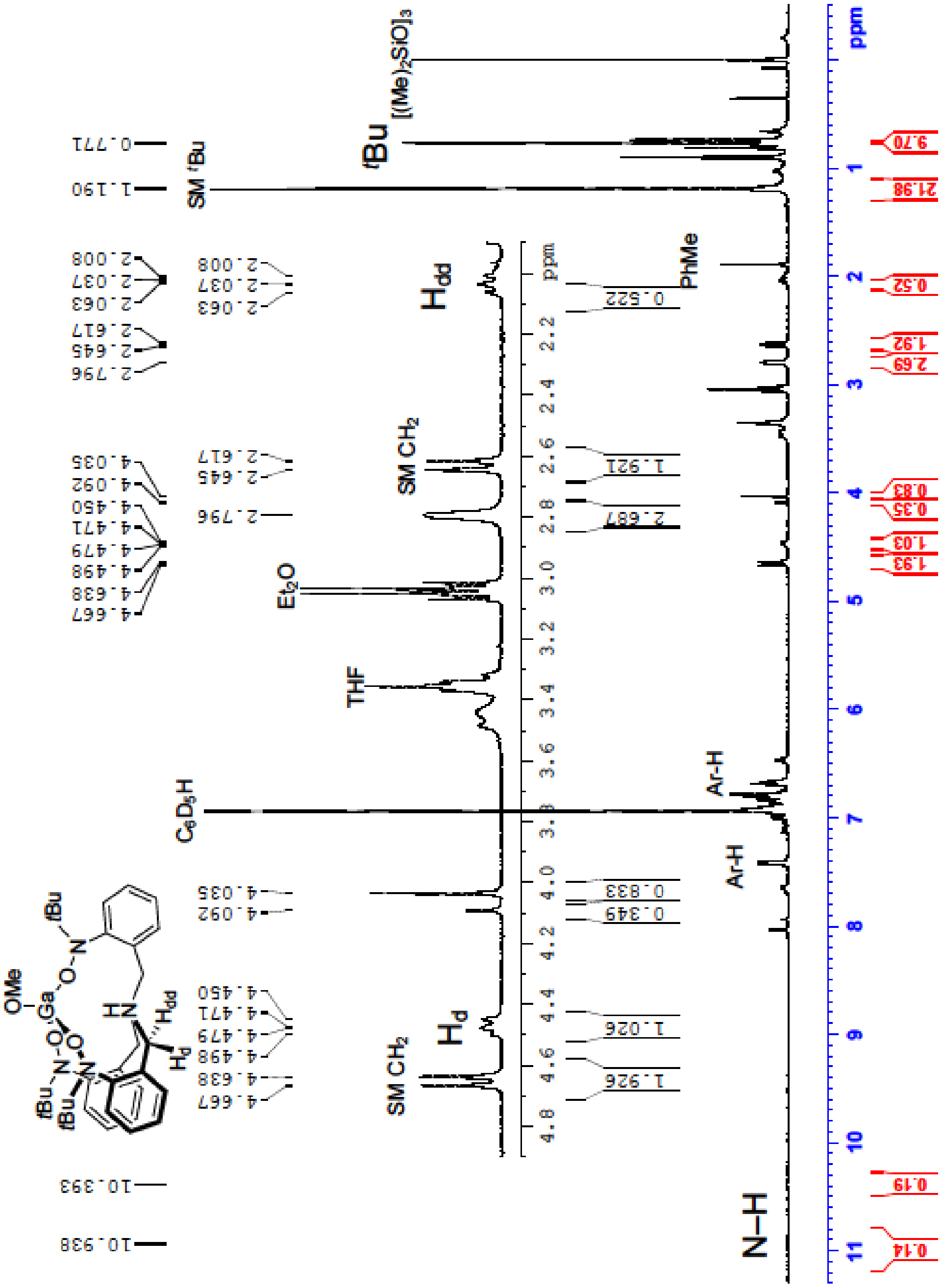

Figure S16. ^{1}H NMR spectrum of (TriNOx)Ga (**2**) and H(TriNOx)GaOMe in equilibrium in C_6D_6 at 20°C.

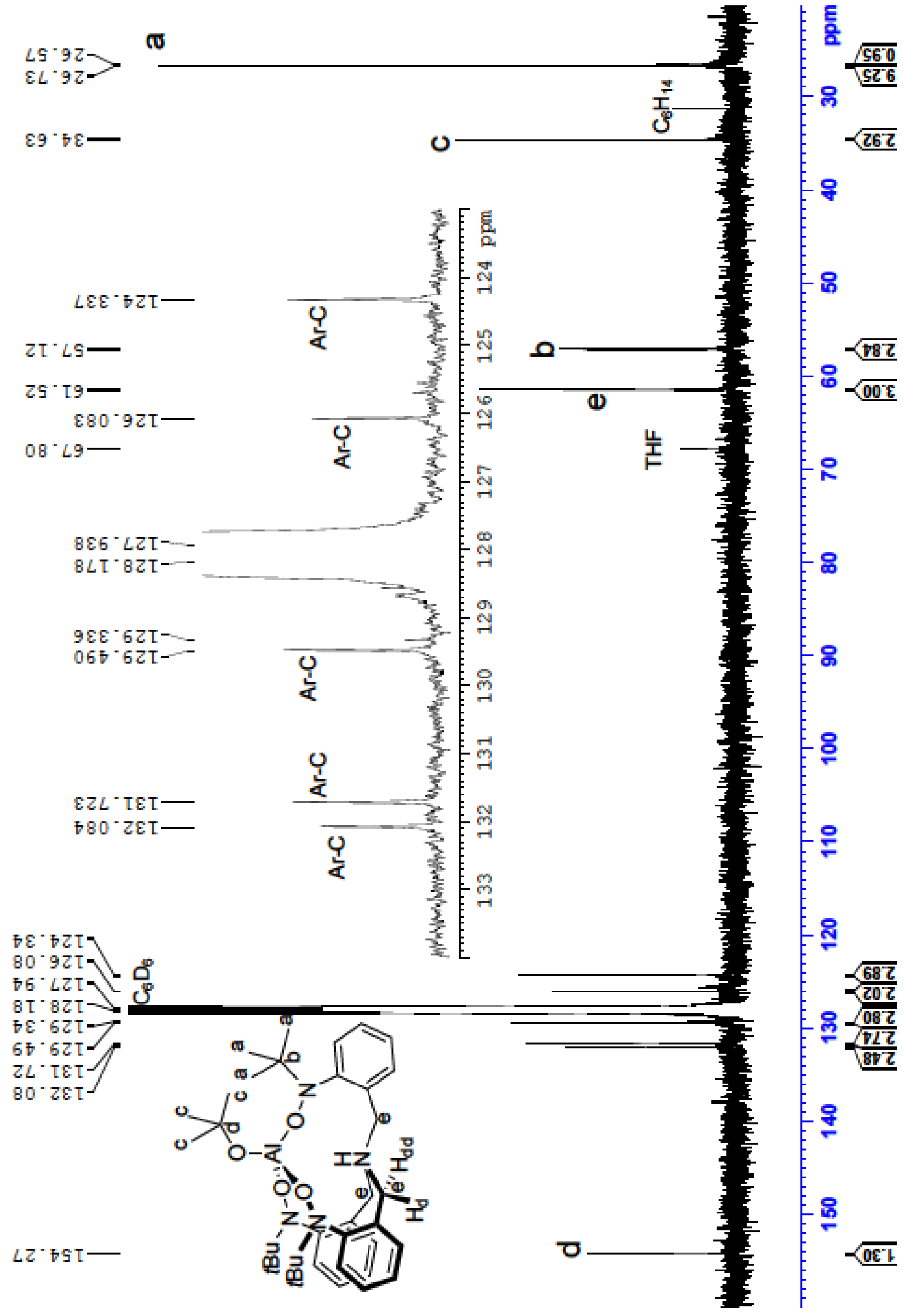

Figure S17. ^{13}C NMR spectrum of H(TriNOx)AlO^{t}Bu (**3**) in C_6D_6 at 20°C.

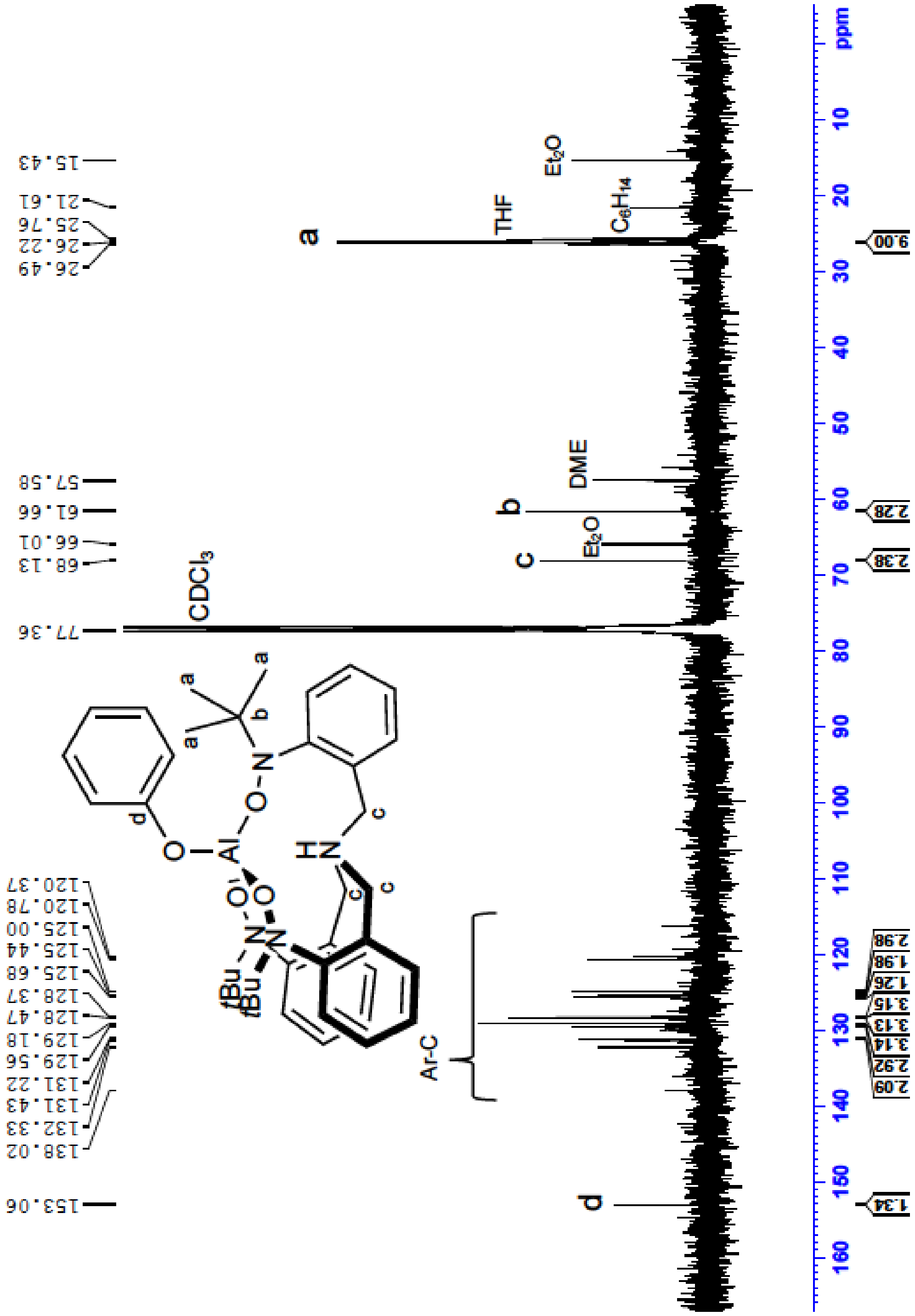

Figure S18. ^{13}C NMR spectrum of H(TriNOx)AlOPh (5) in $CDCl_3$ at 20°C.

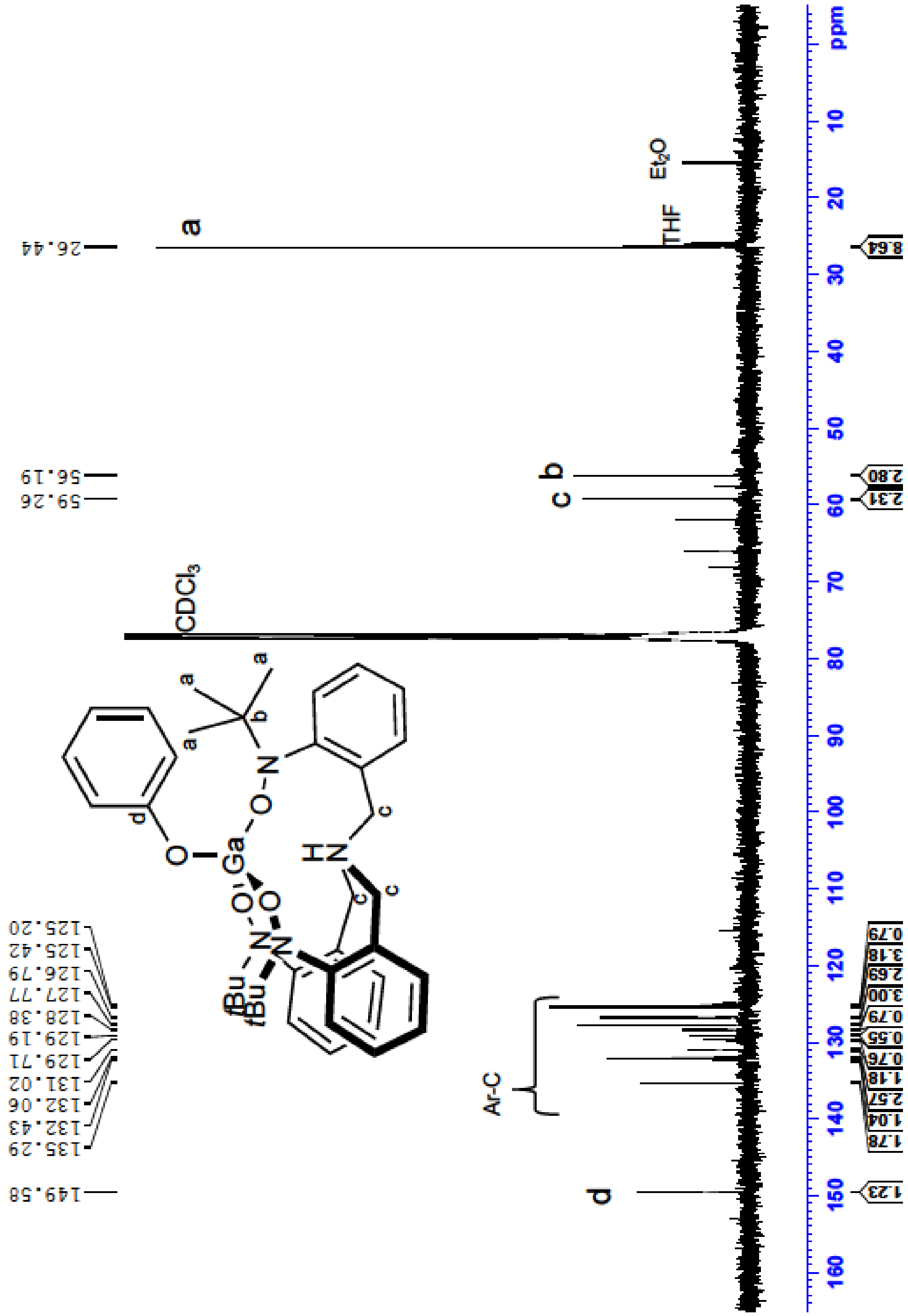

Figure S18. ^{13}C NMR spectrum of H(TriNOx)GaOPh (**6**) in $CDCl_3$ at 20°C.

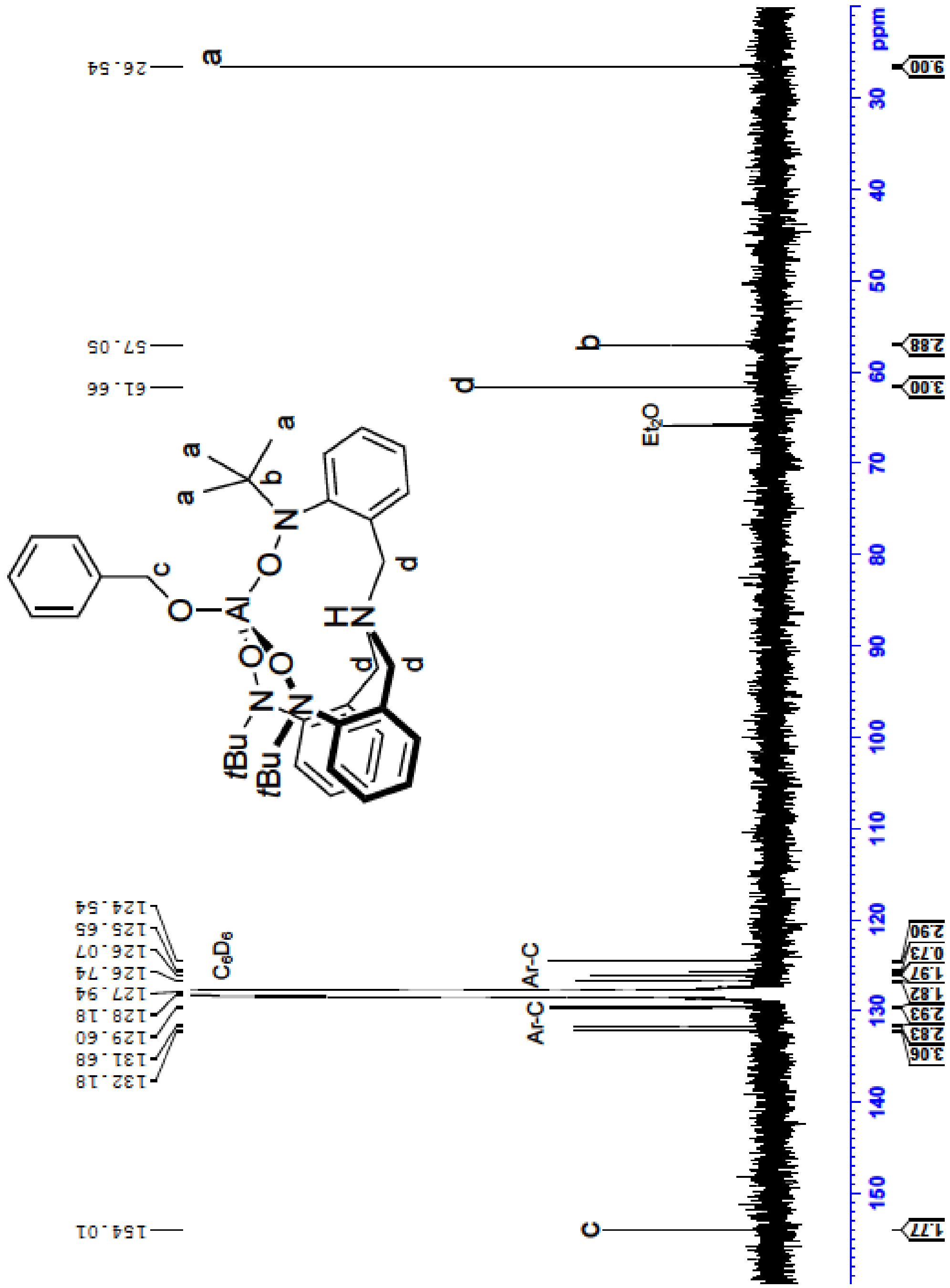

Figure S20. ^{13}C NMR spectrum of H(TriNOx)AlOBn (7) in C_6D_6 at 20°C.

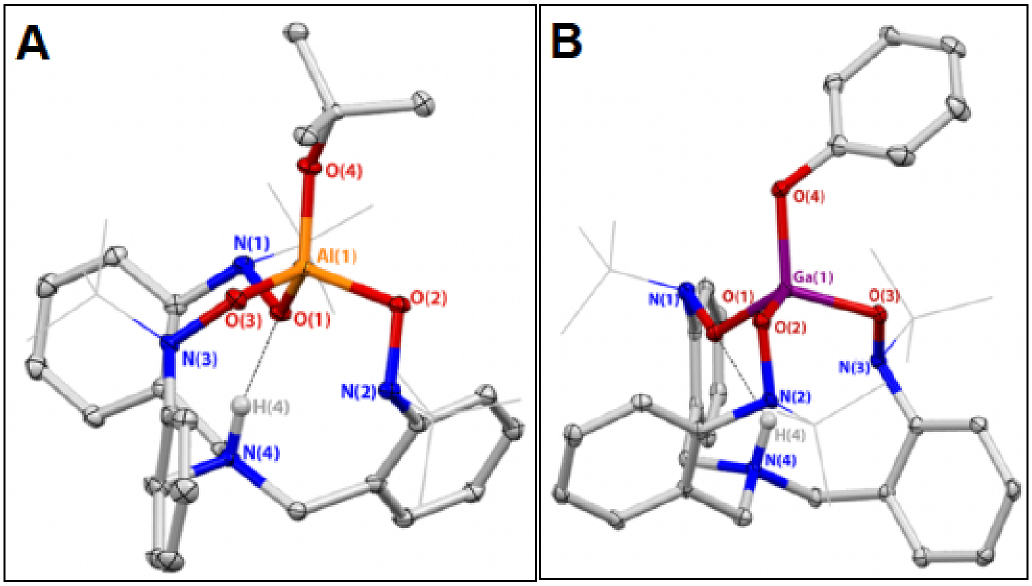

Figure S21. **A**. Solid state single crystal structure of H(TriNOx)AlO^{t}Bu (**3**). Ellipsoids are projected at 30% probability. Non-interacting hydrogen atoms have been omitted for clarity. R_1= 0.0427; τ_4[Al(1)]=0.95. **B**. Solid state single crystal structure of H(TriNOx)GaOPh (**6**). Ellipsoids are projected at 30% probability. Non-interacting hydrogen atoms have been omitted for clarity. R_1= 0.0694; τ_4[Ga(1)]=0.93. Structures reproduced from Maenaga & Graves.[45]

Further details for the refinement of H(TriNOx)AlOPh (5): Refinement converged to R1=0.0515 and wR2=0.1393 for 7477 observed reflections for which F > 4σ(F) and R1=0.0612 and wR2=0.1453 and GOF =1.037 for all 8809 unique, non-zero reflections and 442 variables.

Table S1. Summary of Structure Determination of H(TriNOx)AlOPh (**5**).

Empirical formula	$C_{39}H_{51}AlN_4O_4$
Formula weight	666.81
Diffractometer	Rigaku XtaLAB Synergy-S (Dectris Pilatus3 R 200K)
Temperature/K	100
Crystal system	monoclinic
Space group	$P2_1/c$
a	16.9374(5)Å
b	12.0802(3)Å
c	18.6133(6)Å
β	111.252(4)°
Volume	3549.4(2)Å^3
Z	4
d_{calc}	1.248 g/cm^3
μ	0.103 mm^{-1}
F(000)	1432.0
Crystal size, mm	0.2 × 0.12 × 0.08
2θ range for data collection	4.696 - 56.564°
Index ranges	$-22 \leq h \leq 22$, $-16 \leq k \leq 16$, $-24 \leq l \leq 24$
Reflections collected	75288
Independent reflections	8809[R(int) = 0.0432]
Data/restraints/parameters	8809/0/442
Goodness-of-fit on F^2	1.037
Final R indexes [I>=2σ (I)]	$R_1 = 0.0515$, $wR_2 = 0.1393$
Final R indexes [all data]	$R_1 = 0.0612$, $wR_2 = 0.1453$
Largest diff. peak/hole	0.63/-0.33 eÅ^{-3}

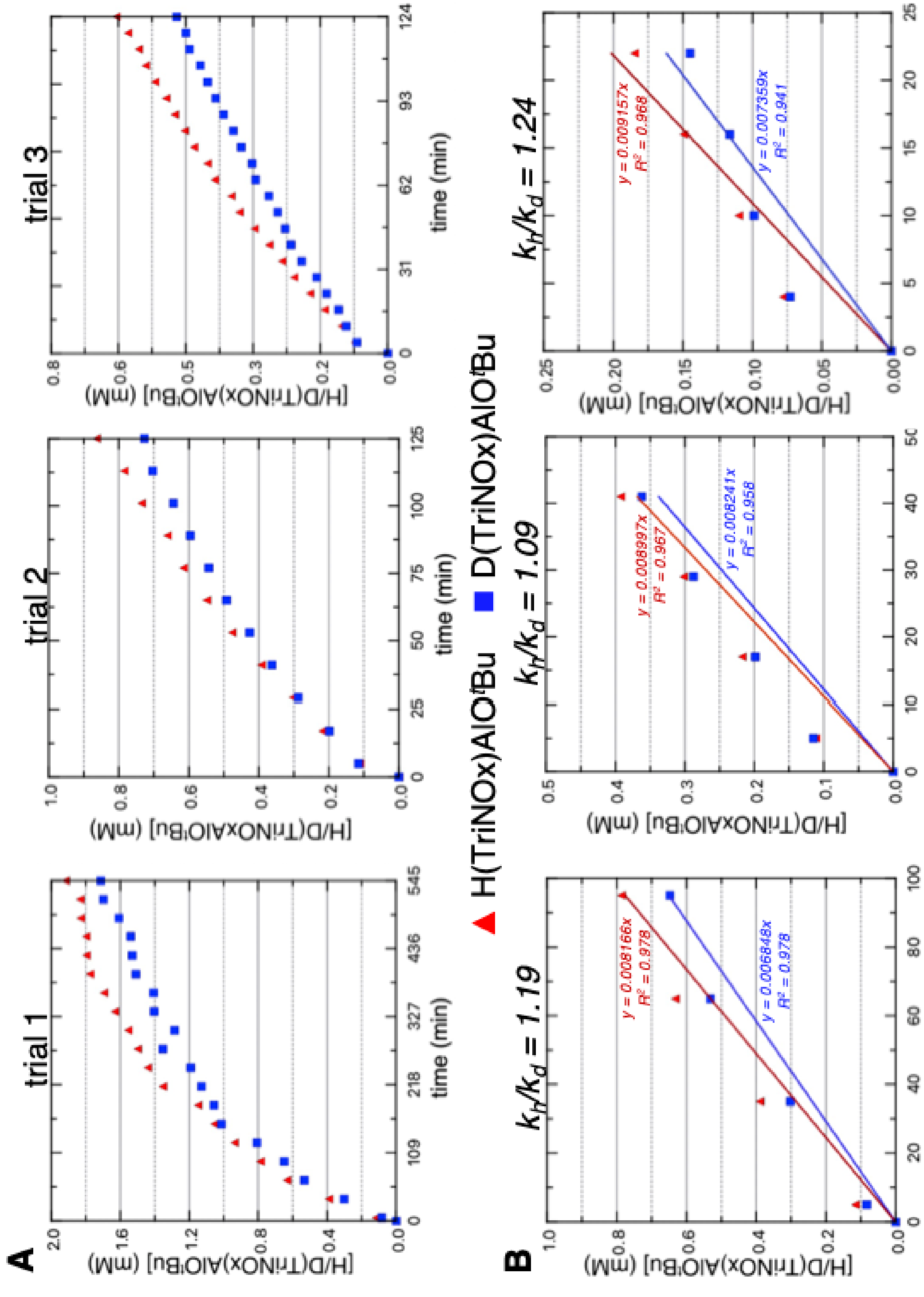

Figure S22. **A**. Complete kinetic profiles of $n = 3$ trials of complex **1** reacting with ^{t}BuOH and ^{t}BuOD. **B**. Linearly approximated initial rates and associated KIE values for each of the profiles shown in **A**., displayed with linear fit slopes. The slope of the OH reaction divided by the slope of the OD reaction results in the k_h/k_d value for that trial.

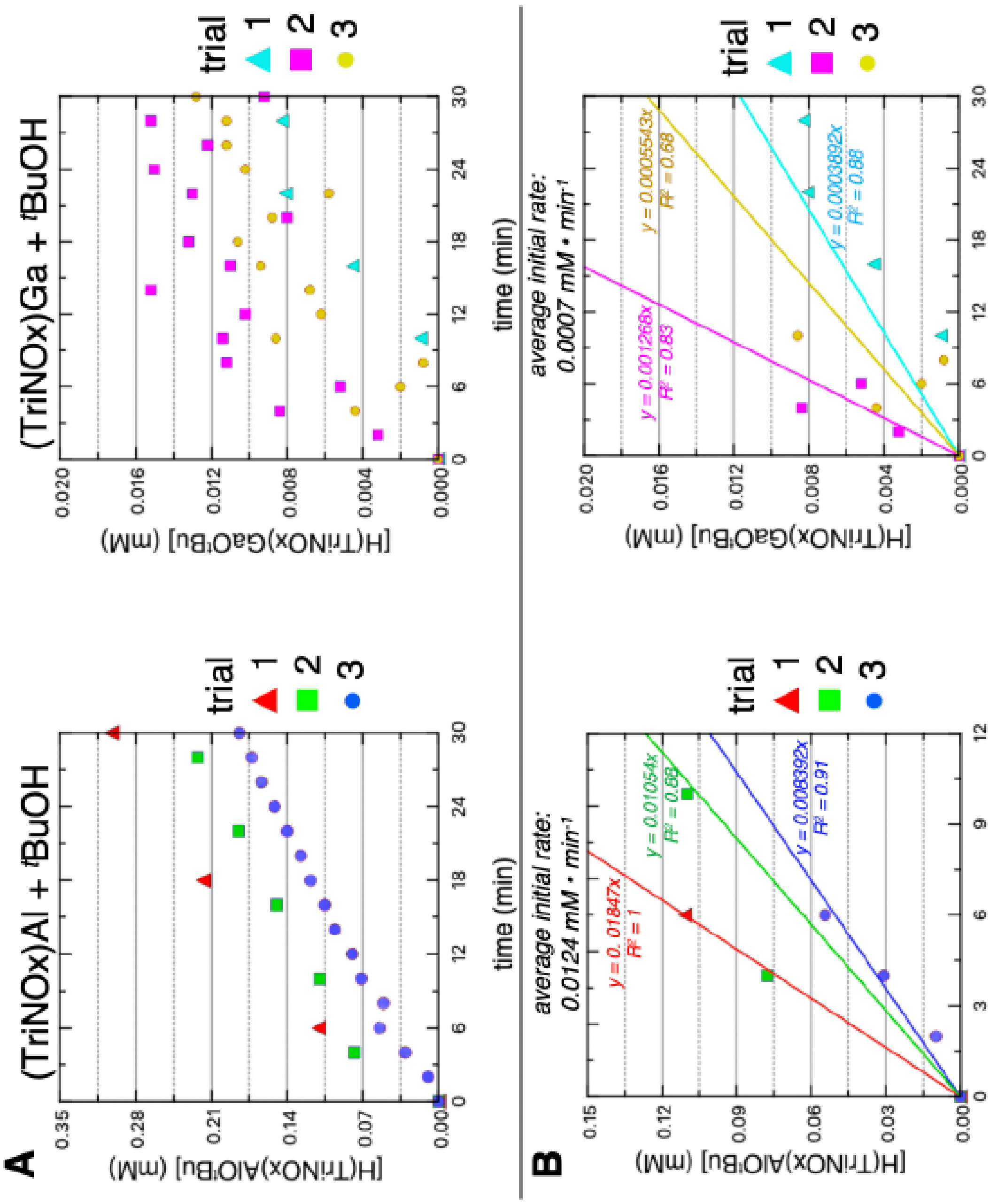

Figure S23. **A**. Reaction profiles of all three trials of the reactions of complexes **1** and **2** with *tert*-butanol, each loaded with initial concentrations of 6 mM. **B**. The linearly approximated initial rates of each trial of the stated reactions, with the average initial rate calculated above each plot.

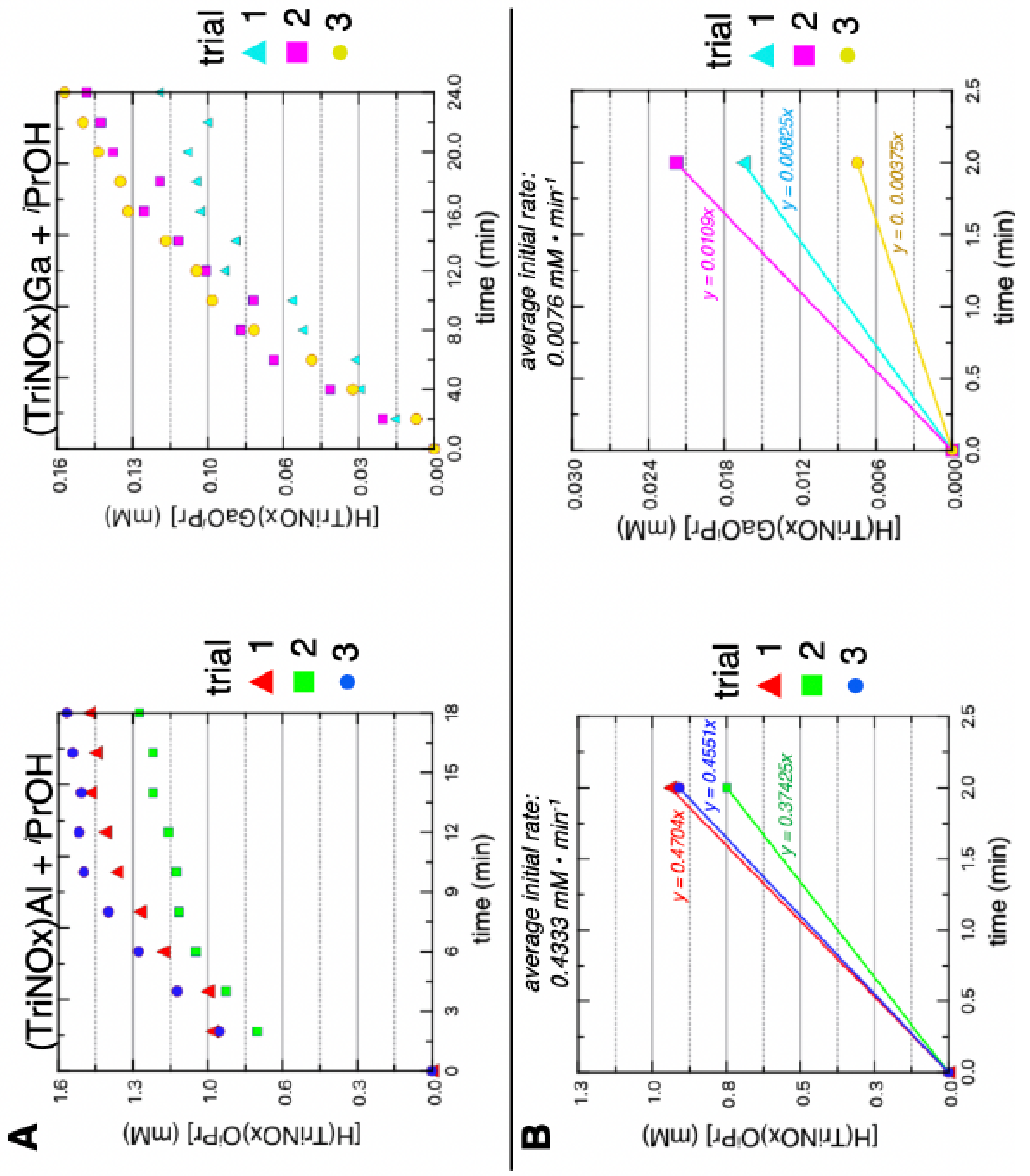

Figure S24. A. Reaction profiles of all three trials of the reactions of complexes **1** and **2** with isopropanol, each loaded with initial concentrations of 6 mM. **B**. The linearly approximated initial rates of each trial of the stated reactions, with the average initial rate calculated above each plot.

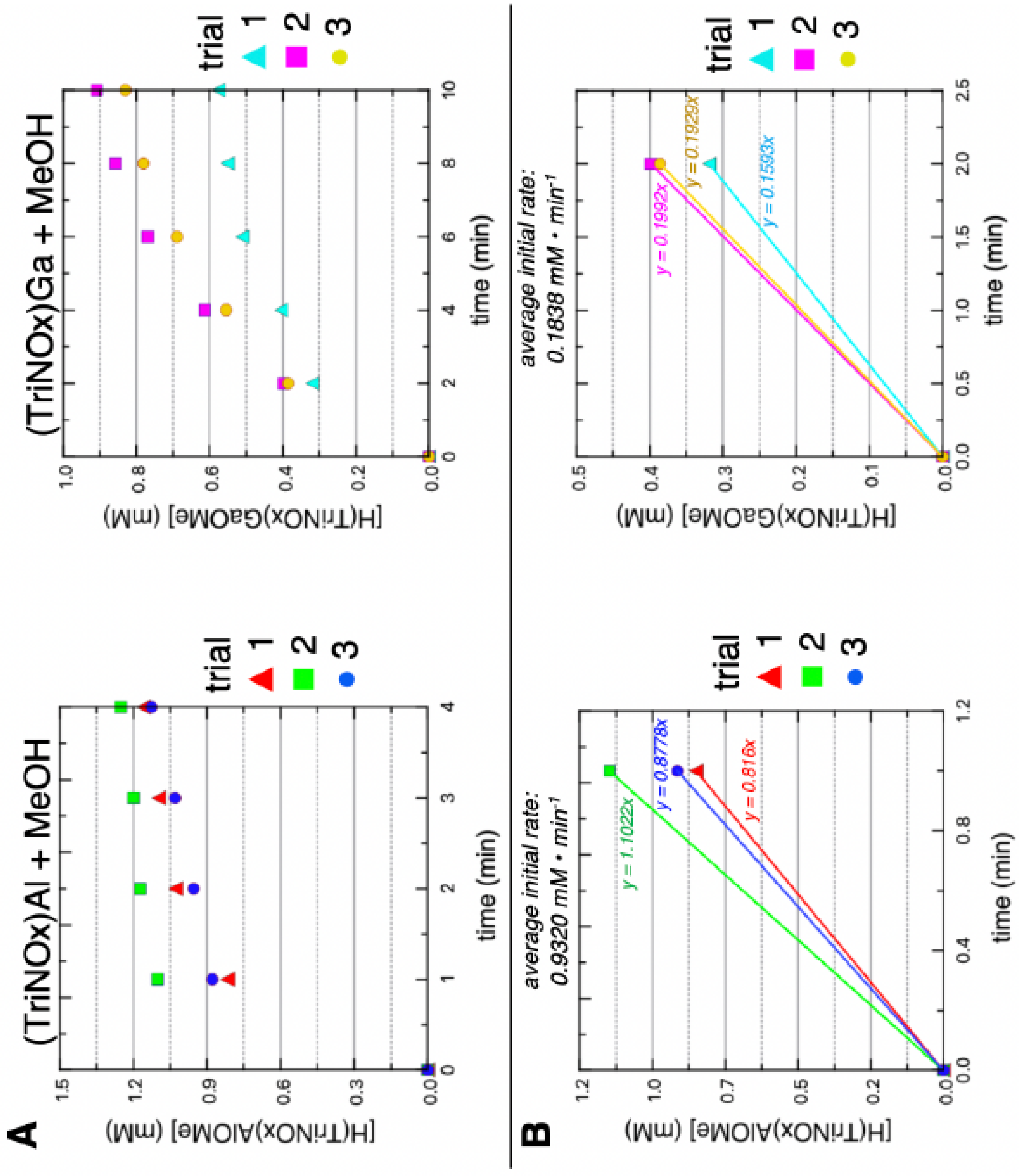

Figure S25. **A**. Reaction profiles of all three trials of the reactions of complexes **1** and **2** with methanol, each loaded with initial concentrations of 6 mM. **B**. The linearly approximated initial rates of each trial of the stated reactions, with the average initial rate calculated above each plot.